EXPERIMENTAL FULL-FIELD ASSESSMENT OF KINEMATICAL AND IMAGING FLUCTUATION PATTERNS

Siavash Maraghechi

To identify the distortions from deformations look inside this thesis

In order to correct the distortions on the thesis cover,
place the lens of your phone camera (or one open eye)
on the spot pointed on the cover and keep it
almost parallel to the surface of the booklet.

Experimental full-field assessment of kinematical and imaging fluctuation patterns

Siavash Maraghechi

Experimental full-field assessment of kinematical and imaging fluctuation patterns

Siavash Maraghechi

A catalogue record is available from the Eindhoven University of Technology Library.
ISBN: 978-90-386-4919-1

Cover design: Anastasija Mass and Siavash Maraghechi

Printed by: ProefschriftMaken || www.proefschriftmaken.nl

The research leading to these results has received funding from the European Research Council under the European Union's Seventh Framework Programme (FP7/2007-2013)/ERC grant agreement n^o [339392]

Experimental full-field assessment of kinematical and imaging fluctuation patterns

PROEFSCHRIFT

ter verkrijging van de graad van doctor aan de Technische Universiteit Eindhoven, op gezag van de rector magnificus prof.dr.ir. F.P.T. Baaijens, voor een commissie aangewezen door het College voor Promoties, in het openbaar te verdedigen op vrijdag 6 december 2019 om 13:30 uur

door

Siavash Maraghechi

geboren te Teheran, Iran

Dit proefschrift is goedgekeurd door de promotoren en de samenstelling van de promotiecommissie is als volgt:

voorzitter:	prof.dr.ir. D.H. van Campen
1^{e} promotor:	prof.dr.ir. M.G.D. Geers
2^{e} promotor:	dr.ir. J.P.M. Hoefnagels
copromotor:	dr.ir. R.H.J. Peerlings
leden:	prof.dr.ir. L. Govaert
	prof.dr. A.A. Zadpoor (Technische Universiteit Delft)
	dr. J.N. Périé (Université de Toulouse)
	prof.dr. E. Toussaint (Université Clermont Auvergne)

Het onderzoek of ontwerp dat in dit proefschrift wordt beschreven is uitgevoerd in overeenstemming met de TU/e Gedragscode Wetenschapsbeoefening.

Summary

Experimental full-field assessment of kinematical and imaging fluctuation patterns

For experimental studies of the mechanical performance of materials, it is essential to quantify the spatial variation of deformations which may occur even if the loading is more or less uniform. Often these deformation fields contain a significant amount of information that may be correlated over large distances compared to the typical length scale of the microstructure. Metamaterials, which are materials with a microstructural design to exhibit exotic behaviours, are an example that reveal such correlated fields. The architectured mechanical behaviour of metamaterials is based on the local kinematics at the scale of the microstructure exhibiting fluctuation patterns with long-range correlations. Spatially correlated patterns are not limited to mechanically induced fields, but can also be rooted in the experimental methodologies used for the kinematical assessment of materials. When images of a specimen are used to obtain full-field kinematic measurements during *in-situ* mechanical tests, distortions in the images introduce errors in the evaluated kinematics. These errors, e.g. due to image distortions, originate from the imaging systems used and may thus exhibit systematic patterns, which are therefore correlated over long ranges as well. Experimental identification of each of these types of spatially correlated fields, due to the measurement method or due to the mechanics of the material, is of great importance, as it allows one to significantly improve the accuracy of the measurement or to develop a better understanding of the mechanics, or in fact both. In this thesis, two cases are studied: (i) identification of Scanning Electron Microscopy (SEM) imaging distortions for full-field kinematic measurements, in order to minimize the distortion-induced errors, and (ii) identification of instability-induced patterns in cellular metamaterials, for better microstructural analysis and design. To this end, Digital Image Correlation (DIC) is exploited and extended as a full-field kinematical assessment method.

Considering the limitations of optical microscopy, high resolution imaging techniques such as SEM are important for experimental full-field kinematical assessments at micro and nano scales. SEM images are constructed based on a scanning process, leading to complex imaging fluctuation patterns, so-called imaging distortions. One group of SEM distortions is scan line shifts, which are localised shifts in the images parallel to the scanning direction. Such imaging fluctuations are easily mistaken for kinematic fluctuations, unless corrected for. An enriched DIC method, parameterizing the measurement

with smooth step functions, is developed and it is employed to identify this particular and challenging type of distortion and correct the SEM images. Successful identification and correction is achieved for SEM images (real and virtually generated) even with a rather high number of line shifts and large amplitudes (Chapter 2).

SEM images are not only affected by line shifts but also by spatial distortion and drift distortion. In order to attain reliable high-resolution measurements of kinematical fluctuation patterns using SEM-DIC, all three types of distortions should be identified and corrected for. By extending the methodology introduced for line shifts, a novel Integrated Digital Image Correlation (IDIC) scheme is developed, which integrates an SEM imaging model with the kinematic measurements of DIC, based on a composition of mapping functions. Each mapping function describes a part of the imaging and the mechanical deformation involved in an *in-situ* mechanical test in the SEM. This IDIC scheme, accompanied by a proper measurement procedure, enables an independent assessment of the imaging fluctuations and the kinematics, and thus to minimize the distortion errors. Virtual experiments show that the proposed method successfully removes the distortion-induced errors to attain the accuracy expected from DIC for the kinematic measurements. Application to real SEM images also proves to be effective in the proper measurement of SEM imaging fluctuation patterns, enabling accurate characterization of kinematical fluctuation patterns (Chapter 3).

Cellular elastomeric metamaterials exhibit a patterned deformation field under a critical compressive load, due to microstructural buckling. This pattern, which involves large local rotations, is significantly constrained by the boundary conditions applied, which lead to the formation of large boundary layers. A recent numerical study revealed a significant size effect in the global response of such metamaterials due to these thick boundary layers. To experimentally validate the size effects and their dependence on the boundary layers, custom-made moulds are used to manufacture meso-scale specimens (with a millimetric microstructural characteristic length), varying their overall size while keeping the microstructural feature size constant. *In-situ* mechanical compression tests under an optical microscope are combined with DIC to produce high-resolution full-field measurement of the underlying kinematic fields. The results show the effect of the specimen size on its global behaviour, as well as the boundary layers as predicted by the prior numerical study (Chapter 4).

In order to identify the long-range correlated fluctuations in cellular metamaterials, a well-defined decomposition of the displacement field into a smooth part, a correlated fluctuation field, and an uncorrelated fluctuation field is needed. To this end, the novel micromorphic IDIC methodology based on a kinematic ansatz proposed in a recent study is developed. A procedure is proposed for the proper regularization of the kinematics such that the correlated fluctuation modes as well as their spatial distribution are identified in a single minimization step. The methodology is tested on both virtual and on the real *in-situ* experiments of the previous chapter, showing good robustness and accuracy (Chapter 5).

Contents

Summary **iii**

1 Introduction **1**
1.1 Scientific Background 1
1.2 Objectives and Outline of the Thesis 4

2 Correction of scan line shift artifacts in scanning electron microscopy - an extended digital image correlation framework **7**
2.1 Introduction 7
2.2 Method 11
2.3 Validation of the method 18
2.4 Application to real SEM images 31
2.5 Conclusions 37
2.A Automatic algorithm to allocate scan line shifts to images in pre-correlations 38

3 Correction of scanning electron microscope imaging artifacts in a novel digital image correlation framework **41**
3.1 Introduction 42
3.2 SEM imaging artifacts 44
3.3 Methodology 46
3.4 Validation by virtual experiments: simple deformation and distortion fields 58
3.5 Validation by virtual experiments: complex deformation and distortion fields 67
3.6 Validation by virtual experiments: application to real SEM patterns . . . 70
3.7 Validation on real SEM images 75
3.8 Conclusions 79
3.A Alternative image gradient arrangement 83
3.B Initial guess for correlations 83

4 Experimental full-scale analysis of size effects in cellular elastomeric metamaterials **87**
4.1 Introduction 88
4.2 Methodology 89
4.3 Results and Discussion 92
4.4 Summary and Conclusions 98

4.A Material Characterization 99

5 Harvesting micromorphic fields from experiments on patterning metamaterials 101
5.1 Introduction 102
5.2 Micromorphic Integrated Digital Image Correlation 104
5.3 Results and Discussion 105
5.4 Summary and Conclusions 114

6 Conclusions and Recommendations 117
6.1 Conclusions 117
6.2 Recommendations for further research 120

Bibliography 123

List of Publications 133

Words of Thanks 135

Curriculum Vitae 137

Chapter 1

Introduction

1.1 Scientific Background

For analysing the mechanical performance of materials, it is often essential to visualize and quantify the spatial variation of deformations. In many cases, the deformation fields contain a significant amount of information that is correlated in space, i.e. their spatial variation is not of a random nature and correlations can be found between values in material points at a distance from each other. The range of these correlations depends on the macro and micro length scales of the problem, i.e. the macroscopic size of the specimen and the characteristic length of the microstructure of the material. Such long-rage correlated fields have been observed in different materials, in particular those with an architectured microstructural design exhibiting properties not found in nature, better known as metamaterials. Through a careful design of metamaterials, the morphology of the microstructure triggers an exotic mechanical response that can be exploited in dedicated applications. The architectured mechanical behaviour of metamaterials is based on the local kinematics at the scale of the microstructure exhibiting fluctuation patterns with long-range correlations. Another marked example of correlated fields is the cases where deformation in a material localizes in space, typically revealing a narrow band in which the deformation is considerably higher than in neighbouring areas. Such localized fields exhibit fluctuations in the kinematics that are correlated over large distances as well. Spatially correlated patterns are not limited to mechanically induced fields and can be rooted in the experimental methodologies used for the kinematical assessment of materials. When images of a specimen are used to obtain full-field kinematic measurements during *in-situ* mechanical tests, distortions in the images introduce errors in the evaluated kinematics. These errors, i.e. image distortions, originate from the imaging systems used and thus exhibit systematic patterns, which are therefore often correlated over long ranges as well.

Experimental identification of these spatially correlated fields is of great importance, whereby the identified fields are exploited for different purposes depending on the nature of the correlated patterns. Two important examples are considered in this thesis:

(i) Image distortions arising from the applied experimental methodologies, where the

independent identification of the error fields is of utmost importance, so that they can be adequately removed from the actual kinematic fields, minimizing measurement errors;

(ii) deformation patterns arising inside materials with an intrinsic microstructure, such as metamaterials, where the identified correlated kinematic patterns are exploited for a proper analysis and design.

This thesis aims at developing methodologies to independently identify spatially correlated patterns/fluctuations from data acquired during *in-situ* mechanical tests, with focus on imaging distortion patterns in Scanning Electron Microscopy (SEM) images and instability-induced patterns in cellular metamaterials. To this end, Digital Image Correlation (DIC) is exploited and extended as a full-field kinematical assessment method.

Digital Image Correlation

Different full-field displacement measurement techniques such as the grid method [1] or Digital Image Correlation (DIC) [2–4] exist to obtain strain fields in *in-situ* mechanical tests. Among these methods, DIC has proven to be the most popular one, due to its flexibility and relative ease of application. DIC is based on the conservation of gray scale between images of the reference and deformed configurations of a specimen, and is performed by minimization of the difference between the two images with respect to the displacement.

There are two major approaches to DIC [5], each suitable for different problems based on the objectives of the experimental study and the nature of the kinematics fields. Local DIC divides each image into small sections, called subsets, thereby identifying the displacement for each subset and consequently constructing the entire displacement field. An objective assessment of the displacement field results, which imposes minimal constraints on the unknown kinematics. However, it does not rely on any insight allowing to decompose the kinematics or to identify separate parts of the evaluated fields. In contrast to local methods, the DIC problem can be redefined and solved over the entire region of interest, i.e. the complete image in which the kinematics are to be determined. However, evaluation of the displacement vector in each pixel of a digital image results in an ill-posed problem requiring regularization (parametrization) of the kinematics in order to substantially reduce the number of degrees of freedom. Using prior knowledge on the unknown fields is an effective way of regularizing the DIC problem, giving rise to a family of DIC methods known as Integrated DIC (IDIC). This can be done by a numerical model describing the mechanics of the investigated material or by a parametric analytical description of the fields to be found, or a combination of both.

SEM Image Distortions

DIC is used in combination with a wide variety of imaging techniques such as optical microscopy [6], optical profilometry [7], scanning electron microscopy [8], scanning tunnelling microscopy [9], atomic force microscopy [10, 11], high-resolution transmission electron microscopy [9, 12]. Considering the limitations of optical microscopy in terms of spatial resolution and the relative ease of use of scanning electron microscopes, SEM has been proven to be a good candidate for high-resolution displacement measurements. The combination of SEM and DIC enables a high resolution for the kinematics, thanks to the high spatial resolution of SEM images and the sub-pixel accuracy of DIC. However, the imaging process, based on the scanning of an electron beam on the specimen surface, results in complex artifacts (distortions) in the images, which can introduce large errors in the evaluated kinematic fields, if ignored. In the literature, the SEM artifacts are typically categorized in three categories: (1) line shift artifacts, which are spurious shifts in the image parallel to the scanning lines, attributed to positioning errors in the scanning process and occurring randomly in time; (2) spatial distortion, which are distortions attributed to the electromagnetic lenses comparable to optical distortions of lenses. These are assumed to be constant in time if the imaging parameters are not changed; (3) drift distortion, which are distortions in the image in the form of shear/tension/compression due to the drifting of the specimen relative to the beam during the scanning process. All these distortions are reflected in the images in the form of long-range spatially correlated fluctuation patterns, considering their systematic natures. An example of SEM artifacts is shown in Fig. 1.1, where part a depicts an SEM micrograph of an electro-deposited copper film revealing the natural gray scale pattern from the microstructure of the material. This image is one of two images acquired one after another without any mechanical deformation induced in between. Fig. 1.1b, shows the difference between these two images after removing the rigid body translation between the two images due to drifting of the specimen. The gray scale pattern of the SEM images reflected in Fig. 1.1b, is only due to the artifacts, which are introducing local differences between the two images. Many line shift artifacts are visible in the lower part of the figure (highlighted by the arrows). There are many studies in the literature that investigate the different types of SEM artifacts and offer solutions for the correction of drift distortion, [10, 13–24], spatial distortion [23, 25–27] and line shift artifacts [28]. However a general framework for systematic identification of all three types of SEM artifacts, which is essential in eliminating the artifact induced errors on the kinematics, seems to be missing.

Cellular Metamaterials

Mechanical metamaterials are a class of materials designed to exhibit mechanical properties not found in nature. They have attracted the attention of many academic and industrial studies in the past decade. Cellular metamaterials [29–39], exhibit a significant change in their mechanical response beyond a critical compressive load, that

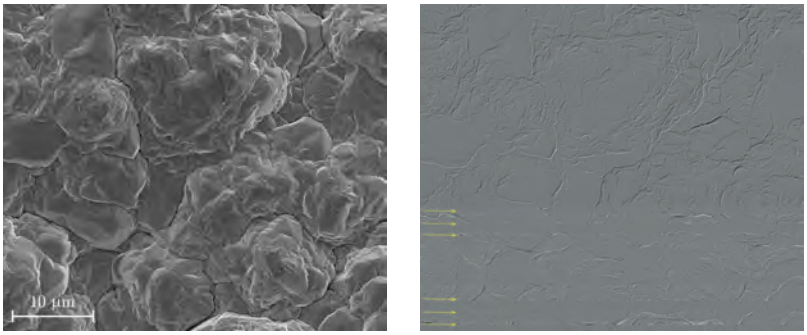

(a) SEM micrograph (b) Influence of Artifacts

Figure 1.1: The influence of imaging distortions on SEM images, (a) SEM micrograph of an electro-deposited copper film revealing the natural pattern of the microstructure. Two images have been taken one after another without any mechanical deformation applied in between. (b) The difference between the two images after removing the rigid translation between the two images, revealing the imaging artifacts.

induces a patterned deformation due to local buckling phenomena in the microstructure. By proper design of the microstructure, these pattern deformations can be exploited for dedicated applications, such as soft robotics [40, 41] and tunable materials [42, 43]. The buckling patterns in cellular metamaterials are typically correlated over long distances inside the specimen and govern the global mechanical behaviour of the material. They also trigger size effects, i.e. effects due to the influence of the size of the specimen with respect to the characteristic length of the microstructure. Fig. 1.2 depicts an example of a cellular elastomeric metamaterial under compressive load resulting in an emergent anti-symmetric buckling pattern that is correlated over the entire area of the specimen. Assessment of the kinematics and more specifically, the independent identification of these correlated fluctuations, is essential for a proper analysis and consequently a better design of cellular metamaterials.

1.2 Objectives and Outline of the Thesis

Integrated DIC offers an opportunity to develop diverse methodologies for identification of the correlated patterns described above. The regularization of IDIC, by exploiting prior knowledge of the nature of the phenomena of interest, can be devised such that it incorporates the characteristics needed to identify the spatially correlated fields. The goal of this thesis is to develop novel IDIC methodologies, based on models describing the nature of the correlated fields for the two presented cases of SEM artifacts and cellular metamaterials, both sharing the need to independently identify the underlying spatially correlated fluctuation fields.

In order to achieve this goal the following research questions need to be addressed:

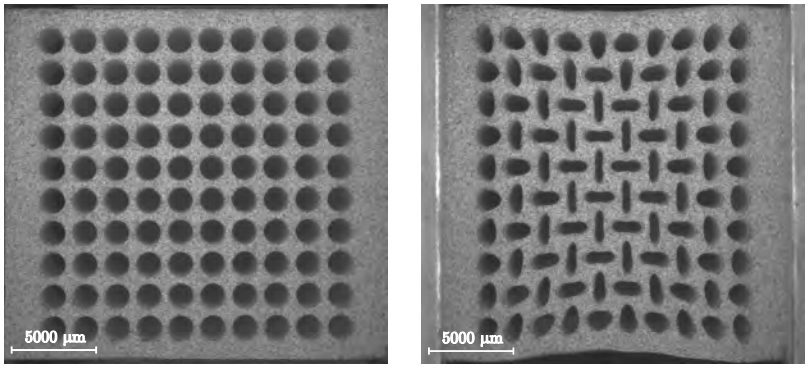

(a) Undeformed microstructure (b) Deformed microstructure

Figure 1.2: Elastomeric metamaterial specimen (a) before and (b) after the onset of microstructural buckling, due to compression in horizontal direction, resulting in the emergence of a long-range correlated fluctuation pattern.

(I) What is the proper model that incorporates the SEM imaging process with all its artifacts alongside the mechanical deformations in an *in-situ* test?

(II) How can the characteristics of SEM imaging distortion fields be exploited to identify them independently?

(III) How to manufacture and test lab-scale cellular elastomeric metamaterial specimens with a microstructure size that is small enough to be relevant for realistic applications and enabling full-field displacement measurements?

(IV) Can the correlated fluctuation pattern induced size effects, previously observed in idealized numerical studies on cellular elastomeric metamaterials, be quantified in experimental tests?

(V) What is an effective approach to decompose the kinematics of cellular metamaterials experimentally, providing a proper identification of all correlated fields?

These questions are explored in depth in this thesis in the following order. The next two chapters investigate the identification of correlated patterns arising from SEM imaging techniques.

Chapter 2 focuses on one family of SEM imaging artifacts, line shifts, which prove to be challenging to detect, identify and correct for. A proper parametrization, by a smooth step function, in combination with a composition of mapping functions in a novel IDIC scheme, is used to identify this type of artifacts. This constitutes the first step towards a thorough investigation of Questions (I) and (II) above. A methodological procedure is devised to recognize the presence of line shifts and to accurately evaluate the parameters characterising these line shift artifacts. Thorough virtual experiments demonstrate the

performance of the method even in the presence of complex mechanical deformations. The limitations are thereby objectively revealed. Application of the method to real SEM images shows the effectivity of the method in identifying and correcting the line shift artifacts in SEM images, even for a case with large amplitudes.

In Chapter 3, the artifact enriched IDIC methodology, initiated in Chapter 2, is further developed to identify all three types of SEM artifacts, i.e. line shift artifacts, spatial distortion and drift distortion. To achieve this, a complete model of the SEM imaging system combined with the mechanical deformations is set up. Separate mapping functions are defined, that take into account the non-linear interaction between the apparent mechanics and the different imaging steps, including the image artifacts. Proper experimental procedures are proposed to ensure accurate and independent identification of the three artifact types as well as the kinematics. Virtual experiments in the presence of complex mechanics show the robustness and accuracy of the method. The application on real SEM images demonstrates an accurate identification of the artifact patterns, thereby minimizing the resulting errors on the mechanics. By this means, this chapter adequately addresses Questions (I) and (II) mentioned above.

Chapters 4 and 5 investigate cellular metamaterials and the identification of the fluctuation patterns triggered by microstructural buckling.

In order to study the correlated fluctuation fields in cellular metamaterials, in Chapter 4, a systematic way is proposed to manufacture lab-scale cellular elastomeric metamaterial specimens and perform *in-situ* tests on them. Specimens are made with millimetric microstructures in order to be relevant for realistic applications of cellular metamaterials. By this means, this chapter spans Question (III). Local DIC is used to attain the displacement field, which are used to accurately assess the global and local behaviour and investigate the size effects in cellular elastomeric metamaterials. Size effects are studied, since these effects constrain the correlated fluctuation patterns occurring in these materials due to buckling of their microstructure. The results are compared to the size effects found in a recent numerical study [44], which responds to Question (IV) above.

In Chapter 5 the novel micromorphic IDIC methodology based on a kinematic ansatz proposed in a recent study [45], is exploited to decompose the kinematics of cellular metamaterials into a smooth slowly varying field and long-range correlated fluctuation patterns. A procedure is proposed for the proper regularization of the kinematics such that the correlated fluctuation modes as well as their spatial distribution are identified in a single minimization step. The methodology is tested on both virtual and real *in-situ* experiments, showing good robustness and accuracy, which directly addresses Question (V) mentioned above.

Finally, in Chapter 6 the overall conclusions and some recommendations for further research are discussed.

Chapter 2

Correction of scan line shift artifacts in scanning electron microscopy - an extended digital image correlation framework

Reproduced from:
S. Maraghechi, J. P. M. Hoefnagels, R. H. J. Peerlings, M. G. D. Geers
Correction of scan line shift artifacts in scanning electron microscopy - an extended digital image correlation framework, *Ultramicroscopy*, 187:144-163, 2018.

Abstract

High Resolution Scanning Electron Microscopy (HR-SEM) is nowadays very popular for different applications in different fields. However, SEM images may exhibit a considerable amount of imaging artifacts, which induce significant errors if the images are used to measure geometrical or kinematical fields. This error is most pronounced in case of full field deformation measurements, for instance by Digital Image Correlation (DIC). One family of SEM artifacts result from positioning errors of the scanning electron beam, creating artifactual shifts in the images perpendicular to the scan lines (scan line shifts). This leads to localized distortions in the displacement fields obtained from such images, by DIC. This type of artifacts is corrected here using global DIC (GDIC). A novel GDIC framework, considering the nonlinear influence of artifacts in the imaging system, is introduced for this purpose. Using an enriched regularization in the global DIC scheme, based on an error function, the scan line shift artifacts are captured and eliminated. The proposed methodology is demonstrated in virtually generated and deformed images as well as real SEM micrographs. The results confirm the proper detection and elimination of this type of SEM artifacts.

2.1 Introduction

Scanning Electron Microscopy (SEM) has proven itself to be one of the most powerful microscopy methods available. It offers a high spatial resolution (e.g. compared to

light microscopy) and relative ease of use (e.g. with respect to transmission electron microscopy). Besides qualitative studies based on SEM images of different materials, quantitative information can be extracted from them as well. Examples of quantitative measurements of in-plane geometrical properties may be found in different fields, such as nanocomposites [46, 47], micro residual stress measurements [48] , biomedical engineering [49, 50] and microscopy methods [51, 52]. Comparative studies between more than one image introduce another level of quantitative analysis on SEM images. Advanced quantitative measurements go as far as full field displacement measurements based on Digital Image Correlation (DIC) using SEM images in experimental micromechanics [3, 18, 25, 28, 53, 54]. However, using SEM images for a quantitative geometrical measurement becomes problematic if several complicated imaging artifacts occur [55, 56]. These artifacts result in distortions in the image, leading to errors in measurement of the underlying geometrical or kinematical fields. In particular, such distortions induce artifactual deformations and strains in DIC measurements, constituting significant errors if ignored. Due to the sensitivity of full field displacement measurements to these errors, caused by artifactual displacement fields, the DIC community is very concerned with the treatment of such imaging artifacts. The same concern is justified for other quantitative geometrical measurements based on SEM images.

SEM imaging artifacts can be categorized into three types [53]. The first type is non-random, time-independent spatial distortion, which is similar to distortions observed in optical systems. A number of papers propose different methods for dealing with this type of artifact [13, 25, 26]. The second category is non-random, time-dependent distortion, referred to as drift, which triggers stretch/compression and/or shear distortions in images. This is a direct result of the scanning involved in the SEM imaging process [57]. Different methods for correcting this artifact are proposed in the literature, for SEM images [13, 16, 19, 25], and for other microscopy methods involving a similar scanning process [58, 59]. The third type is a random, time-dependent distortion which is due to positioning errors of the electron beam during scanning, referred to as "scan line shifts". [60] reported the presence of such artifacts, in the form of local peaks parallel to the scan lines in strain maps determined by SEM-DIC. [28] conducted an extensive study on this artifact, which induces jumps in the displacement maps obtained by DIC. The effect of scanning parameters in four SEMs from different manufacturers was studied in their work. Integrating a collection of images was a solution, proposed to limit the influence of the scan line shifts. Integration of eight images reduce the artifact to a good extent, for scan line shifts upto one pixel. However, scan line shifts have an amplitude ranging up to 5 pixels, for which a significant artificial strain localization band remains after averaging. This paper proposes a systematic method to resolve the scan line shift artifact for SEM images, applicable to any imaging technique involving a scanning process.

Let us consider the scan line shift artifact in more detail. Fig. 2.1 exhibits a clear scan line shift in an SEM image. On the left, in Fig. 2.1a, an SEM image of a dual phase steel with a field of view of $30\mu m$ is presented. On the right, a zoomed view of the same image is compared to the zoomed view of another SEM image, scanned immediately after the first one (showing the same region). No mechanical displacement was applied

to the specimen between the two consecutive scans. The first image contains a scan line shift. This scan line shift is highlighted in Fig. 2.1a by the indicators showing the lower half of the feature moving downwards in the zoomed image on the right. Fig. 2.1b shows the displacement in the vertical direction found by standard local DIC between the two aforementioned SEM images. Two distinct jumps in the displacement field, one positive and one negative, are visible, occurring at certain y values and constant for all x values (y is the vertical coordinate, perpendicular to scanning direction, and x is the horizontal, scanning direction).

The occurrence of scan line shifts originates from the SEM imaging process. An SEM image is generated by scanning an electron beam point by point on the surface of the specimen and gathering the electrons that are emitted from the surface, due to the interaction of the electron beam and the specimen, by different sensors. Since the positioning of the beam during the scanning cannot be controlled by a closed loop, positioning errors are inevitable. The underlying reason for the scan line shifts is not reported in literature. A speculative cause of the incidental mispositioning may be a single dust particle in the electron column, which gradually charges up, but then suddenly releases the charge through an electric discharge which causes the sudden mispositioning of the electron beam. This error is a high frequency phenomenon if occurring between pixels in the same row in an image, thus contributing to the noise. However, if such a positioning error occurs between two consecutive scanning lines, a low frequency phenomenon, it becomes detectable as a shift in the image, see e.g. in Fig. 2.1b. The repositioning of the electron beam in the direction perpendicular to the scanning direction is done once per scan line. Hence, an error in this direction persists until the end of that scan line and subsequently propagates to the next line. This type of artifact therefore reveals an artificial band of localized distortion along the scanning direction in the image.

The aim of the current work is to develop a framework to deal with the scan line shifts in SEM images using a systematic approach. This enables: (i) direct removal of scan line shifts from images, (ii) integration with other methods available in the literature, for the correction of drift and spatial distortion artifacts, (iii) future extension of the method to a general framework dealing with all types of SEM artifacts in a unified manner. To this end, global digital image correlation (GDIC) is used as a general framework in order to deal with the scan line shift artifact.

In GDIC the deformation field between two images is directly determined in the whole region of interest of the images. This is done by parameterizing the spatial variation of the displacement field, possibly using prior knowledge on the kinematics characterizing the deformation, i.e. regularizing the displacement field. Using a smooth step function, e.g. error function, for each scan line shift occurring in the images, the artifact field needed for correcting the images can be determined. Contrary to local DIC, the GDIC framework allows for direct insertion of these step function fields in the brightness conservation algorithm. Note that this GDIC framework can be extended in the future to correct for drift and spatial distortion as well.

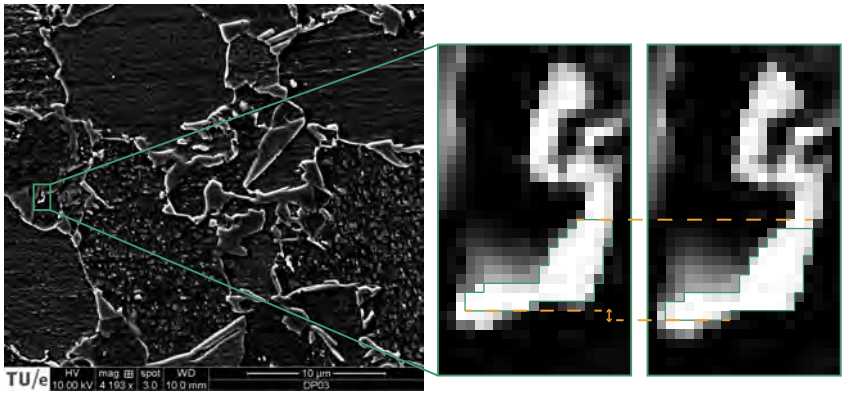

(a)

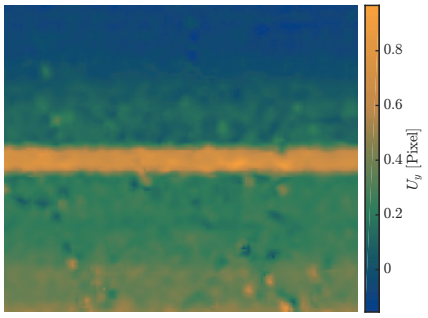

(b)

Figure 2.1: Example of scan line shift artifact in the scanning process; (a) An SEM image at high magnification of a dual phase steel specimen and a zoom of a microstructural feature in two consecutive scans reveals the scan line shift in shortening the feature on the left; (b) displacement in the vertical direction found by local DIC, exhibiting two clear jumps.

In order to achieve the aim mentioned above, the standard GDIC formulation is modified for incorporating imaging artifacts (Section 2.2.1 to 2.2.3). The new formulation is included in a proper procedure for accurately detecting and removing scan line shifts (Section 2.2.4). The methodology is applied to different virtual experiments to asses the effectiveness, accuracy and convergence behavior of the extended GDIC algorithm (Section 2.3). Finally the method is applied to real SEM images for two cases, one with mechanical deformation and one without (Section 2.4).

2.2 Method

2.2.1 Brief review of conventional GDIC

The algorithm used in GDIC is based on the minimization of the gray scale residual :

$$r(\mathbf{x}, \underline{\mathbb{o}}) = f(\mathbf{x}) - g \circ \boldsymbol{\phi}(\mathbf{x}, \underline{\mathbb{o}}) = f(\mathbf{x}) - g\left(\boldsymbol{\phi}(\mathbf{x}, \underline{\mathbb{o}})\right) \quad \text{with} \quad \boldsymbol{\phi}(\mathbf{x}, \underline{\mathbb{o}}) = \mathbf{x} + \mathbf{u}(\mathbf{x}, \underline{\mathbb{o}}), \quad (2.1)$$

which is the difference between the gray value in the reference image f, at original position $\mathbf{x}$, and the deformed image g at deformed position $\boldsymbol{\phi}(\mathbf{x})$. The mapping function $\boldsymbol{\phi}$ implicitly defines the displacement field $\mathbf{u}(\mathbf{x})$. The notational convention of [61] is used, where the operator $\circ$ indicates the composition of two functions. The mapping function is parametrized by a set of degrees of freedom (dofs) stored in the column matrix $\underline{\mathbb{o}} = [a_1, a_2, \ldots, a_n]^T$. Due to noise in the images and the inaccuracy of the regularization used in $\boldsymbol{\phi}(\mathbf{x}, \underline{\mathbb{o}})$, the gray scale conservation leads to a non-zero residual field. This residual field is minimized with respect to $\underline{\mathbb{o}}$ using a least squares approach. As explained in detail in [61], this results in a nonlinear system of equations which is linearized to yield an iterative Newton-Raphson scheme for updating the dofs, $\delta\underline{\mathbb{o}}$, in each iteration:

$$\underline{\underline{M}}\,\delta\underline{\mathbb{o}} = \underline{b}. \quad (2.2)$$

The elements of $\underline{\underline{M}}$ and $\underline{b}$ in Eq. (2.2) are defined as:

$$M_{ij} = \int_\Omega L_i(\mathbf{x}) L_j(\mathbf{x}) d\mathbf{x} \quad (2.3)$$

$$b_i = \int_\Omega r(\mathbf{x}, \underline{\mathbb{o}}) L_i(\mathbf{x}) d\mathbf{x}, \quad (2.4)$$

where $i, j = 1, 2, \ldots, n$ (with n the number of degrees of freedom) and Ω the domain on which the problem is solved i.e. the region of interest in the images. Note that the matrix $\underline{\underline{M}}$ results from the Hessian matrix of a full-Newton method after neglecting two higher order terms, see [61]. The function L_i, in Eqs. (2.3) and (2.4) is given by:

$$L_i(\mathbf{x}) = \boldsymbol{\nabla}(g \circ \boldsymbol{\phi}(\mathbf{x})).\frac{\partial \boldsymbol{\phi}(\mathbf{x}, \underline{\mathbb{o}})}{\partial a_i}, \quad (2.5)$$

i.e. L_i is the inner product of $\boldsymbol{\nabla}(g \circ \boldsymbol{\phi}(\mathbf{x}))$, the gradient of the deformed image assessed at position $\boldsymbol{\phi}(\mathbf{x})$ with respect to the deformed coordinates, and $\frac{\partial \boldsymbol{\phi}(\mathbf{x}, \underline{\mathbb{o}})}{\partial a_i}$, the sensitivity functions for each degree of freedom. If the mapping function is linearly dependent on the degrees of freedom, the sensitivity functions can be taken as basis functions of the displacement field. This is often the case, though not always. Different approximations can be made for the image gradient, affecting the resulting convergence behavior, as discussed by [61]. It is common to choose the gradient of the reference image as an approximation of the image gradient in case of linearly independent basis functions and

small deformations. This implies that the $L_i(\mathbf{x})$ for all dofs (and thus $\underline{\underline{M}}$) is calculated once at the start of the correlation and used for all subsequent iterations.

2.2.2 New GDIC formulation for imaging artifacts

As discussed in the introduction, if SEM images are used for DIC or any other quantitative measurement, the imaging artifacts should be corrected for, to avoid significant errors in the results. Global DIC can be used to eliminate SEM imaging artifacts in a systematic way, by incorporating them via mapping functions akin to the function $\boldsymbol{\phi}(\mathbf{x})$ in Eq. (2.1) . However, note that the imaging artifacts may be present in both the reference image f and the deformed one, g. Fig. 2.2a shows the sequential mechanical and artifactual mappings, where F is the reference pattern free of artifacts, G is the true deformed pattern (also free of artifacts) and f and g are undeformed and deformed images with artifacts, respectively. Fig. 2.2b depicts the true, artifact-free reference pattern and the position vector of a specific material point, $\mathbf{x}$. In order to identify the corresponding gray scale value in image f, the position vector has to be corrected through the mapping function $\boldsymbol{\phi}_f(\mathbf{x})$ representing the artifacts in the reference image. The mapping function $\boldsymbol{\phi}_f(\mathbf{x})$ provides the pixel position where the gray scale value from the material point $\mathbf{x}$ was registered, while scanning image f. This is illustrated in Fig. 2.2c. The same material point in $\mathbf{x}$ is mapped onto a new true position by the deformation map $\boldsymbol{\phi}_m(\mathbf{x}) = \mathbf{x} + u(\mathbf{x})$. The deformed pattern G thus obtained, is subsequently imaged, and also possibly affected by artifacts, which are characterized by $\boldsymbol{\phi}_g(\mathbf{x})$. The composition of these two mapping functions in image g incorporates both the mechanical deformation and the correction needed for the imaging artifacts. The extended residual in gray scale conservation now reads:

$$\begin{aligned} r(\mathbf{x}) &= f(\boldsymbol{\phi}_f(\mathbf{x}, \underline{\mathbb{o}})) - g(\boldsymbol{\phi}_g(\boldsymbol{\phi}_m(\mathbf{x}, \underline{\mathbb{o}}))) \\ &= f \circ \boldsymbol{\phi}_f(\mathbf{x}, \underline{\mathbb{o}}) - g \circ \boldsymbol{\phi}_g \circ \boldsymbol{\phi}_m(\mathbf{x}, \underline{\mathbb{o}}). \end{aligned} \tag{2.6}$$

Note that in the absence of imaging artifacts, i.e. $\boldsymbol{\phi}_f = \mathbf{x}$ and $\boldsymbol{\phi}_g = \mathbf{x}$, the conventional definition (2.1) is recovered, with only mechanical mapping $\boldsymbol{\phi} = \boldsymbol{\phi}_m$ remaining. Note also that, $\underline{\mathbb{o}}$ represents the dofs of all the mapping functions, mechanical and imaging related, as a column matrix. Evidently, each mapping function depends only on the degrees of freedom associated with it. However, to avoid confusing notations, the complete array of dofs, i.e. $\underline{\mathbb{o}}$, is used everywhere.

Starting from this extended definition of the residual field, Eq. (2.6), the solution procedure can be established, providing the same Eqs. (2.2), (2.3) and (2.4), yet with a different definition of $L_i(\mathbf{x})$:

$$L_i(\mathbf{x}) = -L_i^f(\mathbf{x}) + L_i^g(\mathbf{x}) + L_i^m(\mathbf{x}), \tag{2.7}$$

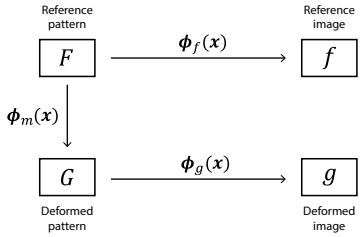

(a)

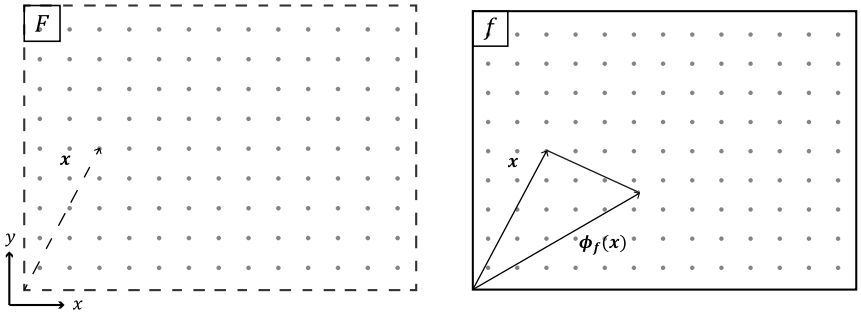

(b) (c)

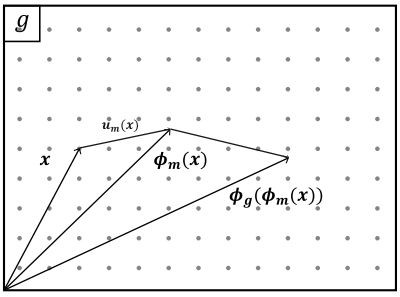

(d)

Figure 2.2: Non linear mapping functions of artifacts and mechanical deformation in both reference and deformed images: (a) Order in which the mapping functions apply, (b) reference (true) specimen's pattern F, (c) mapped position for $\mathbf{x}$ in image f including artifacts, and (d) mapped position for the displaced $\mathbf{x}$ in image g based on mechanical deformation and artifact distortions

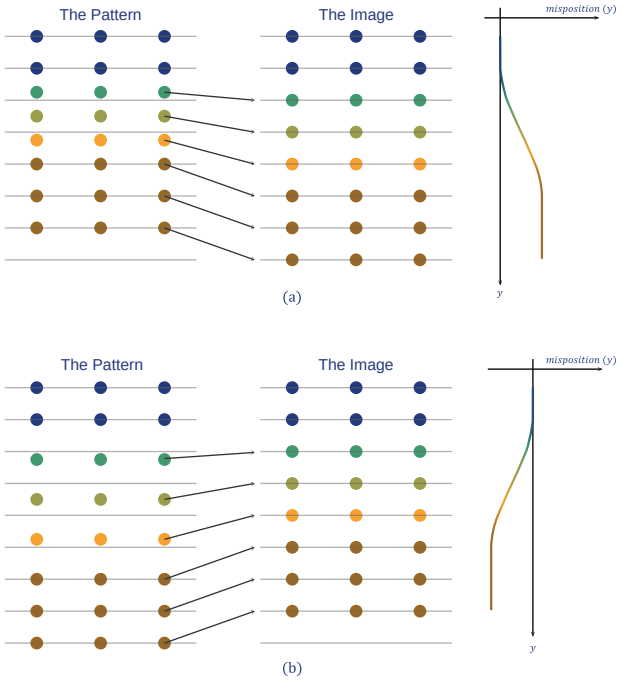

Figure 2.3: Gradual mispositioning of scanned points (left) and its effect on the registered image (right), resulting in artifactual localized (a) tension and (b) compression. On the pattern, the gray lines are the intended scanning lines while the dots are the actual scanned positions. In the image, the dots define the pixels. The blue color represents no positioning error while the gradual change to brown aligns with the gradual change of the error to it's maximum (one pixel in this case). The curves, on the other hand, show the gradual change of the mispositioning as reflected in the image.

where $L_i^f(\mathbf{x})$, $L_i^g(\mathbf{x})$ and $L_i^m(\mathbf{x})$ are defined as:

$$L_i^f = \left(\boldsymbol{\nabla} f \circ \boldsymbol{\phi}_f\right) . \frac{\partial \boldsymbol{\phi}_f}{\partial a_i}, \tag{2.8}$$

$$L_i^g = \left(\boldsymbol{\nabla} g \circ \boldsymbol{\phi}_g \circ \boldsymbol{\phi}_m\right) . \left(\frac{\partial \boldsymbol{\phi}_g}{\partial a_i} \circ \boldsymbol{\phi}_m\right), \tag{2.9}$$

$$L_i^m = \left(\boldsymbol{\nabla} g \circ \boldsymbol{\phi}_g \circ \boldsymbol{\phi}_m\right) . \left(\boldsymbol{\nabla} \boldsymbol{\phi}_g \circ \boldsymbol{\phi}_m\right) . \frac{\partial \boldsymbol{\phi}_m}{\partial a_i}. \tag{2.10}$$

The present paper focuses on the scan line shift artifacts. This requires a proper definition of the artifact mapping functions $\boldsymbol{\phi}_f$ and $\boldsymbol{\phi}_g$, capturing the scan line shifts mathematically. Note that the proposed framework has the potential to be extended in

the future to incorporate the two other types of SEM imaging artifacts, i.e. drift and spatial distortion, if proper sensitivity functions are included in the artifact mapping functions, which would enable to determine the mechanical deformation field corrected for any artifacts. By focusing on the scan line shift artifacts only, as is done here, the influence of drift and spatial distortion is not eliminated. However, after the scan line shifts have been detected and corrected properly, the procedure introduced in the work by [25] can be used to correct for drift and spatial distortion.

2.2.3 The new GDIC formulation for the scan line shift artifact

In order to define a proper mapping function to describe the scan line shift artifact, the underlying cause of the artifact and the trace it leaves in the images should be better understood. Fig. 2.3 illustrates the mispositioning of the electron beam and the image resulting from it. On the left side of Fig. 2.3a the horizontal lines represent the scanning lines if no positioning error would occur. The dots represent the actual positions where the intensities are registered. In this sketch, a gradual increase of mispositioning from zero to one pixel occurs in four scan lines. Indeed, in real SEM images the scan line shift typically has a width of a few scan line spacings. In the image on the right, the measured intensity is attributed to the presumed pixel position. This results in an artifactual localized stretching of the pattern in the image. A localized compression results in the opposite case, in which the actual scan lines have a larger spacing than the presumed ones, as depicted in Fig. 2.3b. The same mispositioning depicted in Fig. 2.3 can also occur in the scanning direction ($\mathbf{x}$ direction), leading to an artificial shear distortion in the images.

Based on the description above, the scan line shifts are efficiently described by mapping functions based on the error function, as:

$$\boldsymbol{\phi}_f(\mathbf{x}) = \mathbf{x} + \frac{1}{2}\left(A_x\mathbf{e}_x + A_y\mathbf{e}_y\right)\left(1 + erf\left(\frac{(y - y_0)}{\frac{w}{3\sqrt{2}}}\right)\right), \tag{2.11}$$

where:

$$erf(z) = \frac{1}{\sqrt{\pi}}\int_0^z \mathrm{e}^{-t^2}dt. \tag{2.12}$$

The degrees of freedom are A_x, A_y, y_0 and w, i.e. the amplitudes in x and y direction, the position and the width of the scan line shift, respectively. The denominator of the argument of the error function, in Eq. (2.11), is by definition $\sqrt{2}\sigma$, where σ is the standard deviation associated with the error function. By setting the denominator equal to $\frac{w}{3\sqrt{2}}$ the width of the scan line shift is chosen to be 6σ (to 99.7% approximation). In Eq. (2.11) the subscript f indicates that the mapping function belongs to the artifacts present in the reference image, while subscript g would refer to the mapping for artifacts in the deformed image. Note that the artifact mapping function is not linearly dependent on the degrees of freedom. This implies that $L_i(\mathbf{x})$ needs to be updated in every iteration for these dofs. Hence, it is not numerically convenient to adopt the gradient of image

f as an approximation of the complete form of the image gradient. Accordingly, the complete image gradient, as described in Eqs. (2.8) to (2.10), is used instead. Fig. 2.4 shows the graphical representation of the distortion field $(\boldsymbol{\phi}_f(\mathbf{x}) - \mathbf{x})$ based on the error function, where the color corresponds to the norm of the distortion vector and the dashed rectangle shows the undistorted configuration.

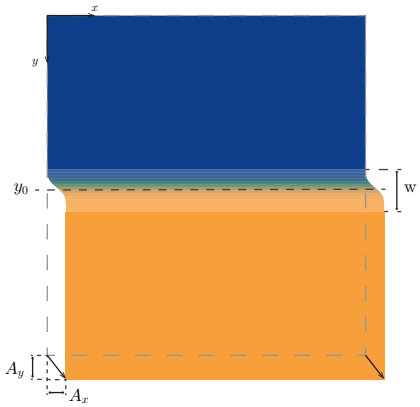

Figure 2.4: 2D representation of the error function as the distortion field for the scan line shift artifact, defined by four degrees of freedom, i.e. A_x, A_y, y_0 and w. The colors correspond to the norm of the distortion vector $\boldsymbol{\phi}_f(\mathbf{x}) - \mathbf{x}$. The dashed rectangle is the undistorted configuration.

2.2.4 Detection and correction of the scan line shifts

In order to solve the nonlinear least squares problem in global DIC, it is common to use a Newton-Raphson scheme, whereby the robustness depends on the initial guess of the degrees of freedom. This initial guess is particularly important for the position of the scan line shift, y_0, due to the small support of the corresponding sensitivity function. In this section the procedure to detect the presence of scan line shifts in images and the subsequent steps to accurately estimate the corresponding degrees of freedom are discussed.

To detect possible scan line shifts in the images, a pre-correlation between two images is performed. The pre-correlation is a simple conventional global DIC procedure using only a set of linear polynomials as basis function, i.e. six dofs. The pre-correlation obviously neglects the existence of a scan line shift, if present, which is therefore reflected in residual field. The few degrees of freedom defining the deformation field enable the polynomial to match the displacements on both sides of the scan line shift only in an average sense. This results in a strong gradient in the residual in the direction perpendicular to the scan lines. This pronounced spatial variation in the residual field of a single correlation indicates how many scan line shifts are present in the correlated pair of images. Moreover, it provides a good initial guess of the position of each scan line shift, even though it cannot reveal to which image each scan line shift belongs.

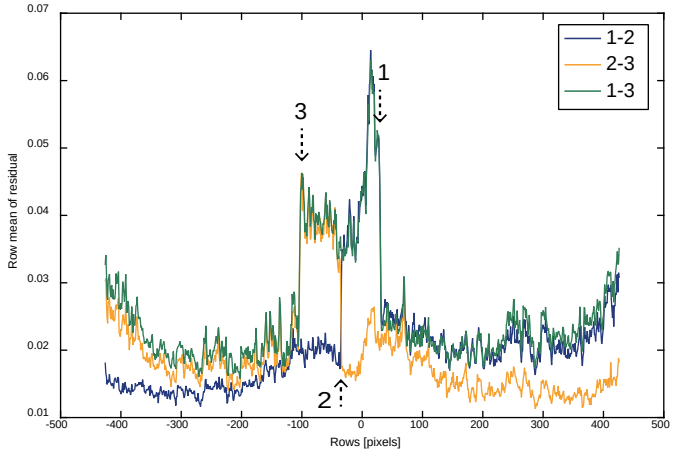

Figure 2.5: Row average of the residual fields of three pre-correlations between three typical SEM images (1, 2 and 3) providing the initial guess for the vertical position of the scan line shifts.

In order to be able to allocate each scan line shift to the correct image, the pre-correlation should be performed between all three pairs of a set of three images, i.e. three separate pre-correlations on three images of the same area of the specimen. Fig. 2.5 shows an example (case of Section 2.4.1) of the row average of the residual fields for three pre-correlations between Images 1-2, 2-3 and 1-3, in blue, orange and green, respectively. The horizontal axis is the y-coordinate of each row, along the direction perpendicular to the scan lines. A high gradient in the residual field that occurs in the same position in two pre-correlations represents a scan line shift that exists in the image that is present in both pre-correlations. Thus, by comparing the average residual of three pre-correlations all scan line shifts in the images can be allocated to their corresponding images. A convenient algorithm has been devised to automatically perform the procedure described above and allocate each scan line shift to the corresponding image for each image triple. For more details see Appendix 2.A.

When approximate scan line shift positions have been established for each image through the pre-correlations, the artifact mapping functions, i.e. $\boldsymbol{\phi}_f$ and $\boldsymbol{\phi}_g$, can be assigned for the final correlation between two images. The resulting initial guess for the position is accurate to within ± 10 pixels. It will be shown in the next section that this accuracy is sufficient to guarantee convergence. Subsequently, the correlation to correct the scan line shifts is performed in two steps. In the first step, the width of each scan line shift is fixed to a large value (here taken as 20 pixels) and only the amplitudes in x and y direction and the position of the scan line shifts are taken as degrees of freedom. The second step is carried out with all four degrees of freedom for each scan line shift, using the results of the previous step as initial guesses. Fixing a large width in the first step causes the support of the sensitivity map related to the position degree of freedom to be large, which relaxes the dependence on the scan line shift position's initial guess and

thus improves robustness. This point will be discussed in more detail in the following section.

An overview of the whole process described above is presented in Fig. 2.6.

2.3 Validation of the method

The effectiveness and the accuracy of the method explained in the previous section is assessed here through virtual experiments. A number of speckle pattern images are created, on which known distortions associated with the scan line shift artifact are applied. The resulting scan line shift artifact fields are computed from the images using the GDIC approach presented in the previous section. The error in the correlated distortion field is obtained by comparing the computed field with the exact field used in the generation of the deformed/distorted images.

The generation of the images should not introduce any errors in the virtual displacement field in the images, as these would be attributed to the error in the GDIC method. One of the most common sources of error in DIC in general is the error related to the gray scale interpolation [53]. This bias error is inevitable in the correlation process. When generating virtual images the same interpolation errors may occur. For this reason discrete interpolation is avoided in the generation process by defining the images as continuous mathematical functions. They are based on the superposition of a number of randomly placed circular Gaussian peaks:

$$F(x,y) = \sum_i a e^{\left(-\frac{1}{2}\left(\frac{(x-\mu_x^i)^2}{\sigma_x^2}+\frac{(y-\mu_y^i)^2}{\sigma_y^2}\right)\right)} \tag{2.13}$$

where a is the amplitude of each peak, μ_x and μ_y are the center coordinates of each peak (chosen randomly), and σ_x and σ_y are standard deviations in x and y direction, respectively. The standard deviations, taken equal here, define the width of each speckle peak. The image is made with two layers of Gaussian peaks corresponding to two different speckle sizes. The addition of the larger speckles (the second layer) improves the robustness of the correlation in terms of initial guess. One of the virtual experiments of section 2.3.2 is repeated with only one layer of Gaussian peaks (the finer speckles) to evaluate the influence of the second layer. Gaussian noise with a standard deviation of either 0.5, 1, or 2.5% of the dynamic range has been added to each image. All the images are normalized in gray scale to have a dynamic range equal to 1. The virtual pattern, F, represents the physical pattern on the specimen in a real experiment. Both images f and g are generated from F and are 513×513 pixels in size. The deformed image, g, is generated by mapping the pattern F based on $\boldsymbol{\psi}$, the generation mapping function. In order to find the generation mapping function, let us consider a general case of virtual generation of a deformed image $g(\mathbf{x})$ with deformation described by the mapping function $\boldsymbol{\phi}(\mathbf{x}) = \mathbf{x} + \mathbf{u}(\mathbf{x})$, from the reference pattern $F(\mathbf{x})$. In the absence of noise we have $F(\mathbf{x}) = g(\boldsymbol{\phi}(\mathbf{x}))$ for each $\mathbf{x}$. Inserting $\mathbf{x} = \boldsymbol{\phi}^{-1}(\mathbf{x}^*)$ in the previous equation yields: $F(\boldsymbol{\phi}^{-1}(\mathbf{x}^*)) = g(\mathbf{x}^*)$. Thus, the generation mapping function is the

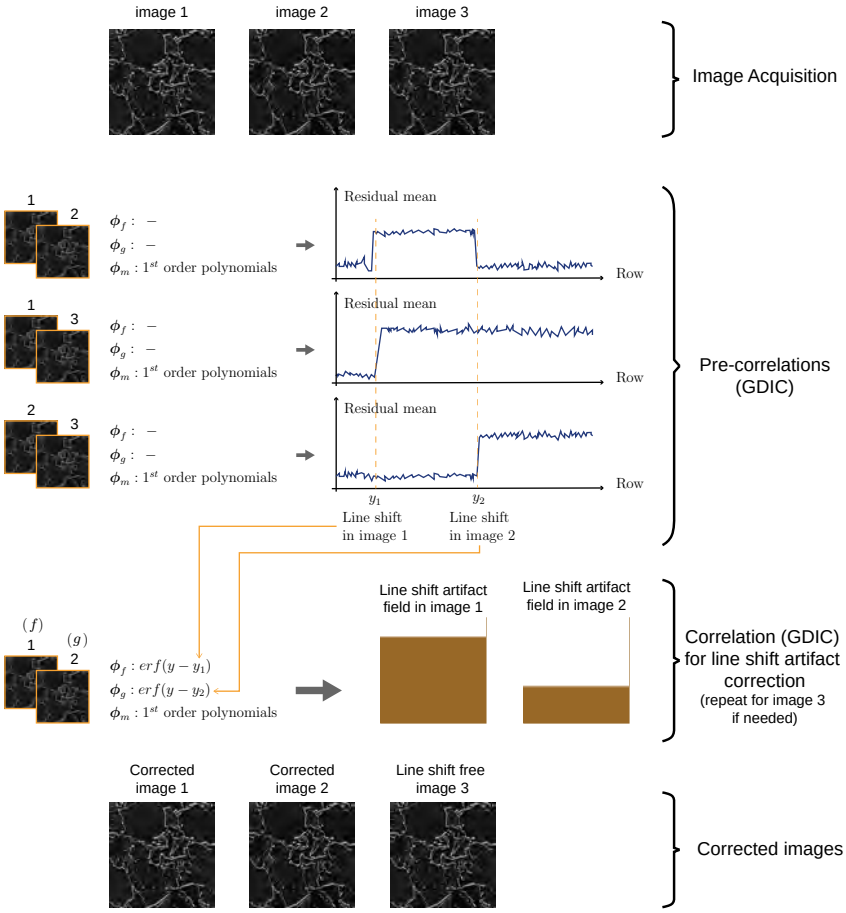

Figure 2.6: An overview of the process of correcting scan line shift artifacts in SEM images, starting with acquisition of (at least) three images, followed by three pre-correlations, and the main correlation for image correction. The pre-correlations are done with the regularization of ϕ_m based on 1^{st} order polynomials. By comparing the row average of residual fields of these pre-correlations, two jumps are allocated: in this example, to images 1 and 2, with positions y_1 and y_2 as initial guess, respectively. The results of the pre-correlations are used to perform the main correlation, resulting in the measurement of the scan line shift artifact fields in images 1 and 2, which can be repeated for image 3 if needed. The images are then corrected based on the artifact fields found.

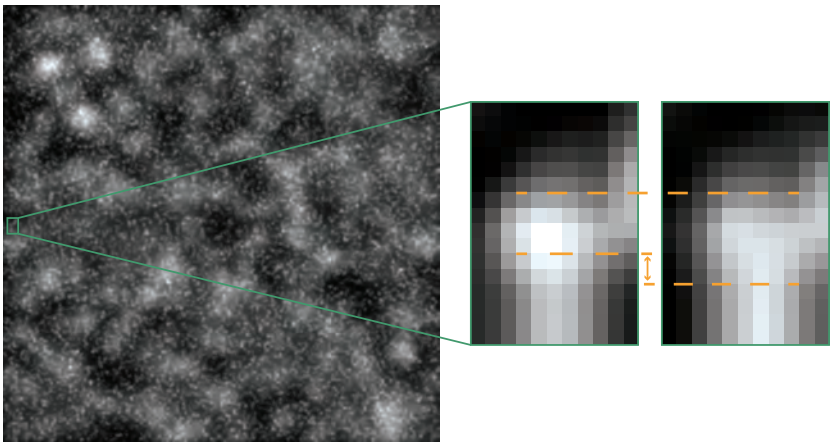

Figure 2.7: Typical virtual image created by superposition of Gaussian functions and the zoomed feature showing the effect of a smooth scan line shift incorporated in the deformed image.

inverse of the mapping function that describes the deformation/distortion field that will eventually be present in image g, i.e. $\boldsymbol{\psi}(\mathbf{x}) = \left(\boldsymbol{\phi}_g \circ \boldsymbol{\phi}_m(\mathbf{x})\right)^{-1}$, where $\boldsymbol{\phi}_g$ is defined as in Eq. (2.11).

Fig. 2.7 shows one of the resulting virtual images with the effect of a smooth scan line shift (case of Section 2.3.1) on a feature in the pattern.

The virtual experiments are performed on three image categories: (i) one scan line shift in an image pair, (ii) multiple scan line shifts per image in a set of three images, to study the limitations of the method in terms of number of scan line shifts per image and their spacings, and (iii) multiple scan line shifts per image in the presence of mechanical deformation fields. The images of the two later categories are also distorted by other SEM artifacts, i.e. drift and spatial distortion. Note that the first two categories represent the geometrical correction needed when using SEM images, whereas the last category focuses on the measurement of mechanical deformation.

2.3.1 Virtual experiments with a single scan line shift

In the first set of virtual experiments, the robustness of the proposed method in terms of initial guess as well as the influence of noise is evaluated. A pair of virtual images is generated, one without any artifact and one with a single scan line shift embedded. The scan line shift is placed at position $y = 3$ pixels (the origin of the coordinate system being at the center of the image) and has a width of 4 pixels with amplitudes of 1 and 2 pixels in x and y direction, respectively. The virtual images are then correlated using the approach proposed in section 2. In order to assess the influence of the initial guess, a series of correlations are performed with the same set of images, but with a different initial guess for the degrees of freedom of the scan line shift. Since the pre-correlations

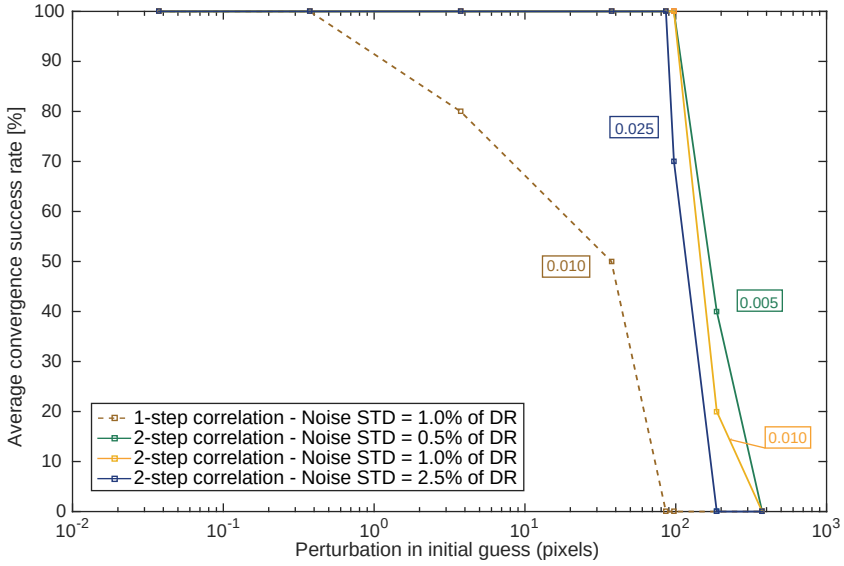

Figure 2.8: Average convergence success rate versus the amplitude of the perturbation applied to the initial guess for different values of noise in the virtual experiments. The 1-step correlation involves all four degrees of freedom in a single correlation (direct correlation for both amplitudes, position and width of the scan line shifts), whereas the 2-step correlation corresponds to an initial correlation of only the position and both amplitudes while keeping the width constant (at 20 pixels), followed by a second correlation with all four dofs.

only serve to provide an initial guess for the position of the scan line shifts, no pre-correlation is performed in this case. The convergence criterion is based on the mean of the absolute value of change in the degrees of freedom, for which a tolerance of 1e−5 is adopted.

Fig. 2.8 shows the average convergence success against random perturbations of a certain amplitude in the initial guess with respect to the exact values. Each point in the plot represents ten correlations for a certain perturbation in the initial guess of the degrees of freedom. A success rate of 100% means that all the ten correlations with that specific perturbation amplitude have converged, while 0% means that none have converged. The only difference between the different curves shown is the noise level added to the images. The standard deviation of the noise implemented in the virtual images has been varied from 0 to 2.5% of the dynamic range. For one noise level, i.e. 1%, also a direct (1-step) correlation with all four dofs is shown, in contrast to the 2-step correlation procedure described in the previous section. The large sensitivity to the initial guess of the 1-step correlation, compared to the 2-step correlation, justifies the use of the latter. In case of 0.5% and 1% noise, the convergence success rate is 100% upto more than 90 pixels of perturbation in the initial guess, while this value equals 80

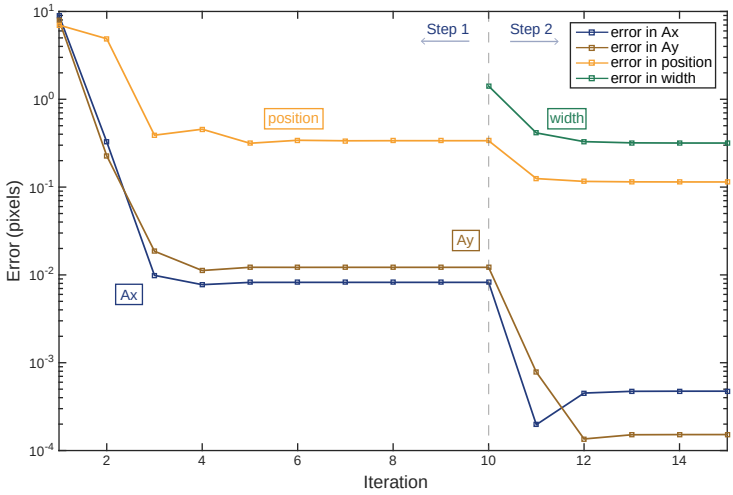

Figure 2.9: Iterative error evolution for virtual images containing one scan line shift only, without noise, and with 10 pixels of perturbation in initial guess, for 2.5% noise (iterations 1 to 10: first correlation step; iterations 11 to 15: second correlation step)

pixels for a noise level of 2.5%, which shows that the approach is very robust.

Fig. 2.9 shows the error in the degrees of freedom characterizing the scan line shift, i.e. the difference of the dofs obtained by the correlation and the reference values used to generate the images (amplitude in x and y direction, position and width), for each iteration during both steps of the correlation. The error for the width is meaningful only for the second correlation step, where it is used as a degree of freedom; therefore it is plotted only for the iterations related to the second correlation step. The final error is negligibly small (bellow 5e−4 pixel) for both amplitudes and relatively small for the position (1.2e−1 pixel) and width (3.1e−1 pixel) at final convergence. The higher value of error associated with the position and width, compared to the amplitudes, is due to the fact that an error in the evaluation of position and width increases the residual field only at the location of the scan line shift, whereas the same relative error in the amplitude of the scan line shift affects a large area of the residual. This results in the observed lower sensitivity to the width and position. In summary, the method reveals and adequate robustness for a wide variation in the initial guess and in the presence of noise.

2.3.2 Virtual experiments with multiple scan line shifts

SEM images may exhibit multiple scan line shifts, and may be affected by drift and spatial distortions as well. The limitations of the proposed method in terms of the number of scan line shifts per image and the distance between occurring scan line shifts

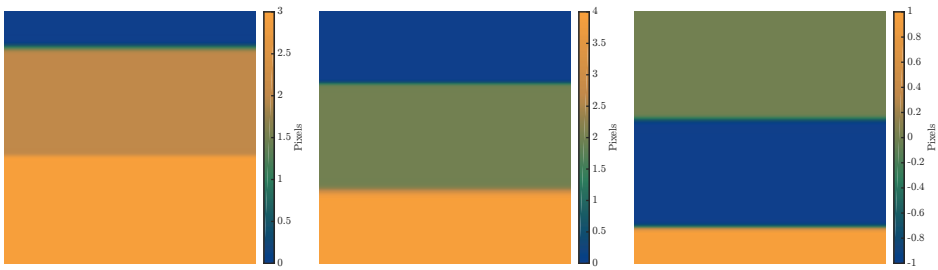

(a) (b) (c)

Figure 2.10: The x component of scan line shift artifact fields in a virtual experiment with two scan line shifts per image in, (a) Image 1, (b) Image 2 and, (c) Image 3, revealing the spacing and the distribution of scan line shifts in the three images.

are investigated in this section. This is done in a more realistic case, i.e. in the presence of drift and spatial distortion and without including an accurate description of them.

Virtual experiments with different numbers of scan line shifts per image, ranging from two to six, are studied. For each case, three images are generated with equally spaced scan line shifts distributed among the images. Fig. 2.10 depicts the distribution and spacing of the scan line shifts with two scan line shifts per image, where parts a, b, and c show the x component of scan line shifts in the first, second, and third image, respectively. Note that the minimum distance between scan line shifts in the case of 2, 3, 4, 5 and 6 scan line shifts per image is 73, 51, 40, 32 and 27 pixels, respectively. Each case (with a certain number of scan line shifts per image) is repeated a number of times while keeping the spacing constant but modifying the amplitudes and the widths randomly. The amplitudes are taken from a normal distribution with a mean value equal to 1.5 pixels and a standard deviation of 1.75 pixels, motivated by the more frequent observation of positive amplitudes in practice. The widths are taken from a normal distribution with a mean value equal to 7 pixels and a standard deviation of 1.5 pixels. The cases with two to six scan line shifts include 6, 9, 12, 15 and 18 scan line shifts in total for each image triple, while 8, 5, 4, 3 and 3 image triples are tested, respectively. In this way, a total of at least 45 scan line shifts are included for each case.

To each image triple, additional distortion fields, i.e. drift and spatial distortion, are added as well, Fig. 2.11. A radial polynomial of order five ($U_s(\rho) = k_3\rho^3 + k_5\rho^5$ where ρ is the radial distance from the center of the image, and k_3 and k_5 are the degrees of freedom) is chosen to represent the spatial distortion, which resembles the radial distortion of an optical lens [62]. Figs. 2.11a and b show the spatial distortion field in x and y, respectively. Drift in SEM is a continuous phenomenon over time, which progresses while each image is being scanned. The evolution of drift in time is described by a third order polynomial (similar to [28]), as in Fig. 2.11c. This results in a drift field with a form similar to shear in horizontal direction and stretch in vertical

direction. Figs. 2.11d and e show the drift field in x and y in the third image of the triplets, respectively.

Each image triple is used to perform the pre-correlations to identify an initial guess for the positions of scan line shifts and allocate each one to its corresponding image, as explained in Section 2.2.4. Fig. 2.12 shows the results of the pre-correlations, where the success rate in allocating the scan line shifts is the percentage of the scan line shifts allocated correctly. The criteria for assessing the allocation of a scan line shift are: (1) it is allocated to the correct image; (2) the initial guess for its position is within ± 10 pixels of the correct position. Note that the latter tolerance is well below the limit value found in the previous section for the acceptable error in the initial guess (i.e. 80 pixels). Each number of scan line shifts per image corresponds to a certain minimum distance between the scan line shifts, as indicated by the horizontal axis on top of Fig. 2.12. It is observed that upto three scan line shifts per image with a spacing of 51 pixels, all scan line shifts are allocated correctly. Beyond this number, the success rate drops bellow optimal, but it remains well above 60% even for six scan line shifts per image, at a spacing of less than 30 pixels.

The result of the pre-correlations, i.e. the allocation of the scan line shifts, is subsequently used to correlate the first two images in each image triple in order to measure the scan line shift artifacts present in them. The artifact mapping functions, $\boldsymbol{\phi}_f$ and $\boldsymbol{\phi}_g$, are defined based on the scan line shifts detected in the pre-correlations. $\boldsymbol{\phi}_m$ is regularized by first order polynomials. Please note that this mapping function includes, next to mechanical deformation, drift and spatial distortion. These are generally unknown; to mimic this, we use a suboptimal regularization for $\boldsymbol{\phi}_m$, to account for these other artifacts in an average sense, in order to get a better accuracy in scan line shift artifact correction. Fig. 2.13a shows the mean absolute error in the measured scan line shift mapping function, defined as $\bar{\mathcal{E}}_L = \frac{1}{A_\Omega} \int_\Omega |\boldsymbol{\phi}_g(\mathbf{x}) - \boldsymbol{\phi}_{g,ref}(\mathbf{x})|$, where Ω is the region of interest, A_Ω is the area of the region of interest, and $\boldsymbol{\phi}_{g,ref}(\mathbf{x})$ is the reference scan line shift artifact mapping function used to generate the virtual images, in this case images g.

The blue crosses in the graph depict the errors obtained for the image pairs. For each case where all the scan line shifts are allocated correctly (i.e. the cases with two or three scan line shifts per image and one of the cases with four), all the scan line shift artifact fields are measured with a high accuracy as can be expected from global DIC (below or at 0.01 pixels). The cases including initial scan line shift allocation errors finally result in errors in the range of 0.4 to 2.7 pixels depending on the number of wrongly allocated scan line shifts. The brown circles in the graph represent the averaged values. Hence, the method works reliably up to three scan line shifts per image, or 51 pixels of spacing between scan line shifts, and looses accuracy beyond this number.

To put errors in Fig. 2.13a in perspective, we compare them against the distortions present in the uncorrected images. Therefore, Fig. 2.13b shows the relative correction of scan line shifts, which is the ratio of the mean absolute error in scan line shift artifact fields and the mean absolute value of the reference scan line shift fields, used to distort the virtual images, subtracted from one (complete correction) for each case, i.e.

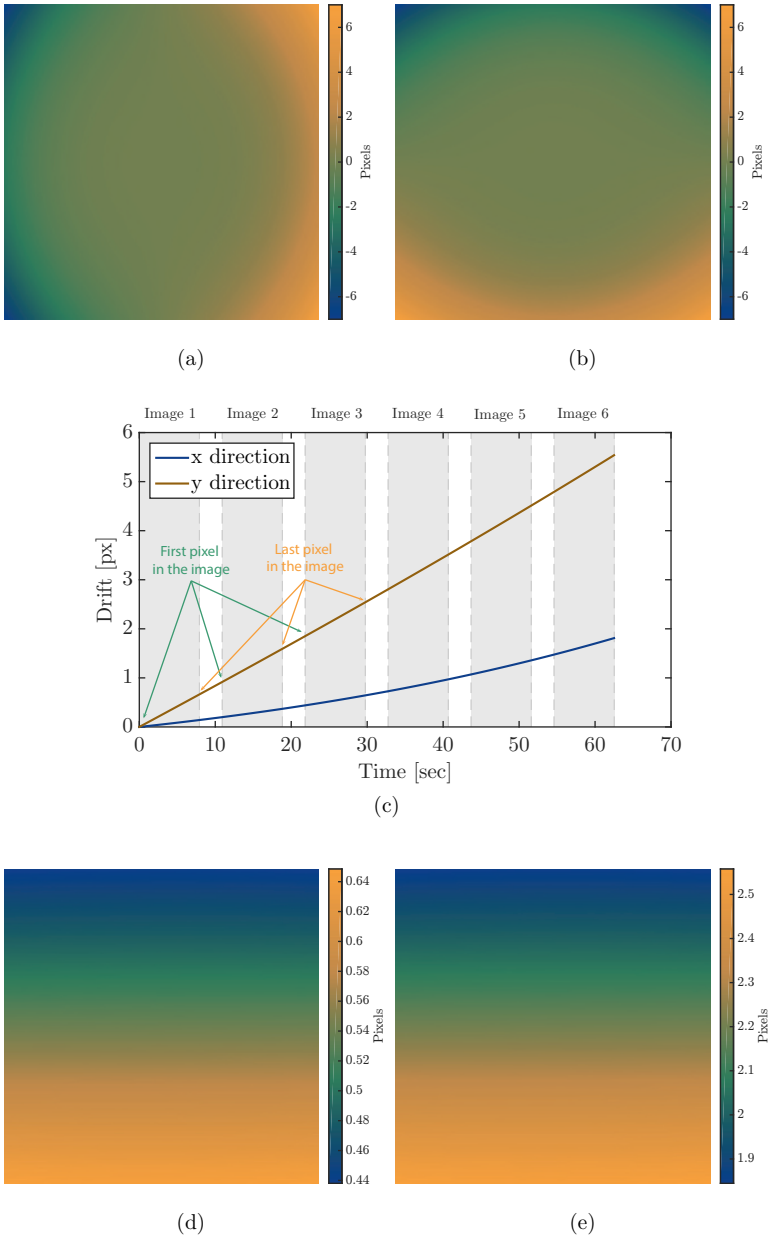

Figure 2.11: Additional artifact fields included in the virtual experiments: (a), (b) spatial distortion in all images of each image triple, in x and y directions, respectively; (c) evolution of drift in time for six images (only the first three are used in Section 2.3.2), where the scanning time of each image is indicated by the shaded areas; (d), (e) drift field in the third image of an image triple, in x and y directions, respectively.

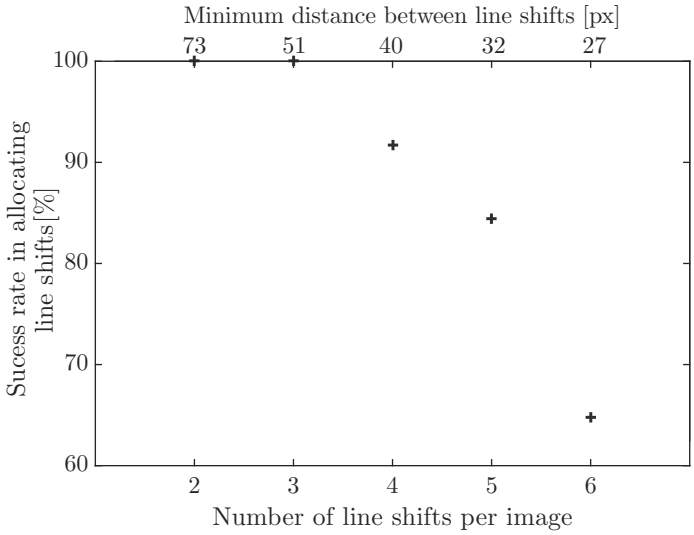

Figure 2.12: Success rate in automatic allocation of the scan line shifts in the pre-correlations for different numbers of scan line shifts per image.

$1 - \frac{\bar{\varepsilon}_L}{\phi_{g,ref}(\mathbf{x})-\mathbf{x}}$. This value represents the percentage of correction the current method provides, relative to the required correction. In the cases with two and three scan line shifts per image, 99.5% correction is achieved. For the cases where the method is less accurate, i.e. with four, five and six scan line shifts per image, 85.6 %, 55.3% and 54.9% correction is still achieved, respectively.

Finally, in order to evaluate the influence of the virtually generated speckle pattern, two extra cases with three line shifts per image are done with two different speckle patterns. In the first case a virtual pattern of only one layer of Gaussian peaks (the finer speckles) is considered, whereas in the second case a pattern from a real SEM image (Fig. 2.18a) is distorted virtually, both confirming the obtained accuracy for the case with two layer Gaussian peak pattern.

The proposed method appears to be reliable and accurate up to three scan line shifts per image, and in the presence of drift and spatial distortion, even though a suboptimal approximation was used for the latter. Thus the method is robust removing scan line shift artifacts for the purpose of geometrical image correction.

2.3.3 Virtual experiments with multiple scan line shifts in the presence of mechanical deformation

Another set of virtual experiments is conducted to evaluate the performance and robustness of the proposed method in the presence of mechanical deformation, drift and spatial distortion. Note that, similar to Section 2.3.2, again a suboptimal description for drift and spatial distortion is used in this section. Fig. 2.14a depicts a typical strain

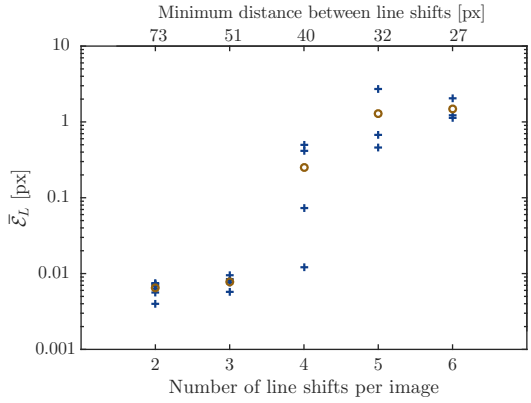

(a)

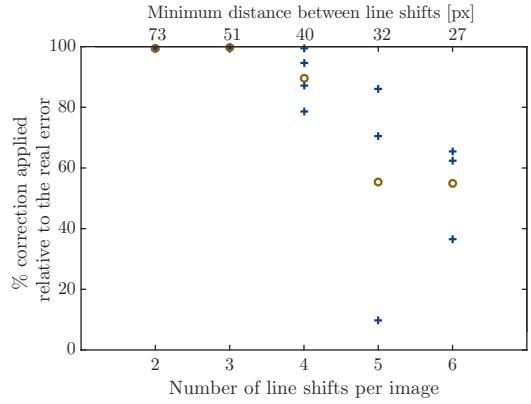

(b)

Figure 2.13: Error in identification of scan line shift artifacts in the virtual experiments with multiple scan line shifts: (a) mean absolute value of the artifact field error averaged over all the scan line shift artifact fields as a function of number of scan line shifts per image; (b) % correction applied relative to the real error in scan line shift artifacts for each case. The blue crosses show the idividul image pairs, while brown circles indicate the averages. The minimum spacing of scan line shifts for each case is indicated by the horizontal axis on top of the graphs.

field, measured using SEM images and local DIC [63], exhibiting high strain gradients and localization bands. The figure depicts the ε_{xx} field, measured from images with a horizontal field width of 85 μm after 0.98 % of macroscopic strain on a René 88DT (a commercial polycrystalline nickel-based super-alloy) specimen. The strains were obtained by local DIC analysis with 21 pixel (0.4 μm) subset size, a 3 pixel step size and a strain window of 15 pixels [63]. The virtual experiments of this section are performed with mechanical deformations generated virtually but representing the main features of the field shown in Fig. 2.14a. i.e. parallel localization bands. These bands are furthermore assumed to span the entire width of the image. This represents the most challenging case for the correction of scan line shift artifacts, since the mechanical deformation field then looks remarkably similar to the scan line shift artifact field particularly at small angles between the localization bands and the scanning direction (horizontal). The effect of orientation of the localization bands will be studied below.

Figs. 2.14b, c and d show the distribution of the three relevant strain components (ε_{xx}, ε_{yy}, ε_{xy}) for the orientation of $\theta = 30^o$. The strain fields represent a background tension of 0.5 % with a Poisson's ratio of 0.5 (no volumetric strain) and shear bands that make a 45^o with the tensile axis. Note that the whole strain state is rotated for each case, keeping the angle between the tension and the localization bands constant. The strain amplitudes, the width (30 pixels), and the spacing (150 pixels) of the bands are close to Fig. 2.14a. A range of $\theta = 90^o$ (vertical bands) to $\theta = 0^o$ (horizontal bands) is considered, of which the latter is the most challenging case when the SEM images are captured using horizontal scan lines.

Note that for the mechanical strain measurement with SEM images, after correcting the scan line shift, it is necessary to correct for the drift and spatial distortion as well. As mentioned before, the method proposed by [25] can be used for this purpose. In order to correct for the drift artifact with this method, two images need to be acquired at each load step. Even though the focus of the current study is not on the correction of drift or spatial distortion, in order to consider a realistic case, the virtual experiments of this section are conducted with the same strategy of using image pairs for each load step.

Fig. 2.15 depicts the structure of the virtual experiments performed for each localization orientation, including six images (three image pairs). The first row in the figure shows the virtual images while the second row sketches the mechanical displacements incorporated in each image pair. The first image pair (load step one) has no mechanics and the next two pairs incorporate the mechanical deformation in two increments. The third row represents the drift and spatial distortion, and the last row represents the scan line shift artifact fields included in the virtual experiments. Three scan line shifts per image are distributed among Images 1, 2 and 3, with equal spacing, as depicted in the figure. The exact same scan line shifts are repeated in Images 4, 5 and 6.

In order to allocate all the 18 scan line shifts in these six images to the correct images and attain the initial guess values for their positions, two pre-correlation steps are performed. The first pre-correlation is done on Images 1, 2 and 3, while the second

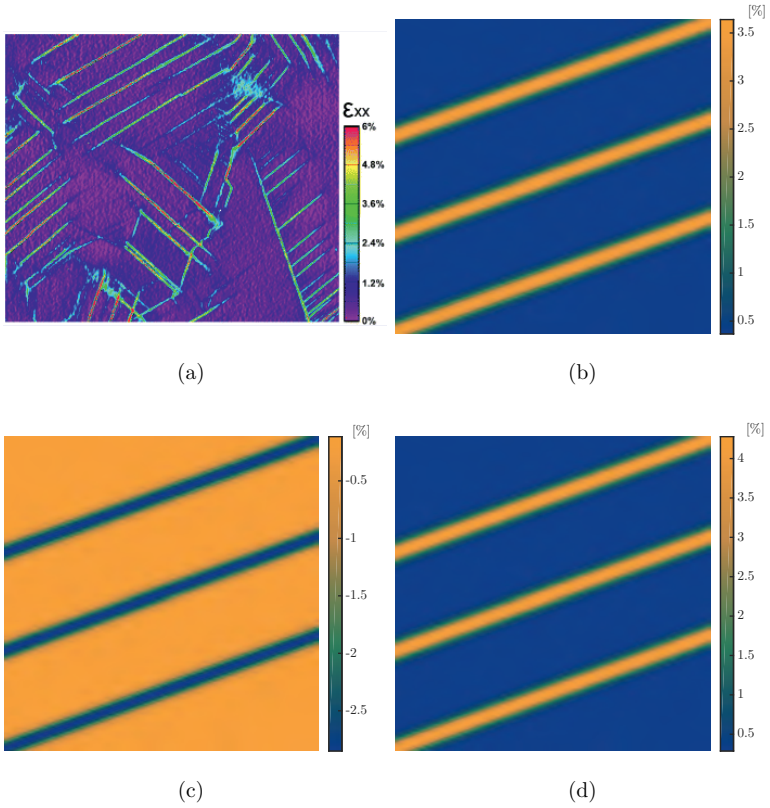

Figure 2.14: Reference mechanical deformation used in the virtual experiments. (a) An example of a DIC measurement on SEM images, taken from the work by [63], exhibiting high strain gradients and localization bands, (b), (c) and (d) ε_{xx}, ε_{yy} and ε_{xy} fields used for the mechanical deformation in the virtual experiments, exhibiting localization bands spanning the whole image, in this figure with an orientation of $\theta = 30^o$.

one is done on images 4, 5 and 6, as shown in Fig. 2.15. Using this procedure, the influence of the mechanical deformation on the pre-correlations is minimized.

Once all the scan line shifts are allocated, three correlations are performed to correct the scan line shift artifacts in image pair 1, 2 (no mechanical deformation present, load step 1), image pair 3, 4 (in the presence of the mechanical deformation of load step 2), and image pair 5, 6 (in the presence of the mechanical deformation of load step 3). Note that these three correlations are performed on image pairs with both images containing the same mechanical deformation field. Accordingly, each correlation can be performed as if no mechanical deformation were present. The only difference that the presence of mechanics is imposing, is in the pre-correlations, since there is one image in the pre-correlations of each of the image triples that contains a different mechanical displacement field, see Fig. 2.15.

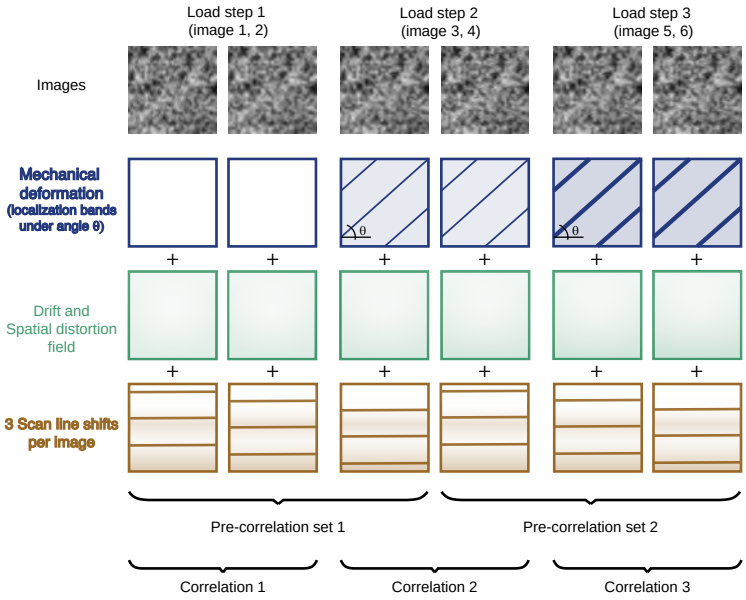

Figure 2.15: Strategy used for performing virtual experiments with multiple scan line shifts per image, in the presence of mechanical strain. Six images (three image pairs) are generated. Each image pair represents a load step, from zero to maximum deformation. Each image incorporates spatial distortion and drift, as well as scan line shift artifacts. Three scan line shifts per image are distributed in Images 1, 2 and 3 as indicated in the bottom row. The exact same scan line shifts are repeated in Images 4, 5 and 6. Two pre-correlation steps are performed to allocate scan line shifts in all the six images, and three correlations are done to correct the scan line shift artifacts in all images. The images for each pre-correlation and correlation case are denoted with curly brackets in the figure, making it clear that the correlations for scan line shift correction are independent of the mechanics.

Fig. 2.16 shows the results of both pre-correlations mentioned above as a function of the localization band orientation θ. The success rate in allocating scan line shifts is the ratio of scan line shifts allocated correctly (using the same criteria as in section 2.3.2) versus the total number of scan line shifts, which is 18 here. It is observed that the localization bands start to cause problems in the pre-correlations only when the orientation is almost horizontal, i.e. less than 10^o. This was anticipated since the horizontal localization bands are very similar to the scan line shifts when they are horizontal, thereby inducing a similar trace in the residual of the pre-correlations. Nevertheless even at $\theta = 0^o$ some of the scan line shifts are allocated to the correct image and position, and the success rate is approximately 60%.

The results of the pre-correlations are used to perform the actual correlations to correct the scan line shifts in the image pairs at constant load. In here, only the results of the correlations on the first image pair (no mechanics) and third image pair (maximum

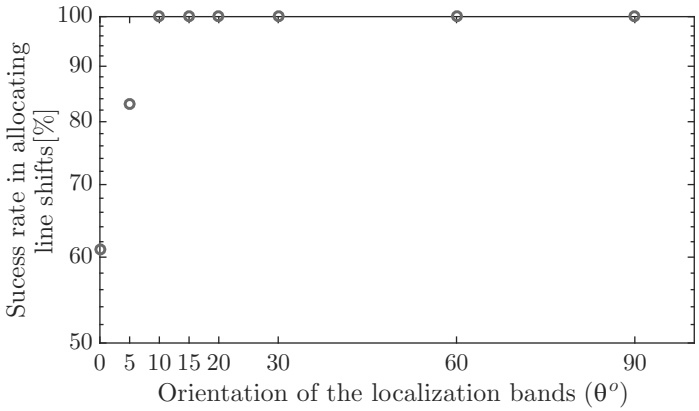

Figure 2.16: Success rate in automatic allocation of scan line shifts in the pre-correlations for different orientations of the localization bands of the mechanical displacement fields for 3 scan line shifts per image.

mechanical deformation) are discussed. The results of the second image pair are fully consistent with the ones from the other two pairs. The artifact mapping functions, $\boldsymbol{\phi}_f$ and $\boldsymbol{\phi}_g$, are defined based on the scan line shifts detected in the pre-correlations. The mechanical deformation has no influence on the correlations and a suboptimal parametrization for drift and spatial distortion is used, i.e. $\boldsymbol{\phi}_m$ is regularized with only first order polynomials to capture the influence of drift and spatial distortion, which is sufficient for an accurate correction of the scan line shift artifacts. Fig. 2.17 shows the mean absolute error in the measurement of scan line shift artifact fields, $\bar{\mathcal{E}}_L$, for different localization orientations. For localization orientations down to $\theta = 10^o$ the scan line shift artifact fields are measured with the expected DIC accuracy (approximately 0.01 pixels) for all images (1, 2, 5 and 6). This means that the scan line shift artifact is corrected more that 99% for all these cases. The error is in the same range for Images 1 and 2 in the case of $\theta = 5^o$. Similar to the results of the previous section, it is confirmed that as long as all the scan line shifts are allocated correctly in the pre-correlations, the correction is performed with high accuracy.

It is observed that the proposed method is robust in the presence of almost horizontal (10^o and more) localization bands spanning the width of the image, even with presence of drift and spatial distortion, that do not need to be accurately captured.

2.4 Application to real SEM images

The method for detecting and removing scan line shift artifacts is next applied to real SEM images. This study is divided into two parts. First, a case without mechanical deformation is discussed, followed by a second case using SEM images taken during an *in-situ* tensile test inside an SEM chamber.

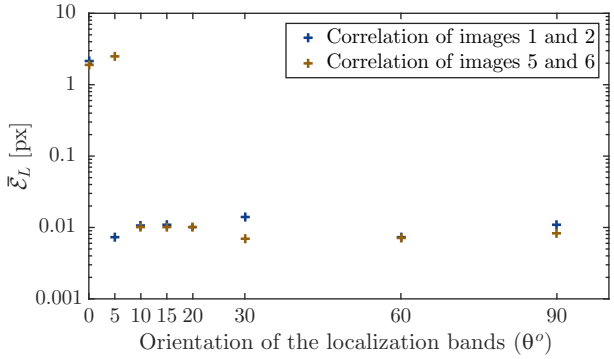

Figure 2.17: Error in the correction of the scan line shift artifact in the presence of mechanical deformation: mean absolute error averaged for all the scan line shift artifact fields for different orientations of the localization bands.

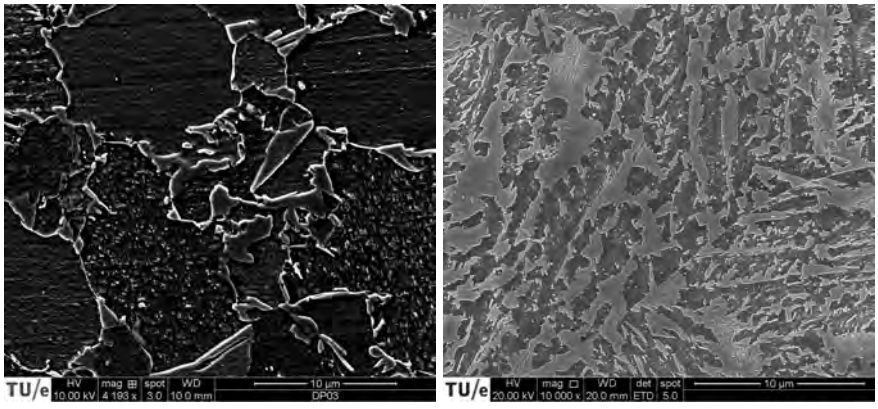

(a) (b)

Figure 2.18: SEM images of (a) a dual phase steel specimen, and (b) a bainitic steel specimen, taken in a FEI Quanta 600F microscope in secondary electron mode. Both types of images have a gray scale pattern which is suboptimal for DIC, thus representing challenging test cases.

2.4.1 SEM images with no mechanical deformation

A set of three SEM images are taken of a Dual Phase (DP) steel specimen in an FEI Quanta 600F microscope in Secondary Electron (SE) imaging mode. The images are taken one after another without any deformation or translation of the specimen. The field of view of the captured images is about $30 \times 30\mu m$, see Fig. 2.18a. The natural pattern present in the images results from etching, resulting in a surface topology that uncovers the microstructure of the material.

A Local Digital Image Correlation (LDIC) between pairs of images is performed using the commercial LDIC package VIC-2D™. A subset size of 41 pixels and a step size of 6 pixels is used for this correlation. Fig. 2.19a shows the vertical displacement map obtained from the LDIC for one pair of images. Two distinct scan line shifts can be observed, with roughly half a pixel amplitudes (in y direction), one in positive, and the other in negative direction.

Next, the same images are corrected for the observed scan line shifts using the proposed method. Firstly, a series of pre-correlations between all three images is performed, resulting in detection of two scan line shifts, one in the first image and the other in the second image. After the allocation of the scan line shifts, the mapping functions of artifacts in f (the first image) and g (the second image), i.e. $\boldsymbol{\phi}_f$ and $\boldsymbol{\phi}_g$ respectively, are assigned. First order polynomials define the mechanical deformation mapping function, $\boldsymbol{\phi}_m$. Since there is no mechanical deformation in this case, this mapping function only captures the difference in drift and spatial distortion artifacts possibly present in the images, enabling a precise detection of the scan line shift artifacts (i.e. the field identified by $\boldsymbol{\phi}_m$ is discarded afterwards). The correlation is performed and both images are corrected for the scan line shifts, thereby effectively eliminating the scan line shifts from the images.

To assess the effectiveness of this methodology, LDIC, with identical settings as used for the uncorrected images, is performed on the corrected images. Local DIC is chosen since it requires no parametrization of kinematic fields, and thus provides a non-biased evaluation of the correction. Note that none of the steps of the proposed method uses local DIC, i.e. all the steps from pre-correlations to the main correlation are based on global formulation of DIC. LDIC is only used here as a method for evaluation of the level of correction attained in real SEM images. Fig. 2.20 presents this difference in an overview: on the left the steps for correcting scan line shift artifacts based on the proposed method (details in Fig. 2.6); and on the right the two LDIC steps for the evaluation of the accuracy of the proposed method. The map of the displacement in y direction thus obtained is depicted in Fig. 2.19b. The effect of the two scan line shifts is completely eliminated from the displacement field. Fig. 2.21 shows the average row values of U_x and U_y as a function of the vertical position of the row for the local DIC results before and after elimination of the scan line shifts. In Fig. 2.21b, both scan line shifts, with amplitudes in y direction equal to 0.55 and -0.49 pixels, respectively, are eliminated completely, i.e. there is no trace left of the sudden increase or decrease of U_y after elimination. The x components of the scan line shifts are eliminated with the

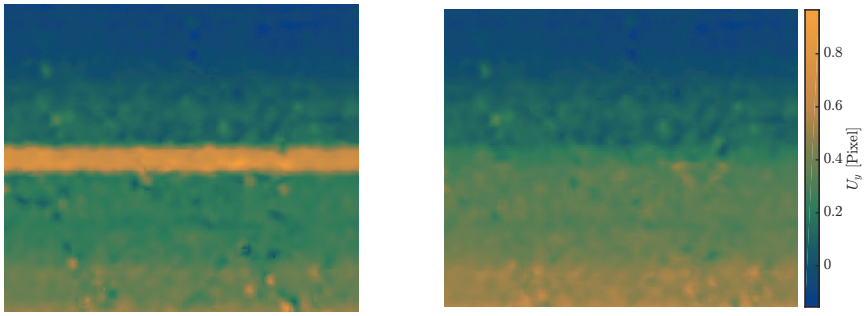

(a) (b)

Figure 2.19: Vertical displacement in measured on an undeformed DP steel specimen before and after scan line shift artifact elimination. Both displacement fields have been determined by LDIC.

same accuracy, as evidenced in Fig. 2.21a.

2.4.2 SEM images of a *in-situ* tensile test

A set of three SEM images with a large scan line shift were available of a bainitic steel specimen, taken during an *in-situ* tensile test in an FEI Quanta 600F microscope in SE imaging mode. The images are from three subsequent deformed states of the specimen, which was subjected to tension in the vertical, y direction. Note that in these prior experiments, no image pairs were taken per loading step, increasing the complexity of the problem. The field of view of the captured images is close to $25 \times 25\mu m$, see Fig. 2.18b. The natural pattern in the image again results from etching, resulting in a surface topology disclosing the microstructure of the material.

LDIC between the first two images is again performed using VIC-2D™. The same settings used before (subset size of 41 pixels, step size of 6 pixels) are adopted for this correlation. Fig. 2.22a shows the vertical displacement map resulting from LDIC. A distinct jump is visible, of a magnitude close to 5 pixels. Note that this is one of the extreme cases of a scan line shift artifact observed with this electron microscope in terms of amplitude and width, making it a relevant test case for validation of scan line shift artifact elimination on real SEM images in the presence of drift, spatial distortion and mechanical deformation.

The proposed procedure is applied to the three images. The pre-correlations revealed that the scan line shift occurs in the second image, thus the correlation for the correction of this line shift artifact is performed with the first two images among the three. Since there is only a single scan line shift corresponding to Image g (the second image), the artifacts mapping function of the reference image, $\boldsymbol{\phi}_f$, can be ignored. One scan line

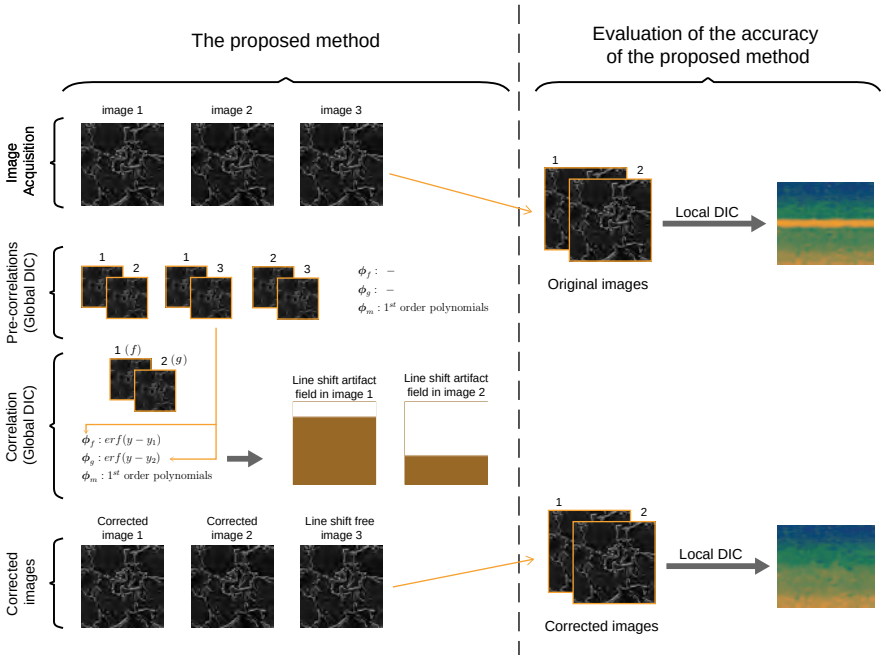

Figure 2.20: An overview of the process of correcting scan line shift artifacts in SEM images (left), and the evaluation of the accuracy of the correction attained by the proposed method (right). Note that LDIC is only used for unbiased evaluation of the accuracy of the proposed method.

shift is allocated to $\boldsymbol{\phi}_g$ with the proper initial guess, obtained from the pre-correlations. First order polynomials define the mechanical deformation mapping function, $\boldsymbol{\phi}_m$. In this case, the mechanical mapping function represents the mechanical deformation in addition to drift and spatial distortion artifacts affecting the images. Again, the purpose is to secure a proper detection and correction of the scan line shift artifact, not the correct measurement of drift, spatial distortion, and mechanical deformation.

The Image g is subsequently corrected for the scan line shift and local DIC is performed on the corrected image with respect to the same reference image. The corresponding vertical displacement map of this correlation is depicted in Fig. 2.22b. An acceptable elimination of the scan line shift artifact is observed, despite the presence of such a strong artifact and mechanical deformation. Note also that the scan line shift is located close to the top edge of the image, which poses no problem for the methodology. Fig. 2.23 reveals the row average of U_x and U_y for the LDIC results, before and after elimination of the scan line shift. The scan line shift of 4.9 pixels amplitude in y direction is properly eliminated. The ratio of the amplitude of the residual of the sudden change in the displacement after elimination to that before elimination is 0.002. The elimination of the scan line shift in the x direction is performed with the same level of precision, as presented in Fig. 2.23a.

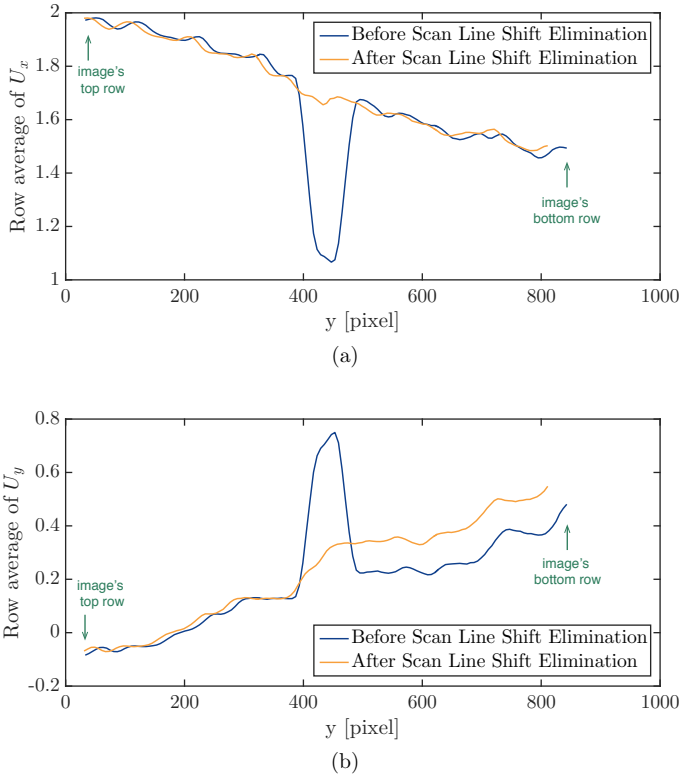

Figure 2.21: Average row values of displacement in (a) x and (b) y direction as a function of the vertical position of the row, found by LDIC on SEM images of a DP steel specimen, before and after elimination of scan line shift artifacts

.

Note that in this case, in contrast with the virtual experiments of Section 2.3.3, the mechanical deformation field is not complex. The limited complexity in the mechanics makes it possible to perform the pre-correlations and correlation successfully without the need for image pairs for each load step.

2.5 Conclusions

Images taken by scanning electron microscopy exhibit artifacts that may result in considerable errors if used for quantitative measurement of, e.g. in-plane geometrical properties or determination of mechanical deformation fields by DIC. These artifacts can be divided into three categories: spatial distortion, drift and scan line shifts. This paper proposes a robust method to deal with scan line shifts, using a systematic approach that does not rely on averaging of images. The nonlinear composition of the effect of

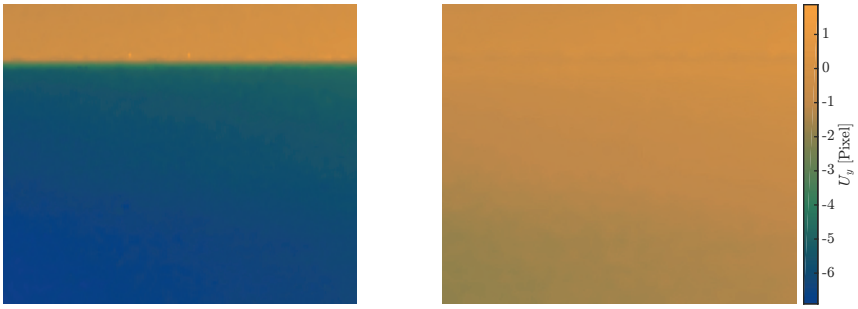

(a) (b)

Figure 2.22: Vertical displacement in a Bainitic steel specimen before (a) and after (b) elimination of the occurring scan line shift artifact (displacements assessed by LDIC).

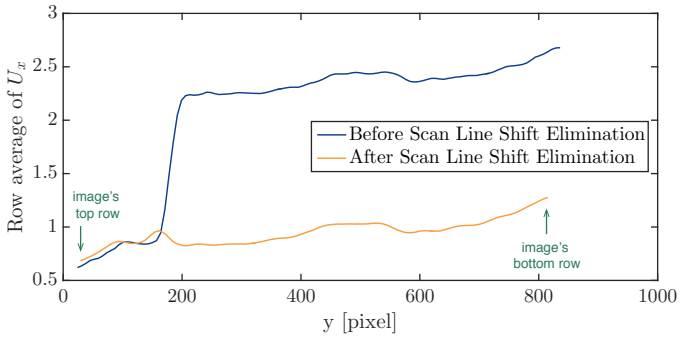

(a)

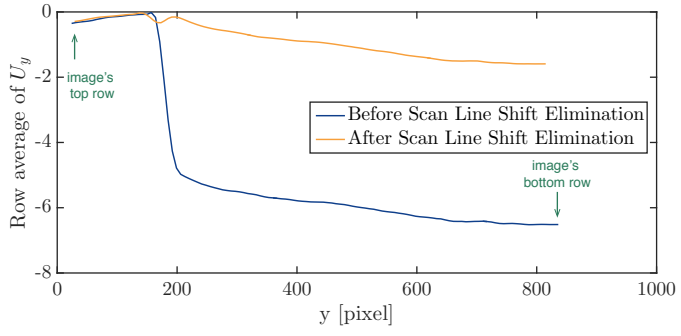

(b)

Figure 2.23: Row average of displacements in (a) x and (b) y direction, obtained by LDIC on SEM images of a Bainitic steel specimen, before and after removal of a scan line shift artifact.

mechanical deformation and the distortions caused by the artifacts is taken into account, leading to an extended global DIC framework suitable for dealing with artifacts. A regularization enrichment based on error functions is proposed to identify scan line shift artifacts and to eliminate them from the affected images.

The method is assessed using a series of virtual experiments based on artificially generated and deformed patterns. The influence of the initial guess of the scan line shift parameters on the robustness and convergence is tested, enabling convergence even with an initial guess error of 80 pixels for the considered virtual test cases. The resulting amplitude of the scan line shifts present an error in the order of 5e−4 pixel in this virtual experiment. The position and the width of the scan line shifts are evaluated with ~ 0.1 and ~ 0.3 pixel accuracy in all virtual experiments, respectively.

The influence of number of scan line shifts and their spacing is studied in a second series of virtual experiments. It is shown that images exhibiting up to three scan line shifts per image can be corrected with an accuracy expected from GDIC (order of 0.01 pixels). The success rate of the scan line shift artifact correction drops to 92%, 84% and 65% for cases of 4, 5 and 6 scan line shifts per image, respectively.

Another set of virtual experiments reveals the influence of a complex mechanical deformation field, exhibiting localization bands in different orientations, on the correction of multiple scan line shift artifacts per image. The correction of three scan line shifts per image is still successfully performed, with ~ 0.01 pixel accuracy, when the orientation of the localization bands is $> 10^o$ different from that of the SEM scanning lines.

The proposed methodology is applied to two sets of real SEM images, one without mechanical deformation and the other taken from an *in-situ* uni-axial tensile test. The images taken reveal scan line shift artifacts up to 5 pixels amplitude. In both cases, all scan line shifts are eliminated accurately. The LDIC maps of the images before and after removal of the scan line shifts emphasize the need for the proposed elimination method and demonstrate the efficiency of the method. The proposed method relies on minimal data acquisition for artifact detection and removal, i.e. no averaging over multiple images is required. The adopted deterministic regularization for this type of artifact results in a high robustness, even when applied to extreme cases of scan line shift artifacts (high amplitude of shifts). The newly proposed extended GDIC general framework based on nonlinear mapping functions for the artifacts in principle can be extended to simultaneously deal with other types of artifact as well, e.g. drift and spatial distortion, which will be discussed in future publications.

Appendices

2.A Automatic algorithm to allocate scan line shifts to images in pre-correlations

A simple algorithm has been established to analyze the pre-correlations automatically and to locate and allocate the scan line shift artifacts to images. Such an algorithm can

be useful if many images are to be analyzed, and specifically when there are multiple scan line shifts occurring in each image. The algorithm is based on the row average of residual fields of three pre-correlations performed on three images, see Fig. 2.5. As mentioned in Section 2.2.4, the high gradients in these curves reveal the presence of a scan line shift artifact. The peaks in the derivative of the row average of these residuals indicate the positions where scan line shifts are occurring. Since numerical differentiation typically provides very noisy data, the curves are first smoothed with a moving average of a 20 pixel window, and the derivative curves are smoothed again with the same parameters. The locations and widths of the peaks of each smoothed residual derivative curve are automatically identified (with the Matlab findpeaks function) and the ones that occur on two graphs within a distance equal to the peak width are paired to allocate a scan line shift to the image which the two pairs have in common. A threshold equal to 1.4 times the average of each curve is set, in order to choose only the peaks that are dominant. It may occur that not all the scan line shifts are captured in one step of the pre-correlations. There are two cases in which this can happen: peaks that are selected on only one curve, or peaks that are selected on all the three curves. If any of these two cases occur, a second pre-correlation is performed automatically. This second set of pre-correlations is enriched with the scan line shifts that have already been allocated, with the position of the scan line shifts fixed to the values found in the first pre-correlation step, and the widths fixed to a large value, i.e. 20 pixels, as described in Section 2.2.4. The second pre-correlation is effective in revealing the scan line shifts that were not identified in the first pre-correlation.

An example of the procedure is shown in Fig. 2.24, where part a depicts the row-averaged residual of the first trial of the pre-correlations of one of the cases of Section 2.3.2 with three scan line shifts per image. Fig. 2.24b and c depict the smoothed derivatives of the residuals for the first and second step of the automatic algorithm as described above. After the first pre-correlation (Fig. 2.24b) there are two peaks at the left and right edge that have been selected only once; therefore, no scan line shifts have been allocated. This triggers the second pre-correlation step, where the same two peaks now occur in two graphs, from which the scan line shifts are correctly allocated to the corresponding images.

Note that neither the parameters chosen in the algorithm (thresholding, smoothing, etc.) nor the algorithm itself are optimized. In spite of this, it proves to be reliable in a good range of number and spacing of scan line shifts, as discussed in Section 2.3.2. Obviously, further optimization might still be possible.

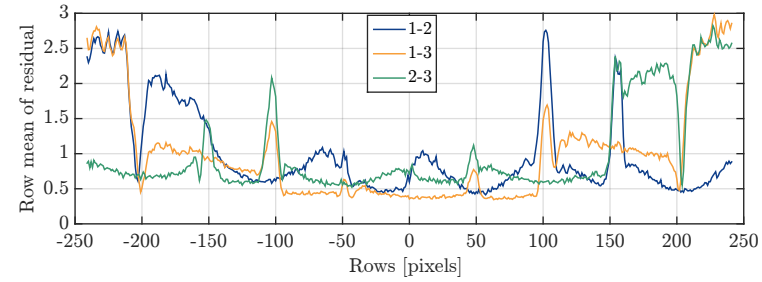

(a)

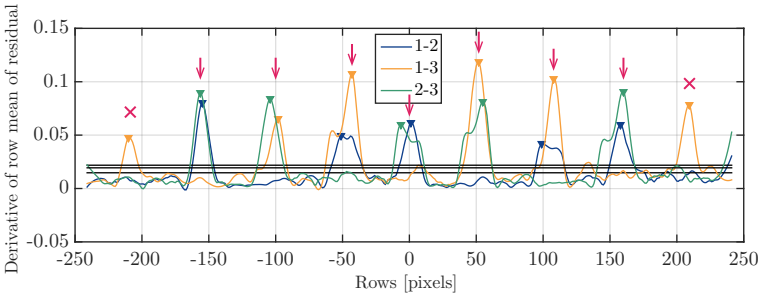

(b)

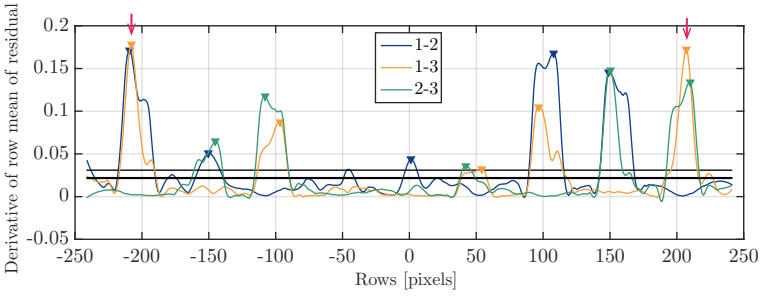

(c)

Figure 2.24: Illustration of the automatic scan line shift allocation procedure: (a) row average of residual fields of first step pre-correlations between three virtual images with three scan line shifts per image; (b) smoothed derivative of the average of residual fields of the first step pre-correlations with the identified peaks indicated by triangles; the arrows and crosses indicate the allocated and unallocated scan line shifts; (c) smoothed derivative of the second step pre-correlations, where the arrows indicate additionally allocated scan line shifts.

Chapter 3

Correction of scanning electron microscope imaging artifacts in a novel digital image correlation framework

Reproduced from:
S. Maraghechi, J. P. M. Hoefnagels, R. H. J. Peerlings, O. Rokoš, M. G. D. Geers
Correction of scanning electron microscope imaging artifacts in a novel digital image correlation framework, *Experimental Mechanics*, 59:489-516, 2019.

Abstract

The combination of digital image correlation (DIC) and scanning electron microscopy (SEM) enables to extract high resolution full field displacement data, based on the high spatial resolution of SEM and the sub-pixel accuracy of DIC. However, SEM images may exhibit a considerable amount of imaging artifacts, which may seriously compromise the accuracy of the displacements and strains measured from these images. The current study proposes a unified general framework to correct for the three dominant types of SEM artifacts, i.e. spatial distortion, drift distortion and scan line shifts. The artifact fields are measured alongside the mechanical deformations to minimize the artifact induced errors in the latter. To this purpose, Integrated DIC (IDIC) is extended with a series of hierarchical mapping functions that describe the interaction of the imaging process with the mechanics. A new IDIC formulation based on these mapping functions is derived and the potential of the framework is tested by a number of virtual experiments. The effect of noise in the images and different regularization options for the artifact fields are studied. The error in the mechanical displacement fields measured for noise levels up to 5% is within the usual DIC accuracy range for all the cases studied, while it is more than 4 pixels if artifacts are ignored. A validation on real SEM images at three different magnifications confirms that all three distortion fields are accurately captured. The results of all virtual and real experiments demonstrate the accuracy of the methodology proposed, as well as its robustness in terms of convergence.

3.1 Introduction

Digital Image Correlation (DIC) is nowadays the most frequently used full-field displacement measurement technique for industrial and academic purposes [3]. Apart from conventional optical images (taken with one or multiple cameras), DIC may be applied to microscopy images obtained by different methods, such as scanning electron microscopy [8], scanning tunneling microscopy [9], atomic force microscopy [10, 11], high-resolution transmission electron microscopy [9, 12], and optical profilometry [7]. These methods provide a high spatial resolution which, combined with the sub-pixel accuracy of DIC [3], enable a high resolution displacement and strain assessment. This opens a vast perspective in experimental micromechanics. Scanning electron microscopy (SEM) has proven itself to be one of the most powerful microscopy methods available. It combines a high spatial resolution (e.g. with respect to light microscopy or optical profilometry) with relative ease of use (e.g. with respect to transmission electron microscopy or atomic force microscopy). However, using SEM images for kinematic measurements comes with a price, due to the presence of several complicated imaging artifacts [55, 56]. These artifacts manifest themselves in the form of distortions in the image, and cause significant artificial deformations and strains in DIC measurements if ignored [25, 28].

SEM imaging artifacts can be categorized into three classes according to Ref. [53]. (1) Random, time-dependent distortion due to positioning errors of the electron beam during scanning, referred to as "scan line shifts". (2) Non-random, time-independent spatial distortion, similar to distortions observed in optical systems. (3) Non-random, time-dependent distortion referred to as drift distortion. It triggers non-uniform artificial deformation fields in images and directly results from the scanning involved in the SEM imaging process [18, 57].

The effect of the above-mentioned artifacts may be reduced by optimizing the SEM scanning parameters. For instance, faster scanning can reduce drift distortions, while lower beam voltage and smaller spot size may reduce charging leading to less drift distortions. However, these alterations do not eliminate the artifacts, while they increase the image noise, which may also reduce the accuracy of the mechanical deformation field to be identified.

In this paper, a novel framework for correcting all three categories of SEM imaging artifacts is presented in a unified and systematic way. The method is fully integrated in a DIC framework and thus yields, at the same time, artifact-corrected images and accurate mechanical deformation fields.

The different types of artifacts have been studied in the literature and some solutions have been proposed to correct them. Several methods have been proposed to correct the drift artifact in SEM images [10, 13–24]. Most of these papers focus only on drift distortion at high magnification, where the effect of drift distortion is more significant than that of spatial distortion. The spatial distortion is discussed in other papers and different solutions are also proposed for correcting it. These studies cover optical microscopy [53, 62, 64] as well as SEM [23, 25–27]. The random, time-dependent scan line shift artifact has been studied much less and is often neglected in the literature.

Lagattu et al. [60] and Stinville et al. [63] report on the presence of this artifact in SEM images and Sutton et al. [28] proposes averaging over a number of images to reduce the detrimental effect of the line shifts. In a previous study by the authors, a more rigorous solution was proposed, based on the enrichment of conventional Global Digital Image Correlation (GDIC) basis functions by error functions; this method was demonstrated to be effective in quantifying the line shifts with amplitudes ranging between $0.5 - 5$ px, and correcting them to less than 0.01 px error [65].

Still lacking in the literature is a systematic unified framework to simultaneously quantify all three types of SEM imaging artifacts along with the mechanical displacement field in an integrated general solution scheme. The methodology introduced by Sutton et al. [25] can be considered ground-breaking, in the sense that, by correcting the DIC displacements it simultaneously deals with spatial and drift distortion and decreases the effect of line shifts (effective for line shifts with amplitudes of up to 1 pixel), but it requires averaging of multiple (as many as 16) scans, and involves many separate optimization steps[1] for characterizing drift and spatial distortion properly. Simultaneously addressing all three artifact types is indeed quite challenging, since one can easily render the methodology ill-posed and non-unique.

The objective of the current study is therefore to fill this gap, and to develop a systematic, stable and unified method to correct for all three types of SEM artifacts in a generic DIC framework.

The three types of SEM artifacts discussed above show a deterministic behavior. Based on this fact, in the current study, Integrated Digital Image Correlation (IDIC) is used to measure these artifact fields alongside the mechanical displacements in a separate manner. Such a measurement will ensure that the artifacts induce minimum errors in the strain measurements. To this end, the imaging process in the SEM as well as the mechanical deformation in the specimen are modeled as a hierarchy of mathematical mapping functions to replace the conventional mapping functions used in IDIC and GDIC. Such a composition of mapping functions enables to uniquely capture the mechanics and artifacts independently. The general framework is not restricted to SEM images and can be equally applied for correcting imaging artifacts for other microscopy methods, whereby the hierarchy of mapping functions needs to be adapted to the specific microscopy technique. Here we focus on SEM imaging and develop the method for it accordingly.

In this study, proper regularization functions are chosen to describe spatial distortion, drift distortion and scan line shifts in SEM images. (1) Line shifts are randomly

[1] Sutton et al.'s method [25] consists of the following steps. Local DIC is performed on image pairs to get drift distortion disparity maps. B-spline surfaces are fitted to these maps. For each pixel separately, the drift velocity in time is found at certain points in time. The drift velocity is fitted with a B-spline function in time. The fitted drift velocity is integrated to identify drift distortion in time. For all pixels, a B-spline surface is fitted to provide a functional for the drift distortion field for one image of each pair. These disparity maps are corrected for drift distortion. A B-spline surface is fitted to these disparity maps resulting in a functional for spatial distortion. The (drift-corrected) disparity maps are corrected for spatial distortion. The whole process is repeated until both drift and spatial distortion are corrected.

occurring and hence are to be extracted from an image when and where they occur (as reported in our previous study [65]). (2) Spatial distortion is independent of time, i.e. equal for all the images. Hence, it can be captured by a calibration phase prior to the mechanical test based on a simple known mechanical field, i.e. rigid body motion [13]. (3) The drift distortion on the other hand is a time dependent phenomenon that is smooth in time [25]. Thus it is defined and regularized in time as a smooth function covering the scanning time of all the images in a mechanical test. The drift distortion as a function of time is projected on the images by the mathematical definition of the scanning process in time [25].

The DIC problem is then solved in a time-integrated manner, correlating all deformation and distortion fields of all images at once [66]. Finally, since all images (including the first one) contain distortions, the existence of an undeformed reference image must be abandoned; therefore, a more general definition of the reference image is introduced, based on the average of all back-deformed images.

The paper presents the methodology in detail, followed by a proof of principle by means of a series of virtual experiments. It will be demonstrated that this framework has several characteristic advantages, justifying the originality of the work:

(i) all artifacts are dealt with in a single unified framework,
(ii) only two correlation phases (spatial distortion calibration and mechanical test phase) suffice to assure that all artifact distortion fields are captured accurately along with the mechanical deformation field,
(iii) the information in all images is optimally used by avoiding any kind of image integration,
(iv) drift distortion is directly measured and corrected in every image, including the first (reference) image, without any extrapolation of data and,
(v) there is no need to correct the images and perform another correlation on the corrected images again; i.e. no pre- or post- processing of images or DIC displacement data is needed.

Table 3.1: Notational conventions

scalar: a	column: $\underline{a}$
vector: $\mathbf{a}$, $\mathbf{A}$	matrix: $\underline{\underline{A}}$
inner product of vectors: $\mathbf{a}.\mathbf{b}$	$\boldsymbol{\nabla}_{\mathbf{x}} = \frac{\partial}{\partial x}\mathbf{e}_x + \frac{\partial}{\partial y}\mathbf{e}_y$
composition of functions : $f \circ g(x) = f(g(x))$	

3.2 SEM imaging artifacts

SEM images are generated by the interaction of an electron beam focused on the specimen surface and registering the out-coming electrons, point by point in a scanning process. The electron beam, after being generated and concentrated by a series of lenses (electromagnetic or electrostatic), follows along the optical axis up to the point where it passes through the scanning coils. Here the electron beam is deflected from the

optical axis in intervals to perform the scanning of the specimen surface. A final electromagnetic lens following the scanning coils focuses the beam onto the specimen surface. The schematic representation in Fig. 3.1a depicts these successive imaging steps.

An error in the deflection of the electron beam in the scanning coils from one scan line to the other is considered to be the main source of scan line shifts [65]. The origin of such errors is not discussed in the literature. A speculative explanation is that, line shifts may be caused by the (sudden) discharge of spurious contamination particles on the wall of the electron column, which gradually charge up over time. Line shift artifacts occur in a random manner, however, they reveal a deterministic flaw in the image. Fig. 3.1b shows how such a mis-positioning of the electron beam is reflected as a local distortion in the image.

The electron beam, which is deflected by the scanning coils to a certain pixel position possibly entailing a scan line shift, now passes through the (final) objective electromagnetic lens. The electromagnetic field of the objective lens is always spatially nonuniform to a certain extent. Thus the beam is further distorted depending on where it passes through the objective lens. In the scanning process, the further the beam passes from the center of the electromagnetic lens, the higher the deviation from the desired magnetic field that acts on the beam, i.e. the higher the erroneous (radial) deflection of the beam. This can be observed in the fact that images with lower magnification generally exhibit more spatial distortion, see Fig. 3.1a. This distortion in the electron beam is assumed to be the source of the spatial distortion artifact, Fig. 3.1c. These distortion fields are well studied in the literature for aberration-corrected electron microscopes [67, 68]. The spatial distortion is assumed to be a time-independent field. This means that as long as the electron beam parameters are not altered, the distortion field is equally affecting all of the images in a series [25].

The drift distortion artifact is a consequence of undesired motion of the specimen relative to the electron beam while the scanning process is going on, see Fig. 3.1d. This smooth time-dependent motion can be caused, for instance, by the motion of the stage or different components of the SEM column (e.g. due to temperature changes), or by global repulsion of the beam due to charging of the specimen that increases in time [69].

Although new microscopes give vast possibilities for scanning procedures, it is common that the scanning is performed row by row, typically from top to bottom of the image, or sometimes column by column. Such a scanning scheme results in distortions which induce apparent tension/compression and shear. The drift distortion field is thus non-uniform in each image, and varies from image to image [25].

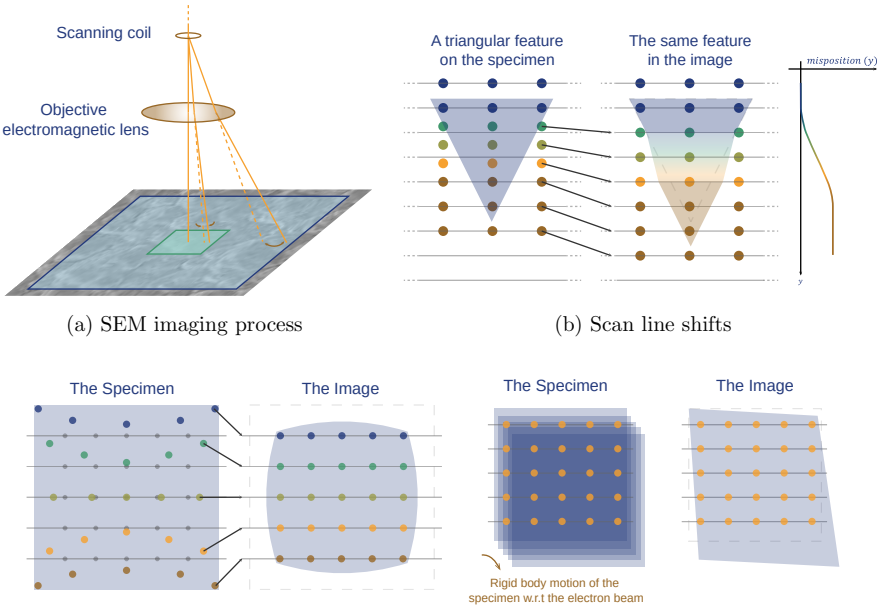

(a) SEM imaging process

(b) Scan line shifts

(c) Spatial distortion

(d) Drift distortion

Figure 3.1: Schematic representation of the origin of SEM imaging artifacts: (a) SEM imaging process and the effect of the inhomogeneous electromagnetic field of the final electromagnetic lens in different magnifications; (b) line shifts: errors occurring in the positioning of the electron beam on the surface of the specimen are reflected as a localized shift in the image (schematic of a zoomed view of a feature on the specimen); (c) spatial distortion: the scanning occurs on the colored dots instead of the correct positions (gray dots) which is reflected in the image as the spatial distortion (schematic of the whole field of view); (d) drift distortion: undesired relative motion of the specimen with respect to the electron beam during scanning results in shear/tension like distortions in SEM images (schematic of the whole field of view). The gray horizontal lines in (b), (c) and (d) indicate the scan lines, i.e. where the scanning should have happened in case of no beam positioning error, thus the pixel positions.

3.3 Methodology

3.3.1 Novel IDIC formulation based on hierarchical mapping functions for SEM artifacts

Images are considered as mathematical projections of a reference pattern. This reference pattern, F, is an ideal, instantaneous (thus not real) image of the specimen, free of any artifacts, at the very first instance $t = 0$ when the scanning of the first image starts. Consider a material point $\mathbf{X}$, on a specimen at this instance, Fig. 3.2a. Due to mechanical deformation and drift (the rigid body motion of the specimen with respect to the electron beam during scanning), this material point will be located in another

position $\mathbf{x}$ at the moment it is scanned in a certain image. The mapping between $\mathbf{X}$ and $\mathbf{x}$ is defined as:

$$\mathbf{x} = \boldsymbol{\phi}_M(\mathbf{X}), \tag{3.1}$$

where subscript M refers to "Motion" in the plane of the specimen. This mapping function incorporates mechanical deformation and drift artifact. On the other hand, the imaging process introduces errors as well. The electron beam landed in position $\mathbf{x}$ while it was supposed to scan another position, $\boldsymbol{\xi}$. This mispositioning is described by a second mapping function that incorporates the imaging artifacts,

$$\mathbf{x} = \boldsymbol{\psi}_I(\boldsymbol{\xi}), \tag{3.2}$$

where the subscript I refers to "Imaging". The position vector $\boldsymbol{\xi}$ indicates the position in the image plane where the gray scale data of the position $\mathbf{x}$ in the specimen is recorded, i.e. $\boldsymbol{\xi}$ is the pixel position, Fig. 3.2a. Note that the mathematical formulations in this section are all in continuous form, however, the final calculations are done in discrete manner since the digital images are constructed of discrete data based on pixels. For the correlation, the pixel position $\boldsymbol{\xi}$ corresponding to each material point $\mathbf{X}$ is needed. To this end, the mapping function in Eq. (3.2) needs to be inverted:

$$\boldsymbol{\xi} = {\boldsymbol{\psi}_I}^{-1}(\mathbf{x}) = \boldsymbol{\phi}_I(\mathbf{x}). \tag{3.3}$$

By combining Eqs. (3.1) and (3.3) the total mapping from each material point to the correct pixel position is attained as:

$$\boldsymbol{\xi} = \boldsymbol{\phi}_I\left(\boldsymbol{\phi}_M(\mathbf{X})\right), \quad \text{or} \quad \boldsymbol{\xi} = \boldsymbol{\phi}_I \circ \boldsymbol{\phi}_M(\mathbf{X}), \tag{3.4}$$

where the symbol "$\circ$" denotes the classical function composition. This hierarchical mapping for a certain image g is depicted in Fig. 3.2b. Note that the pixel position, $\boldsymbol{\xi}$, is not necessarily an integer value, thus requiring interpolation in between pixels to recover the desired gray scale value.

Mapping function for imaging

Let us elaborate on $\boldsymbol{\psi}_I(\boldsymbol{\xi})$ resulting from the SEM imaging process. Based on the order discussed in the previous section, $\boldsymbol{\psi}_I$ is a sequential composition of two mapping functions, the line shift mapping function, $\boldsymbol{\psi}_L$, and the spatial distortion mapping function, $\boldsymbol{\psi}_S$, which for image i results in:

$$\boldsymbol{\psi}_{Ii}(\boldsymbol{\xi}_i) = \boldsymbol{\psi}_S \circ \boldsymbol{\psi}_{Li}(\boldsymbol{\xi}_i). \tag{3.5}$$

Note that $\boldsymbol{\psi}_S$ is constant between images. As in Eq. (3.3), the inverse of the imaging mapping function for image i is:

$$\boldsymbol{\xi}_i = \boldsymbol{\phi}_{Ii}(\mathbf{x}_i) = {\boldsymbol{\psi}_{Ii}}^{-1}(\mathbf{x}_i) = \boldsymbol{\phi}_{Li} \circ \boldsymbol{\phi}_S(\mathbf{x}_i). \tag{3.6}$$

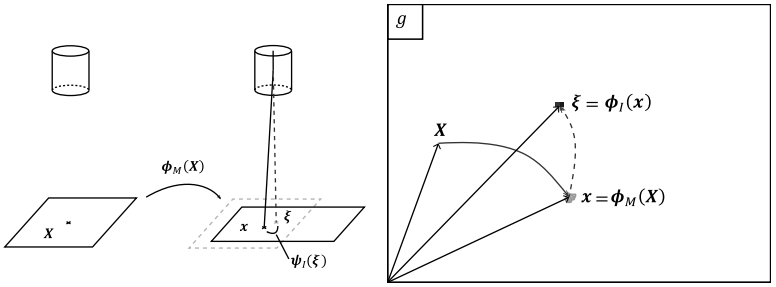

(a) (b)

Figure 3.2: The process of imaging in the SEM and the corresponding mapping functions: (a) a material point $\mathbf{X}$ before starting the first image of a mechanical test ends in position $\mathbf{x}$ at the moment it is scanned due to mechanical deformation and drift (rigid body motion of the specimen with respect to the electron beam), and the electron beam lands in position $\mathbf{x}$ instead of $\boldsymbol{\xi}$ due to imaging artifacts. (b) Projection of the mapping functions on a certain image g showing the hierarchical mapping of material point $\mathbf{X}$ to the corresponding pixel position $\boldsymbol{\xi}$ in this image.

Note that the spatial distortion field is independent of the image, since it is assumed to be time-independent.

Mapping function for motion in the specimen plane

On the other hand the motion mapping function, $\boldsymbol{\phi}_M$, is defined for image i as:

$$\boldsymbol{\phi}_{Mi}(\mathbf{X}, \boldsymbol{\xi}) = \mathbf{X} + \mathbf{U}_i(\mathbf{X}) + \mathbf{D}(t(\boldsymbol{\xi})) \tag{3.7}$$

where $\mathbf{U}(\mathbf{X})$ is the mechanical displacement field and $\mathbf{D}(t)$ is the drift, which is the relative motion of the specimen with respect to the electron beam in time. Note that $\mathbf{U}_i(\mathbf{X})$, which is applied in discrete load increments, may contain a physical rigid body motion of the specimen as well, but this applied discrete rigid body motion does not induce artificial strains, in contrast to the smooth, time-continuous rigid body motion during scanning that is caused by drift. The two fields are separated by constraining the mechanics to be equal for every pair of images (taking two images per load step) while drift distortion is a smooth function in time. This strategy is explained in more detail in Section 3.3.3. Since relative beam-specimen motion triggering drift distortion goes on during the scanning process (and during the time between the images), its value differs from pixel to pixel. Following Ref. [13], these scan times can be projected on the image plane (the pixel positions $\boldsymbol{\xi}$) based on a mathematical definition of the scanning process:

$$t(\boldsymbol{\xi}) = t_i + (t_d \mathbf{e}_x + t_r \mathbf{e}_y) \cdot \boldsymbol{\xi} \quad ; \quad t_r = W t_d + t_j, \tag{3.8}$$

where t_d is the dwell time describing the amount of time spent on the scanning of each single point resulting in a single pixel; t_r is the time required to scan one line while t_j is

the time required to re-position the beam from the end of one scan line to the beginning of the next one; t_i is the elapsed time until the beginning of scanning of image i; W is the width of the image (length of each scan line) in pixels, and $\mathbf{e}_x$ and $\mathbf{e}_y$ are base vectors in x and y direction, respectively. These base vectors are aligned with the horizontal and vertical scanning directions of the SEM. Note that even though Eq. (3.8) is continuous in time, it is probed only at a set of discrete values of time (the scan times) corresponding to the scanning of pixels. This means that even though drift $\mathbf{D}(t)$, is smooth in time, drift distortion for each scan time $\mathbf{D}(t(\boldsymbol{\xi}))$ is by definition never smooth nor continuous (C^{-1}), due to the scanning process that is discontinuous in space. This discontinuity in space is observed in the pronounced change in the drift distortion from the last pixel of one row to the first pixel of the next one.

At the beginning of the first image, corresponding to $t = 0$, the drift is equal to zero. Considering that the first image holds no (imposed) mechanical deformation, it can be concluded that the motion mapping function is equal to unity (position $\mathbf{X}$) at $t = 0$:

$$\mathbf{U}_1(\mathbf{X}) = \mathbf{0} \quad ; \quad \mathbf{D}(t = 0) = \mathbf{0} \quad \Rightarrow \quad \boldsymbol{\phi}_{M1}(\mathbf{0}) = \mathbf{X}. \tag{3.9}$$

Note that, by considering Eq. (3.7), Eq. (3.4) is nonlinear in $\boldsymbol{\xi}$, i.e. an iterative solution is required for each material point $\mathbf{X}$ to find the corresponding $\boldsymbol{\xi}$. To this end, the Picard method can be utilized as a fast iterative solution method:

$$\boldsymbol{\xi}^{P+1} = \boldsymbol{\phi}_{Ii} \circ \boldsymbol{\phi}_{Mi}(\mathbf{X}, \boldsymbol{\xi}^{P}), \tag{3.10}$$

where P refers to an iteration of the Picard solution procedure with an initial guess taken from the previous iteration of the main correlation.

System of equations

Based on the mapping functions defined above (in Eq. (3.4)), the pixel position for each material point can be probed in each image, which results in what is often referred to as the "back-deformed image" denoted by:

$$\tilde{g}_i(\mathbf{X}, \underline{\mathbb{g}}) = g_i \circ \boldsymbol{\phi}_{Li}(\underline{\mathbb{g}}) \circ \boldsymbol{\phi}_S(\underline{\mathbb{g}}) \circ \boldsymbol{\phi}_{Mi}(\mathbf{X}, \underline{\mathbb{g}}), \tag{3.11}$$

where g_i is image i and $\underline{\mathbb{g}}$ is the column of all the degrees of freedom (dof) parameterizing all the mapping functions. Note that only a part of column $\underline{\mathbb{g}}$ is associated with each of the mapping functions, but to avoid notational confusion the full column $\underline{\mathbb{g}}$ is mentioned wherever any dof is present. In absence of noise and if all the mapping functions are known, the difference between the back-deformed images is zero. However, in reality this difference, i.e. the gray scale residual, is minimized for the correct mapping functions. The gray scale residual for each image i is defined as:

$$r_i(\mathbf{X}, \underline{\mathbb{g}}) = g_1 \circ \boldsymbol{\phi}_{L1} \circ \boldsymbol{\phi}_S \circ \boldsymbol{\phi}_{M1}(\mathbf{X}) - g_i \circ \boldsymbol{\phi}_{Li} \circ \boldsymbol{\phi}_S \circ \boldsymbol{\phi}_{Mi}(\mathbf{X}). \tag{3.12}$$

As in Eq. (3.11), all the mapping functions and consequently the residual are functions of all the dofs. For the sake of compactness, however, from here on the column of degrees of freedom $\underline{\mathbb{o}}$ is dropped in the notation of mapping functions. Minimization of the residual would lead to an ill-posed problem unless the number of unknowns is sufficiently reduced by means of regularization to the set of degrees of freedom in $\underline{\mathbb{o}}$, as in Eqs. (3.11) and (3.12). Note that the reference image, here chosen to be the first back-deformed image $\tilde{g}_1$, also incorporates artifacts, and hence it should be probed in correct positions by the corresponding artifact mapping functions.

In order to identify the unknown deformation and distortion fields, residual of all images are stacked to create a column of residual fields, and the sum of squares of this residual column $\underline{r}$ is minimized with respect to the degrees of freedom $\underline{\mathbb{o}}$:

$$\underline{r}(\mathbf{X},\underline{\mathbb{o}}) = \begin{bmatrix} r_1(\mathbf{X},\underline{\mathbb{o}}) \\ \vdots \\ r_i(\mathbf{X},\underline{\mathbb{o}}) \\ \vdots \end{bmatrix} \quad ; \quad \underline{\mathbb{o}}^{opt} = \begin{bmatrix} a_1 \\ \vdots \\ a_k \\ \vdots \end{bmatrix} = \underset{\underline{\mathbb{o}}}{\operatorname{argmin}} \left(\frac{1}{2} \int \underline{r}^{\mathsf{T}}(\mathbf{X},\underline{\mathbb{o}})\, \underline{r}(\mathbf{X},\underline{\mathbb{o}})\, d\mathbf{X} \right), \tag{3.13}$$

where $\underline{\mathbb{o}}^{opt}$ is the set of optimal degrees of freedom minimizing the residual.

The minimization of the sum of squares of $\underline{r}$ implies its derivatives with respect to each degree of freedom to vanish:

$$b_k = \frac{\partial}{\partial a_k} \left(\frac{1}{2} \int \underline{r}^{\mathsf{T}}(\mathbf{X},\underline{\mathbb{o}})\, \underline{r}(\mathbf{X},\underline{\mathbb{o}})\, d\mathbf{X} \right) = 0. \tag{3.14}$$

This is a set of nonlinear equations which is linearized using a Newton-Raphson solution scheme [61]:

$$\underline{b}^{it+1} \simeq \underline{b}^{it} + \underline{\underline{M}}\delta\underline{\mathbb{o}} = 0 \quad \Rightarrow \quad \underline{\underline{M}}\delta\underline{\mathbb{o}} = -\underline{b} \quad ; \quad \underline{\mathbb{o}}^{it+1} = \underline{\mathbb{o}}^{it} + \delta\underline{\mathbb{o}}, \tag{3.15}$$

where $\underline{\underline{M}}$ is the Hessian, defined as:

$$M_{kl} = \frac{\partial b_k}{\partial a_l}. \tag{3.16}$$

The derivative of the objective function with respect to each dof, b_k, is calculated as:

$$b_k = \int \frac{\partial \underline{r}^{\mathsf{T}}(\mathbf{X},\underline{\mathbb{o}})}{\partial a_k} \underline{r}(\mathbf{X},\underline{\mathbb{o}}) d\mathbf{X} = \int \underline{L}_k^{\mathsf{T}}(\mathbf{X},\underline{\mathbb{o}}) \underline{r}(\mathbf{X},\underline{\mathbb{o}}) d\mathbf{X}, \tag{3.17}$$

where $\underline{L}$ for image i and dof k is:

$$L_{i,k}(\mathbf{X}, \underline{\mathbb{0}}) = \frac{\partial r_i(\mathbf{X}, \underline{\mathbb{0}})}{\partial a_k} \tag{3.18}$$

$$= \frac{\partial}{\partial a_k} \left(g_1 \circ \boldsymbol{\phi}_{L1} \circ \boldsymbol{\phi}_S \circ \boldsymbol{\phi}_{M1}(\mathbf{X}) - g_i \circ \boldsymbol{\phi}_{Li} \circ \boldsymbol{\phi}_S \circ \boldsymbol{\phi}_{Mi}(\mathbf{X}) \right) \tag{3.19}$$

$$= L_k^{L_1}(\mathbf{X}, \underline{\mathbb{0}}) + L_k^{S_1}(\mathbf{X}, \underline{\mathbb{0}}) + L_k^{M_1}(\mathbf{X}, \underline{\mathbb{0}}) - L_k^{L_i}(\mathbf{X}, \underline{\mathbb{0}}) - L_k^{S_i}(\mathbf{X}, \underline{\mathbb{0}}) - L_k^{M_i}(\mathbf{X}, \underline{\mathbb{0}}) \tag{3.20}$$

and $L_k^{L_i}$, $L_k^{S_i}$ and $L_k^{M_i}$ are the derivatives of the residual for image i with respect to the particular dof k associated to $\boldsymbol{\phi}_{Li}$, $\boldsymbol{\phi}_S$ and $\boldsymbol{\phi}_{Mi}$. Each derivative is determined by applying the chain rule:

$$\begin{aligned} L_k^{L_i}(\mathbf{X}, \underline{\mathbb{0}}) = & \left[\boldsymbol{\nabla}_{\boldsymbol{\xi}} \left(g_i \circ \boldsymbol{\phi}_{Li} \circ \boldsymbol{\phi}_S \circ \boldsymbol{\phi}_{Mi}(\mathbf{X}) \right) \right] \cdot \\ & \left(\frac{\partial \boldsymbol{\phi}_{L_i}(\mathbf{X}, \underline{\mathbb{0}})}{\partial a_k} \circ \boldsymbol{\phi}_S \circ \boldsymbol{\phi}_{Mi}(\mathbf{X}) \right) \end{aligned} \tag{3.21}$$

$$\begin{aligned} L_k^{S_i}(\mathbf{X}, \underline{\mathbb{0}}) = & \left[\boldsymbol{\nabla}_{\boldsymbol{\xi}} \left(g_i \circ \boldsymbol{\phi}_{Li} \circ \boldsymbol{\phi}_S \circ \boldsymbol{\phi}_{Mi}(\mathbf{X}) \right) \right] \cdot \\ & \left[\boldsymbol{\nabla}_{\boldsymbol{\zeta}} \left(\boldsymbol{\phi}_{Li} \circ \boldsymbol{\phi}_S \circ \boldsymbol{\phi}_{Mi}(\mathbf{X}) \right) \right] \cdot \\ & \left(\frac{\partial \boldsymbol{\phi}_S(\mathbf{X}, \underline{\mathbb{0}})}{\partial a_k} \circ \boldsymbol{\phi}_{Mi}(\mathbf{X}) \right) \end{aligned} \tag{3.22}$$

$$\begin{aligned} L_k^{M_i}(\mathbf{X}, \underline{\mathbb{0}}) = & \left[\boldsymbol{\nabla}_{\boldsymbol{\xi}} \left(g_i \circ \boldsymbol{\phi}_{Li} \circ \boldsymbol{\phi}_S \circ \boldsymbol{\phi}_{Mi}(\mathbf{X}) \right) \right] \cdot \\ & \left[\boldsymbol{\nabla}_{\boldsymbol{\zeta}} \left(\boldsymbol{\phi}_{Li} \circ \boldsymbol{\phi}_S \circ \boldsymbol{\phi}_{Mi}(\mathbf{X}) \right) \right] \cdot \\ & \left[\boldsymbol{\nabla}_{\mathbf{x}} \left(\boldsymbol{\phi}_S \circ \boldsymbol{\phi}_{Mi}(\mathbf{X}) \right) \right] \cdot \\ & \left(\frac{\partial \boldsymbol{\phi}_{Mi}(\mathbf{X}, \underline{\mathbb{0}})}{\partial a_k} \right), \end{aligned} \tag{3.23}$$

where the gradients are with respect to the corresponding subscripts indicated in each case, i.e. $\boldsymbol{\xi} = \boldsymbol{\phi}_{Li} \circ \boldsymbol{\phi}_S \circ \boldsymbol{\phi}_{Mi}(\mathbf{X})$, $\boldsymbol{\zeta} = \boldsymbol{\phi}_S \circ \boldsymbol{\phi}_{Mi}(\mathbf{X})$, and $\mathbf{x} = \boldsymbol{\phi}_{Mi}(\mathbf{X})$. For convenience of implementation, further rearrangements of Eqs. (3.21) to (3.23) are possible, see appendix 3.A. In conventional GDIC, the derivatives of the displacement field with respect to degrees of freedom ($\boldsymbol{\varphi}_k = \frac{\partial \mathbf{U}}{\partial a_k}$) are referred to as basis (or sensitivity) functions. Here, in Eqs. (3.21) to (3.23), the expressions within round brackets are the sensitivity functions, which are the derivatives of the corresponding mapping functions with respect to the degrees of freedom. The $\underline{\underline{L}}$ matrix is finally assembled as:

$$\underline{\underline{L}}(\mathbf{X}, \underline{\mathbb{0}}) = \left[\underline{L}_1(\mathbf{X}, \underline{\mathbb{0}}) \ \dots \ \underline{L}_k(\mathbf{X}, \underline{\mathbb{0}}) \ \dots \right] = \begin{bmatrix} L_{1,1}(\mathbf{X}, \underline{\mathbb{0}}) & \dots & L_{1,k}(\mathbf{X}, \underline{\mathbb{0}}) & \dots \\ \vdots & & \vdots & \\ L_{i,1}(\mathbf{X}, \underline{\mathbb{0}}) & \dots & L_{i,k}(\mathbf{X}, \underline{\mathbb{0}}) & \dots \\ \vdots & & \vdots & \end{bmatrix}. \tag{3.24}$$

From Eqs. (3.16) and (3.17) the elements of the Hessian matrix, $\underline{\underline{M}}$, can be found as:

$$M_{kl} = \frac{\partial}{\partial a_l}\left(\int \underline{L}_k^{\mathsf{T}}(\mathbf{X},\underline{\mathbb{0}})\underline{r}(\mathbf{X},\underline{\mathbb{0}})d\mathbf{X}\right) \tag{3.25}$$

$$= \int \frac{\partial \underline{L}_k^{\mathsf{T}}(\mathbf{X},\underline{\mathbb{0}})}{\partial a_l}\underline{r}(\mathbf{X},\underline{\mathbb{0}})d\mathbf{X} + \int \underline{L}_k^{\mathsf{T}}(\mathbf{X},\underline{\mathbb{0}})\frac{\partial \underline{r}(\mathbf{X},\underline{\mathbb{0}})}{\partial a_l}d\mathbf{X} \tag{3.26}$$

$$= \int \frac{\partial \underline{L}_k^{\mathsf{T}}(\mathbf{X},\underline{\mathbb{0}})}{\partial a_l}\underline{r}(\mathbf{X},\underline{\mathbb{0}})d\mathbf{X} + \int \underline{L}_k^{\mathsf{T}}(\mathbf{X},\underline{\mathbb{0}})\underline{L}_l(\mathbf{X},\underline{\mathbb{0}})d\mathbf{X}. \tag{3.27}$$

The first term in Eq. (3.27) is neglected since it contains the residual, which is small close to convergence [61], resulting in:

$$M_{kl} \simeq \int \underline{L}_k^{\mathsf{T}}(\mathbf{X},\underline{\mathbb{0}})\underline{L}_l(\mathbf{X},\underline{\mathbb{0}})d\mathbf{X}. \tag{3.28}$$

Note that correlation using hierarchical mapping functions takes the same amount of time as a conventional GDIC problem of the same size (in terms of number of images and dofs) if the same assumptions on the image gradient and Hessian approximation are made.

Reference image

Up to this point the first image, g_1, was used as the reference in constructing the residual. This image may be prone to artifacts as well, and it is not more significant than any other image. Hence, a new definition of the reference image is needed, which does not introduce any bias with respect to one of the images. A weighted average of all the back-deformed images is taken to this purpose:

$$f(\mathbf{X},\underline{\mathbb{0}}) := \frac{1}{W}\sum_{j}^{N} w_j \left(g_j \circ \boldsymbol{\phi}_{Lj} \circ \boldsymbol{\phi}_S \circ \boldsymbol{\phi}_{Mj}(\mathbf{X})\right), \tag{3.29}$$

where w_j is the assigned weight to image j and $W = \sum_j^N w_j$. Using this new reference image $f(\mathbf{X},\underline{\mathbb{0}})$, the residual reads:

$$r_i(\mathbf{X},\underline{\mathbb{0}}) = f(\mathbf{X},\underline{\mathbb{0}}) - g_i \circ \boldsymbol{\phi}_{Li} \circ \boldsymbol{\phi}_S \circ \boldsymbol{\phi}_{Mi}(\mathbf{X}). \tag{3.30}$$

By choosing all the weights equal to one, a uniform average of all back-deformed images constitutes the reference image. This is important, specifically in the presence of artifacts where the first image contains distortions and needs to be back-deformed. Note that this definition does not involve an extra computational cost, since all the back-deformed images are needed to construct the residual, regardless of the definition chosen for the reference image. A more elaborate weighing scheme can be considered as well, e.g. weighing based on the inverse of the residuals. Such a scheme emphasizes images that are correlated more accurately, to construct the reference image in each

iteration. The updated reference image implies only a minor change in the definition and assembly of the $\underline{\underline{L}}$ matrix:

$$L_k^{L_i}(\mathbf{X}, \underline{\mathbb{0}}) = \frac{1}{W} \sum_j^N w_j \left(L_k^{L_j}(\mathbf{X}, \underline{\mathbb{0}}) + L_k^{S_j}(\mathbf{X}, \underline{\mathbb{0}}) + L_k^{M_j}(\mathbf{X}, \underline{\mathbb{0}}) \right) - L_k^{L_i}(\mathbf{X}, \underline{\mathbb{0}}) - L_k^{S_i}(\mathbf{X}, \underline{\mathbb{0}}) - L_k^{M_i}(\mathbf{X}, \underline{\mathbb{0}}), \tag{3.31}$$

which is based on the same definitions of $L_k^{L_i}$, $L_k^{S_i}$ and $L_k^{M_i}$ as given in Eqs. (3.21) to (3.23).

Note that using the average of all back-deformed images as the reference image is essential in the presence of artifacts that affect all images, including the first one. In the absence of artifacts, it does not introduce any error compared to using the first image as reference. This is demonstrated on sample 11b of the so-called "DIC challenge" [70] by considering a mesh of 20×10 knots (in x and y direction) of 2^{nd} order B-splines. Obtained results for the two definitions of the reference image differ in terms of displacements less than 3e−4 px, which is well below the DIC accuracy.

3.3.2 Regularization of the artifact mapping functions

The distortion and deformation fields in the mapping functions, Eqs. (3.6) and (3.7), are regularized by restricting this parametrization to a limited set of degrees of freedom. Depending on the expected mechanical deformation, the regularization of the mechanical deformation field may range from a low-order polynomial to a finite element-type discretization of the domain. The regularization for the distinct artifact fields, however, is determined by their nature, as discussed next.

Line shift artifact

In order to specify the line shift artifact field, based on the description given in the previous section and Fig. 3.1b, an error function is used with four degrees of freedom for each line shift. Thus $\boldsymbol{\phi}_L$ in Eq. (3.6) can be written for one line shift as [65]:

$$\boldsymbol{\phi}_L(\mathbf{x}) = \mathbf{x} + \frac{1}{2} \left(A_x \mathbf{e}_x + A_y \mathbf{e}_y \right) \left(1 + \operatorname{erf} \left(\frac{(y - y_0)}{\frac{w}{3\sqrt{2}}} \right) \right), \tag{3.32}$$

where:

$$\operatorname{erf}(z) = \frac{2}{\sqrt{\pi}} \int_0^z \mathrm{e}^{-t^2} dt, \tag{3.33}$$

and $\mathbf{x} = x\mathbf{e}_x + y\mathbf{e}_y$. The degrees of freedom are the amplitudes in x and y direction, A_x and A_y, the position y_0 (the row of pixels where the shift occurs) and the width of the line shift w. The width of the smooth line shift is included as a dof since it has been observed that such line shifts may easily span several scan lines [65].

Spatial distortion

In order to measure spatial distortion with minimal presumptions, a series of locally supported basis functions, such as B-splines, are chosen for regularizing the spatial distortion field. A smooth field of B-splines of order n discretized with m_x and m_y knots in x and y direction is considered:

$$\boldsymbol{\phi}_S(\mathbf{x}) = \mathbf{x} + \sum_{i=1}^{k}\sum_{j=1}^{l} \mathbf{P}_{i,j} R_{i,j}(\mathbf{x}), \tag{3.34}$$

where $k = m_x - n - 1$, $l = m_y - n - 1$, $\mathbf{P}$ contains the components of a control point (i.e. two degrees of freedom) and

$$R_{i,j}(\mathbf{x}) = \frac{B_{i,n}(x) B_{j,n}(y)}{\sum_{p=1}^{k}\sum_{q=1}^{l}\left(B_{p,n}(x) B_{q,n}(y)\right)}. \tag{3.35}$$

Function $B_{i,k}(z)$ is given by:

$$\begin{aligned} B_{i,0}(z) &= \begin{cases} 1 & \text{if } z_i \le z < z_{i+1} \\ 0 & \text{otherwise} \end{cases} \\ B_{i,k}(z) &= \frac{z - z_i}{z_{i+k} - z_i} B_{i,k-1}(z) + \frac{z_{i+k+1} - z}{z_{i+k+1} - z_{i+1}} B_{i+1,k-1}(z). \end{aligned} \tag{3.36}$$

In the case of a point symmetric spatial distortion field, as in spherical aberrations in aberration corrected transmission electron microscopes [67, 68], globally supported basis functions, such as radial or cylindrical [26] polynomials, are chosen to describe this artifact field. The spatial distortion mapping function regularized by a radial polynomial of order n and a cylindrical polynomial of order n_c with fixed orientation θ reads:

$$\boldsymbol{\phi}_S(\mathbf{x}) = \mathbf{x} + \sum_{k=2}^{n} a_{r,k}\left(\mid \mathbf{x} \mid^{k-1} \mathbf{x}\right) + \sum_{k_c=2}^{n_c} a_{c,k_c}\left(\left(\mathbf{x}\cdot\mathbf{e}'_x\right)^{k_c}\mathbf{e}'_x\right), \tag{3.37}$$

where $\mid \mathbf{x} \mid$ is the Euclidean norm, and $\mathbf{e}'_x$ is the rotated base vector defined as:

$$\mathbf{e}'_x = \cos(\theta)\mathbf{e}_x - \sin(\theta)\mathbf{e}_y. \tag{3.38}$$

The origin of the coordinate system is in the center of the image.

Drift distortion

Since drift distortion is defined as a rigid body motion in time projected on images through the scanning process, recall Eqs. (3.7) and (3.8), the regularization of the drift distortion is done in time and not space. Taking into account that drift distortion is a smooth function of time, different choices can be made for its regularization, ranging from polynomials in time with globally supported sensitivity functions with few degrees

of freedom, up to a B-spline discretization of the time domain with locally supported sensitivity functions and typically with more degrees of freedom. The drift distortion field regularized by an n^{th} order polynomial in time is:

$$\mathbf{D}(t) = \sum_{k=1}^{n} \left(a_{2k-1}\mathbf{e}_x + a_{2k}\mathbf{e}_y\right) t^k, \tag{3.39}$$

where t is defined in Eq. (3.8), whereas regularization by a B-spline of order n, that is discretized with the knots $\{t_0, t_1, \ldots, t_m\} \in [0, t_{total}]$, yields:

$$\mathbf{D}(t) = \sum_{i=0}^{k} \left(a_{2i+1}\mathbf{e}_x + a_{2i+2}\mathbf{e}_y\right) B_{i,n}(t), \tag{3.40}$$

where $B_{i,n}(t)$ are given in Eq. (3.36).

3.3.3 Correlation procedure

To properly and uniquely identify the artifact fields, the following systematic procedure is proposed. Because the spatial distortion field is assumed to be time-independent and identical for all images a calibration phase is performed prior to the actual mechanical test in the so-called "spatial distortion calibration phase". In the subsequent "mechanical test phase", the previously measured spatial distortion field $\boldsymbol{\phi}_S$ is kept fixed, and used to directly correct the measurement of the mechanical test itself. Let us first describe the measurement of drift distortion and the scan line shift, as both artifacts need to be identified during these two phases.

Based on the similarity of the drift artifact to tension/compression/shear, for typical SEM scanning schemes, drift distortion needs to be properly distinguished from the mechanical deformations. To this purpose, following [25], two images are taken at each load step. Fig. 3.3a depicts this scheme, where the horizontal axis represents the time, spanning the complete test time, and the vertical axis represents one of the components of the displacement and drift distortion. The shaded areas show the time taken for scanning each image. Considering that drift distortion is smooth and continuous in time, the only difference between the two images in each pair is due to drift distortion, while the deformation shared by the two must be due to the mechanical deformation. So, by constraining the mechanics of each image pair to be exactly identical and defining drift distortion as a smooth and continuous function in time, it is ensured that the mechanical deformation and drift distortion fields can be uniquely identified. This will be also demonstrated in the virtual experiments of Sections 3.4 and 3.5. The only constraint needed for drift is that at $t = 0$ it equals zero as mentioned before in Eq. (3.9). In this artifact corrected IDIC scheme the drift distortion in all images (including the first image) is directly measured and hence, there is no need for any extrapolation of the data, making the results more accurate. Note that both for the "spatial distortion calibration phase" and the "mechanical test phase" it is necessary to capture two images

for each displacement/load step to be able to measure the drift distortion. Additionally, line shift artifacts need to be simultaneously measured, both during the spatial distortion calibration and mechanical test phase. To do so, the line shift mapping function, $\boldsymbol{\phi}_{Li}$, is defined for each image containing any line shift artifacts ($i = 1, 2, \ldots n$). Since the line shift artifact, cf. Eq. (3.32), yields the same result for all positive widths smaller than one (rendering effectively the resulting system ill-posed, recall Eq. (3.32)), the corresponding dofs need to be constrained to be equal to or greater than one pixel. This is in practice achieved by means of a constrained optimization algorithm [71].

The spatial distortion calibration proceeds similar to Ref. [25]: a series of rigid body motions, in both x and y direction, is performed on the specimen, using the SEM stage. The consequence of a rigid body motion is that each area on the specimen experiences a different amount of spatial distortion before and after the motion. This is reflected as a field of artificial deformations which now can be measured based on the composition of the rigid body motion, described by the motion mapping function $\boldsymbol{\phi}_M$, and the spatial distortion, described by $\boldsymbol{\phi}_S$. Since the mechanical interaction is limited to rigid body motion without deformation, any measured deformation results from the spatial distortion only (when the drift distortion and possible line shifts in the calibration phase are measured as well as described above). The rigid body motions in the spatial distortion calibration phase are applied as follows. As depicted in Fig. 3.3b, three steps of rigid body motion are applied consisting of a forward motion in x, a forward motion in y and finally a backward motion in x direction. The maximum applied rigid body motion in each direction is approximately 5% of the field of view (FOV). This is visualized in Fig. 3.3c, where the FOV of the acquired image pairs is shown. Here, a part of the pattern is common to all four image pairs (regions of interest), which is positioned at different locations in individual image pairs (based on the applied rigid body motion). Each one of the colored frames in Fig. 3.3c shows where the region of interest (ROI) is located with respect to the FOV in each image pair. Note that the spatial distortion (as well as the other artifact fields) is defined in the entire FOV (not in the ROI). In order to correlate all the degrees of freedom describing the spatial distortion, all the basis functions need to have their supports in the region of interest of at least one of the considered image pairs. The shaded area in Fig. 3.3c represents an example of a locally supported basis function that satisfies this condition. To guarantee the above condition, the applied rigid body motions need to cover all four corners of the FOV, and hence the spatial distortion field. Area number 1 in this figure is probed four times, whereas areas number 2 (repeated at the four sides of the FOV) and number 3 (repeated at the four corners of the FOV) are probed only twice and once, respectively. The accuracy of the evaluation of the spatial distortion field is therefore much higher in the center (area 1). In order to maximize this area, only a limited rigid body motion should be applied (5 % of the FOV in our case). Based on this fact and since the accuracy of IDIC decreases near the edges (see e.g. Figure 6 in reference [7]), the best practice is to perform the calibration phase at about 10 % larger FOV and evaluate the spatial distortion in the central area (area 1) only. This reduced region then corresponds to the field of view of the images of the mechanical test. Note that since a change of magnification in SEM

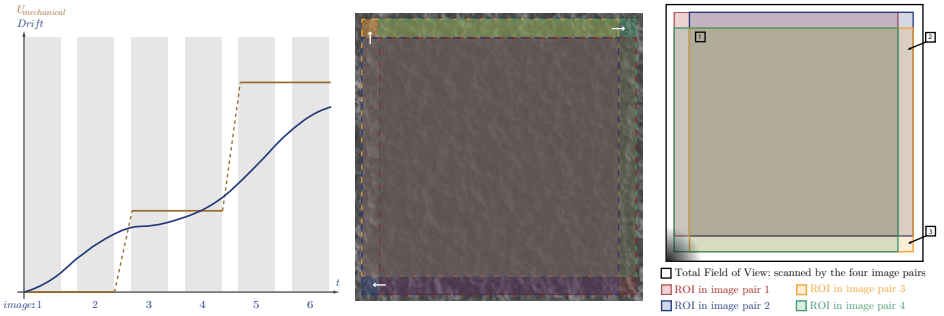

(a) (b) (c)

Figure 3.3: Identification of drift distortion: (a) schematic representation of the time evolution of the rigid body motion of the specimen relative to the beam, resulting in drift distortion and the load step strategy to separate the mechanical deformation from the drift artifact. Identification of spatial distortion: (b) an example of four image pairs with rigid body motions covering four corners of the field of view (FOV) for B-spline regularization of the spatial distortion. (c) Field of view of image pairs and relative positions of region of interest (ROI) in each image pair; in the center (area 1), the spatial distortion is probed by four image pairs, while close to the edges (area 2), and in the corners (area 3) it is probed, respectively, in only two and one image pairs. The shaded corner (bottom left) represents the support of a local B-spline basis function; this support should be contained in the region of interest of at least one of the image pairs to correlate its amplitude in the spatial distortion field.

is performed by scanning over a larger or smaller field of view, as long as the beam parameters are not changed, the spatial distortion can be assumed to be constant in time. In case of globally supported basis functions for the spatial distortion (e.g. radial and/or cylindrical polynomials), it suffices to apply the rigid body motion only in the diagonal direction with a step size of almost 25% of field of view. In order to increase the accuracy of the measurement, the total diagonal rigid body motion is applied in two steps, resulting in three image pairs in total.

Note that the applied rigid body motions need to be controlled with high accuracy (of the order of 0.01 px) to accurately measure the spatial distortion in the calibration phase. Because translational control to such a high accuracy is experimentally unfeasible even with high accuracy positioning systems, rigid body motions are introduced as degrees of freedom in the motion mapping function $\boldsymbol{\phi}_M$ to measure the applied rigid body motions with high accuracy. This has consequences for the measurement of the spatial distortion field. Although zeroth order terms in spatial distortion induce a constant shift in all image pairs, this has no effect on the mechanics (measured through differences between individual image pairs). The first order terms in the spatial distortion induce a constant stretch throughout all images, which results in a zeroth order effect on the mechanics (i.e. an extra artificial rigid body motion). If the applied rigid body motions were known accurately, the first order term of the spatial distortion could be measured, but since

the rigid body motion must be measured as well, the influence of the linear part of the spatial distortion is captured by the motion mapping function $\boldsymbol{\phi}_M$. Therefore, in order to prevent non-uniqueness and hence convergence issues, the spatial distortion mapping function $\boldsymbol{\phi}_S$ is constrained to be orthogonal to constant and linear functions. These constraints are applied on the spatial distortion field by means of Lagrange multipliers.

The separation of the artifact fields from the mechanical deformation field is therefore achievable based on the considerations mentioned above and summarized below:

(i) spatial distortion is a constant field in time (as long as beam parameters are not changed); it is identified during an independent calibration step in which no mechanical deformation occurs (only discrete steps of rigid body motion are applied);

(ii) drift distortion is a continuously evolving, smooth function in time, also during scanning of each image; it is distinguished from mechanical deformation which is applied in a step-wise manner between the acquisition of every two images i.e. mechanical deformation is constant in each image pair;

(iii) scan line shift artifact fields are random localized distortions with a direction dictated by the underlying scanning process; they occur discretely in time, and are distinguished from the mechanical deformation through image pairs similar to drift;

(iv) mechanical deformation is considered as an arbitrary complementary field, constant within a given loading step (i.e. constant for each image pair); i.e. no constraint is enforced on mechanical deformation.

The complete IDIC problem is solved using a Newton-Raphson scheme. The convergence of this minimization method is sensitive to the initial guess. Thus, a procedure is proposed in Appendix 3.B to determine a set of initial guess values that guarantees convergence, starting from a zero initial guess, rendering the methodology robust. The initial guess for two sets of dofs is trivial. Considering the large values of the rigid body motions, the dofs corresponding to these motions need an initial guess that is accurate to within ± 20 px. These values are trivially known, since the rigid body motions are always manually applied in the calibration phase. Line shift amplitudes are always set to 1 px initially, since a zero value for these dofs would result in zero support for the sensitivity functions of the line shift width and position [65].

3.4 Validation by virtual experiments: simple deformation and distortion fields

In order to validate the methodology introduced above, a series of virtual experiments is performed. These have the advantage over real experiments that the exact fields are known and thus the accuracy of the "measured" fields can be assessed rigorously and quantitatively. A validation based on real experimental images is presented in Section 3.7. An artificially generated pattern is deformed to generate virtual images of the "spatial distortion calibration" and "mechanical test" phases. The pattern consists of

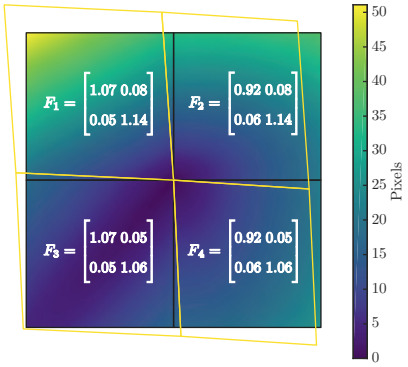

(a)

Line shifts						
image	A_x	A_y	y_0	w		
1	1	2	-50	6		
4	2	-1	50	6		
Spatial distortion						
radial polynomial order	1	2	3	4	5	
dof	0	0	1.5	0	1	
Drift						
polynomial order in time	1	1	2	2	3	3
direction	x	y	x	y	x	y
dof	1	5	.5	.2	.2	.1

(b)

Figure 3.4: Virtual experiment input. (a) Applied virtual mechanical field: amplitude of displacement fields and corresponding deformation field in image 5 and 6, i.e. the last image pair in the series of images for the mechanical test phase. The four quarters indicate areas of constant deformation gradient. (b) Degrees of freedom for the input virtual artifact fields.

three layers of randomly distributed circular Gaussian peaks. Each layer is defined as:

$$F(x,y) = \sum_i a e^{\left(-\frac{1}{2}\left(\frac{(x-\mu_x^i)^2}{\sigma_x^2}+\frac{(y-\mu_y^i)^2}{\sigma_y^2}\right)\right)}, \tag{3.41}$$

where a is the amplitude of each peak, μ_x and μ_y are peak center coordinates (chosen randomly), and σ_x and σ_y are standard deviations in x and y direction. The three layers have amplitudes of 0.3, 0.4 and 0.2 (in a gray scale ranging from 0 to 1), standard deviations of 35, 10 and 1.5 px, and spacings of 70, 15 and 1.5 px, cf. Fig. 3.7.

The calibration phase uses 6 images (3 image pairs). The second and third image pairs have been obtained by applying diagonal rigid body motions of 70 and 140 pixels (corresponding to 27% of the field of view), respectively. Similarly, the mechanical test phase uses 3 image pairs. The first image pair is free of any mechanical deformation, serving as the mechanics reference. The last pair incorporates the mechanical displacement field, the vector amplitude of which is depicted in Fig. 3.4a, and the second pair bears exactly half of that displacement field. The applied deformation corresponds to a piecewise constant strain field, with deformation gradients in the four areas given in Fig. 3.4a. The deformed shape is shown as well. Even though this deformation is rather simple, it looks similar to a typical drift distortion (tension in y direction and shear), thus constituting a challenging case for distinguishing the drift artifact from the mechanics.

All virtual images in the calibration and mechanical test case are also distorted by typical artifact fields. The spatial distortion is equal in both the calibration and

mechanical deformation phase. The drift distortion and line shift artifact fields are identified independently in both phases without mutual influence. Hence, the same artifact fields are implemented in both phases for the sake of simplicity. The virtual artifact fields are applied through the hierarchical mapping functions, replicating the imaging process in an SEM. A third order polynomial in time describes the input virtual drift distortion field. The spatial distortion field, which is applied equally to all the images, is a radial polynomial of order 5. Two scan line shifts are applied, respectively, to image 1 and 4. Note that the existence of a line shift in the first image makes it even more challenging to accurately measure drift distortion in this image. Each line shift is described by a smooth error function with amplitudes up to ± 2 pixels (px) in x and y direction and a width of six pixels. The degrees of freedom corresponding to each of the artifact fields are listed in table of Fig. 3.4b. Finally, Gaussian noise with a standard deviation of 0.1%, 1%, 2%, 5% and 10% is added to all the images, yielding five image series (each with 12 images) with the same deformation and distortion fields, but different noise levels.

In the next subsections, first a correlation case is discussed where the exact same regularization functions as the input distortion and deformation fields are chosen, followed by three studies on the effect of noise, regularization of spatial distortion field and regularization of drift distortion in time.

3.4.1 Correlations with nearly optimal regularizations

The identification of the fields (calibration and mechanical phase) is done on the virtual images with 1% noise using the same regularization of mapping functions that were used to generate the virtual images. This is the optimal choice of regularization since there are the exact number of dofs needed to identify the virtual distortion and deformation fields in the virtual images. To incorporate the rigid body motion in the spatial distortion calibration phase, the mechanical displacement field, $\mathbf{U}$, in the motion mapping function $\boldsymbol{\phi}_M$ is chosen to be constant. For the mechanical test phase, this field is regularized by 4×4 elements of first order B-splines. In both the calibration and test phase, the correlations are initiated with a straightforward initial guess and performed following the steps discussed in Appendix 3.B.

The correlation of the spatial distortion calibration phase is performed with a (trivial) zero initial guess. The convergence is robust and monotonic. In the calibration phase, the spatial distortion field is measured alongside the drift distortion and the line shift artifacts to guarantee the accuracy of the measurement. Figs. 3.5a, b and c depict the amplitude of the measurement error of the artifact fields in the calibration phase. Notations used for the mean absolute value of the vector amplitude of the errors in the measured displacement and artifact fields are: $\bar{\mathcal{E}}_U$, $\bar{\mathcal{E}}_D$, $\bar{\mathcal{E}}_S$, $\bar{\mathcal{E}}_L$ for mechanical displacement (in this phase applied rigid body motion), drift artifact, spatial distortion and line shift artifact fields, respectively. Fig. 3.5a shows the error for the identified drift distortion in the first image. The mean error ($\bar{\mathcal{E}}_D = 0.0005$ px) and the maximum value (0.0009 px) are both well below the accuracy of DIC, which is in the order of 0.01 px,

depending on the continuity of the regularization and the spatial resolution [72]. These very low errors in the first image are explained by the fact that the drift distortion is constrained to zero for the first pixel (top right) of the first image, yielding zero error in this pixel. Note that the measurement of drift distortion in the first image with this accuracy is only possible with the adopted time regularization for drift distortion, Eq. (3.7), and the coupled framework employed in the current study. The error of the spatial distortion is shown in Fig. 3.5b with mean absolute and maximum values of 0.0045 and 0.008 px, respectively. Fig. 3.5c shows the error of the line shift artifact of image 4. The mean error for this field is $\bar{\mathcal{E}}_L = 0.0015$ px. Note that the maximum value of the error in the line shift artifact field is restricted to the width of the line shift. This is due to the slightly lower sensitivity to dofs related to the position and width of line shifts, since the supports of the sensitivity functions related to these dofs are as small as the width of the line shift (a few pixels). The error fields in Fig. 3.5 need to be compared with their corresponding artifact fields. The maximum value of the input artifact fields corresponding to drift distortion in image 1, spatial distortion, and line shift in image 4 are 0.68, 9.9 and 2.23 px, respectively, while the inaccuracy with which these fields have been identified is roughly three orders of magnitude lower. This emphasizes the difference in the scale of the artifacts and the error in evaluating them.

The spatial distortion field measured in the calibration phase (with mean error of $\bar{\mathcal{E}}_S = 0.004$ px) is subsequently used to correlate the images of the mechanical test phase. In this correlation the spatial distortion mapping function is activated, so that the images are directly "corrected" for the spatial distortion effect (with fixed dofs) while the drift distortion and line shift artifacts are measured alongside the mechanics. This step is again initiated with a zero initial guess, entailing robust and monotonic convergence. Fig. 3.6a illustrates the residual field of image 6 (normalized with respect to the dynamic range of the image) in the correlation while Fig. 3.6b shows the same residual if all artifacts are neglected (using conventional GDIC). The mechanical displacement field is measured with high accuracy, see Fig. 3.6c, which shows the amplitude of the error of the mechanical displacement field. The mean absolute value of this error field is $\bar{\mathcal{E}}_U = 0.005$ px. To assess the accuracy of the results, Fig. 3.6d shows the amplitude of the error in the mechanical displacement field, if all artifacts are neglected (using conventional GDIC with the same regularization for the mechanical deformation field). Note that both the mean absolute value of the error and the range of the color bar are more than two orders of magnitude smaller when the artifact corrections are included. Fig. 3.6e and f show the amplitude of error in the drift distortion in the first image (mean error of $\bar{\mathcal{E}}_D = 0.0006$ px) and the line shift artifact in the fourth image (mean error of $\bar{\mathcal{E}}_L = 0.001$ px), respectively. Note again the difference in the mean absolute value and the color bar range of these fields and the case of Fig. 3.6d.

3.4.2 Noise robustness

The same procedure and parameters as described in Section 3.4.1 are used to analyze the image series with different noise levels. For each noise level, first the calibration

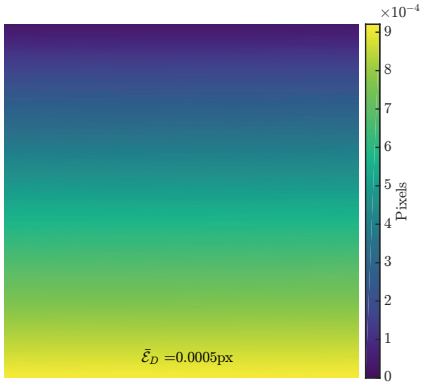

(a) Error in drift distortion

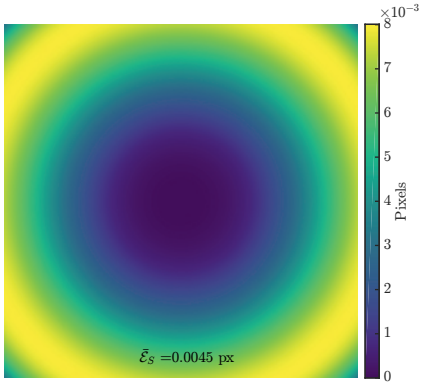

(b) Error in spatial distortion

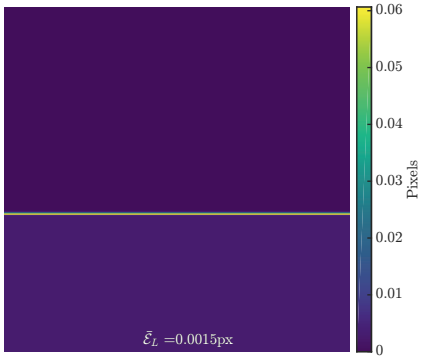

(c) Error in line shift artifact

Figure 3.5: Error fields in the calibration phase: (a) error amplitude of drift measurement in image 1, (b) error amplitude of spatial distortion measurement (c) error amplitude of line shift artifact measurement in image 4.

images are correlated to identify the spatial distortion (with an error that increases with increasing noise level), which is then used to correlate the images of the mechanical test phase. Fig. 3.7 shows the mean absolute value of the error in the mechanical displacement fields of the main test, as a function of the noise level. The proposed methodology remains robust in the presence of noise, which is vital in analyzing SEM images, where the noise levels are typically (much) higher than in optical images. A noise level of 2% results in a mean error in the mechanical displacement equal to $\bar{\mathcal{E}}_U = 0.007$ px, which is remarkably good considering the typical DIC accuracy limits.

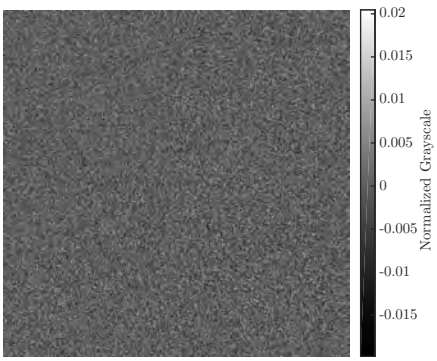

(a) Corrected residual

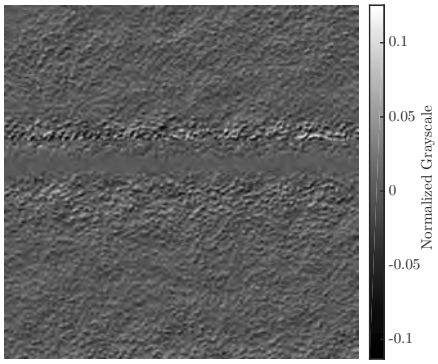

(b) Uncorrected residual

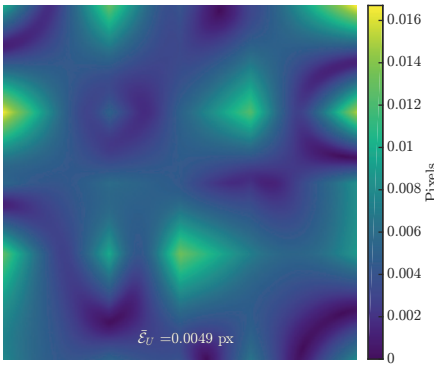

(c) With artifact correction

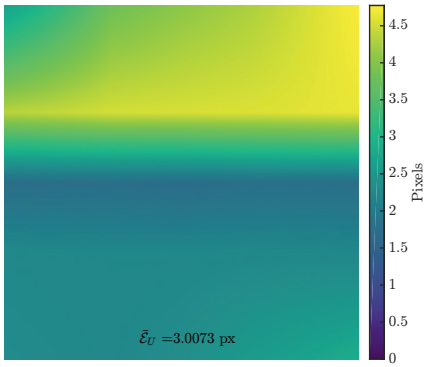

(d) Without artifact correction

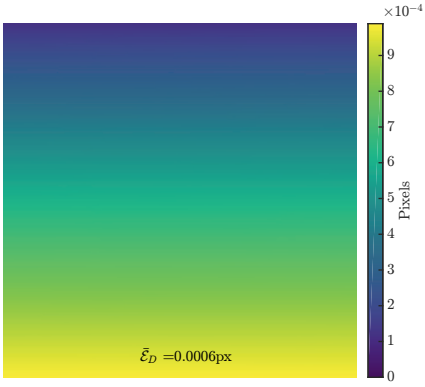

(e) Error in drift distortion

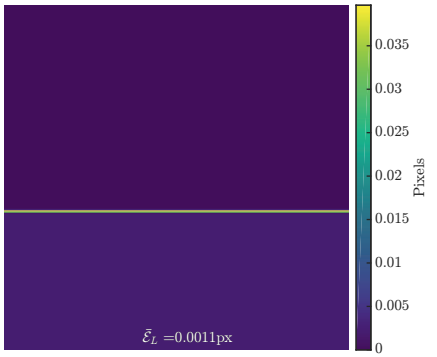

(f) Error in line shift artifact

Figure 3.6: Mechanical test phase results: residual field in image 6 (normalized with respect to the dynamic range of the image) (a) with and (b) without artifact correction. Error amplitude of the mechanical displacement field in image 6 (c) with and, (d) without artifact correction, (e) error amplitude of drift distortion in image 1, and (f) error amplitude of line shift artifact in image 4.

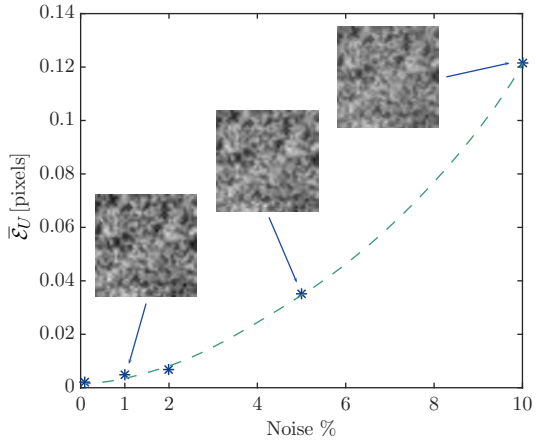

Figure 3.7: Mean absolute value of the amplitude of error in the measured mechanical displacement field as a function of the noise in the images of both the calibration and main test phase, where the noise is defined by its standard deviation as a percentage of the dynamic range of images. The images refer to the virtual patterns for 1%, 5% and 10% of noise.

3.4.3 Spatial distortion regularization study

Using the images with 1% noise, different regularizations of the mapping function for spatial distortion are used to repeat the correlation in the calibration phase. This demonstrates that more general regularization choices for the spatial distortion still lead to high accuracy. The drift distortion and line shift artifact fields are regularized in the same way as in the previous section. Fig. 3.8a depicts the different regularization cases and the mean absolute value of the error amplitude of the measured spatial distortion field for each. In the first three cases, spatial distortion is regularized by radial polynomials. In the last four cases a series of cylindrical functions in both x and y direction are added, e.g. case five includes radial polynomial of order 9, as well as cylindrical functions in x direction of order 3 and cylindrical functions in y direction of order 3, i.e. eight dofs in total. First order terms are not included in the radial nor cylindrical polynomials because of the discontinuity of the gradient fields at the origin, which would trigger convergence problems. Note that both the x and y components of each term of the radial polynomials are anti-symmetric with respect to the y and x axis, respectively. This is opposite to the normal polynomials, where the even order terms are symmetric and the odd order terms are anti-symmetric. Based on this fact, radial monomials of consecutive order have quite similar shapes, which if included all, make the system ill-conditioned or even ill-posed. Accordingly, only odd number order terms of radial polynomials are included in the regularization of the spatial distortion. It is observed, in Fig. 3.8a, that the error in measurement of the spatial distortion field remains in an acceptable range (less than $\bar{\mathcal{E}}_S = 0.018$ px) in the presence of extra radial

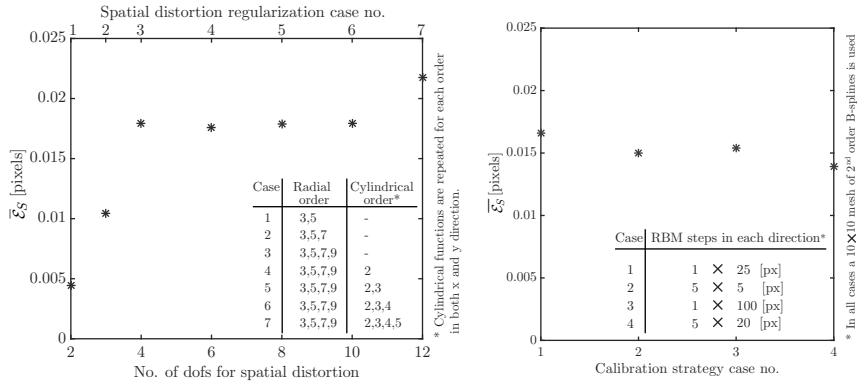

Figure 3.8: Spatial distortion studies: (a) Mean absolute value of the amplitude of the error vector in the measured spatial distortion field as a function of number of degrees of freedom used to regularize the spatial distortion field in the calibration phase. The regularization functions used in each case are described in the legend. (b) Mean absolute value of the amplitude of the error vector in the measured spatial distortion field as a function of strategy used for calibration phase in terms of rigid body motion (RBM) steps conducted. All four cases are correlated with a B-spline regularization of spatial distortion field.

functions in the regularization of the spatial distortion mapping function. Moreover, adding cylindrical functions to the regularization has a negligible effect.

Four additional virtual experiments are performed to study the influence of the number and the magnitude of the rigid body motion steps in the calibration phase, on the evaluation of spatial distortion. In all the cases the images contain only rigid body motions and radial spatial distortions, and the correlations are done using a 10×10 mesh of second order B-splines for spatial distortion and zeroth order polynomials for mechanics. All cases follow the strategy of Fig. 3.3b with rigid body motions given by: (i) one 25 px step in each direction, (ii) five 5 px steps in each direction, (iii) one 100 px step in each direction, and (iv) five 20 px steps in each direction. The error in the evaluation of the spatial distortion in all four cases is equal and in line with the accuracy expected for DIC, see Fig. 3.8b.

3.4.4 Drift distortion regularization study

The images with 1% noise are used to perform a series of correlations (of the mechanical test phase) changing the regularization of drift distortion in time, while using the regularization functions for mechanics, line shifts, and spatial distortion field used in Section 3.4.1. This analysis reveals the accuracy of the mechanical deformation measurements despite the more general (more dofs) regularization of drift artifact. Three cases of polynomials in time (third, fourth and fifth order) and four cases of second

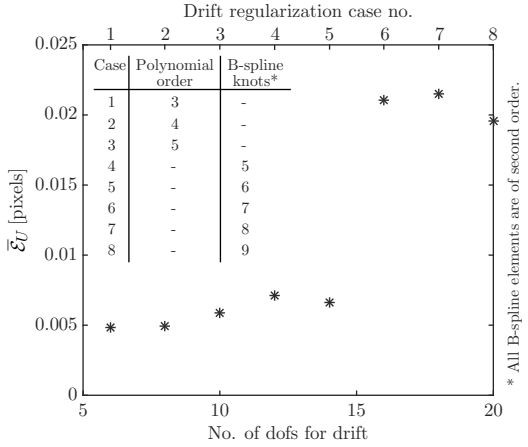

Figure 3.9: Mean absolute value of the amplitude of the error vector in the measured mechanical displacement field as a function of number of degrees of freedom used to regularize the drift artifact field in the mechanical test phase. The regularization functions used in each case are described in the legend.

order B-spline functions in time are used for drift distortion regularization functions, all reported in Fig. 3.9. The B-spline cases consist of different cases of discretization of time with five to nine knots, evenly distributed over time.

The cases of drift distortion regularized with up to 14 dofs (second order B-splines with six knots) result in less than 0.007 px of absolute mean value of error in the measured mechanical displacement field. The error for the higher-order regularization cases is higher but remains around 0.02 px.

3.4.5 Combination of higher order regularizations

A final case is examined, combining the effects of noise and higher order regularization of spatial distortion and drift distortion. Images with 2% noise are used for both calibration and mechanical test phases. The spatial distortion is regularized with the Case 3 of Section 3.4.3 (radial polynomials of order 3, 5, 7 and 9). The spatial distortion found is used for the main mechanical test correlation in which drift distortion is regularized with Case 5 of Section 3.4.4 (second order B-splines in time with six knots). A mean absolute value of the amplitude of error of the mechanical displacement field of 0.019 px results, which is still a good value when compared to the typical accuracy associated with DIC.

3.5 Validation by virtual experiments: complex deformation and distortion fields

The second set of virtual experiments considers a more realistic spatial distortion field, mechanical deformation field, and drift distortion that are all correlated with a generic B-spline regularization, a scan line shift in each image, and more realistic patterns for SEM-DIC.

Fig. 3.10a shows a strain field measured using SEM-DIC by Stinville et al. [63], exhibiting high strain gradients and localizations. The figure reports ε_{xx} measured in a field of view $85\mu m$ of a René 88DT (a commercial polycrystalline nickel-based superalloy) under 0.98% of global strain, which is obtained by stitching several measurements of separate scans. Local DIC with 21 pixel ($0.4\mu m$) subset size, step size of 3 and strain window of 15 pixels was used to make this measurement. The slip band pattern observed in the diagram has inspired the complex mechanical deformation field for the virtual experiments of this section. It features parallel localization bands with an orientation of 45^o that span the entire width of the image, which is a challenging case for the accurate measurement of scan line shifts [65]. Figs. 3.10b, c and d depict a zoomed area of Fig. 3.10a inside which the individual strain components ε_{xx}, ε_{yy} and ε_{xy} are shown, corresponding to a background stretch of 0.5% in x and compression of -0.25% in y direction in addition to the 45^o shear bands. The strain amplitudes, the width (60 px) and the spacing (200 px) of the shear bands are closely matching those of Fig. 3.10a. Note that the size of zoomed area as in Figs. 3.10b, c and d is comparable to each scan/DIC measurement used by Stinville et al. [63].

Fig. 3.11a and b show spatial distortion fields that were experimentally measured, from images at 200× magnification, in the work of Sutton et al. [25]. Fig. 3.11c and d show the spatial distortion fields used for the virtual experiments of this section, closely matching those of Fig. 3.11a and b.

A third order polynomial in time (similar to Sutton et al. [25]) is used to describe the drift distortion, cf. Fig. 3.11e, and one scan line shift is present in each image. The line shifts are equally spaced and distributed among the images. Their amplitudes in both x and y direction are randomly chosen from a normal distribution with a mean of 1.5 px and a standard deviation of 1.75 px. The widths are taken from a normal distribution with a mean of 7 px and a standard deviation of 1.5 px. The parameters used for generating the scan line shifts are listed in Fig. 3.11f.

The images for the spatial distortion calibration phase are generated as described in Section 3.3.3 with rigid body translations of 25 px (corresponding to more than 4.2% of the field of view). The subsequent mechanical test phase consists of three image pairs. The last image pair carries the full mechanical deformation (as depicted in Fig. 3.11), the second image pair contains half of this deformation, whereas the first pair is undeformed.

In order to measure complex mechanical fields with high strain gradients, a fine discretization of the 2^{nd} order B-spline mesh is required. This makes the problem more

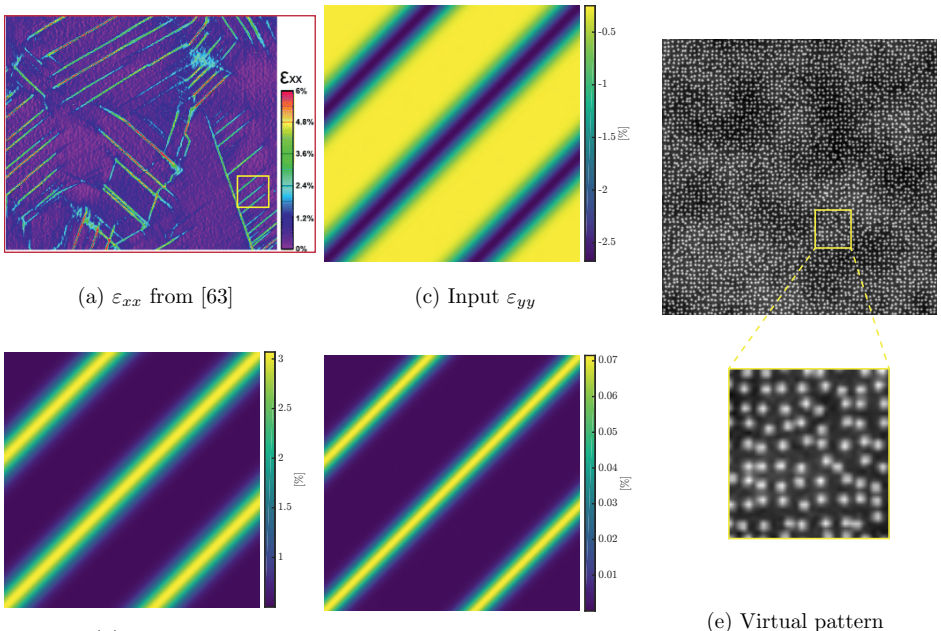

(a) ε_{xx} from [63]

(c) Input ε_{yy}

(b) Input ε_{xx}

(d) Input ε_{xy}

(e) Virtual pattern

Figure 3.10: Reference mechanical deformation, taken from [63], used in the "complex" virtual experiments. (a) An example of a DIC measurement on SEM images, taken from [63], exhibiting high strain gradients and localization bands. The yellow frame depicts the zoomed area used as the reference mechanical deformation in the "complex" virtual experiments. (b), (c) and (d) The ε_{xx}, ε_{yy} and ε_{xy} fields used for the mechanical deformation in the virtual experiments of this section, exhibiting localization bands spanning the whole image with an orientation of 45^o, in addition to a background stretch of 0.5% in x and compression of -0.25% in y direction. (e) Virtually generated pattern used in Section 3.5, and the zoomed view.

sensitive to the virtual pattern used in the images, which is generated as follows. The first two layers consist of randomly distributed circular Gaussian peaks with amplitudes of 0.2 and 0.1, standard deviation of 35 and 10 px, and spacings of 70 and 20 px, respectively. The last layer is generated by a randomly perturbed regular grid of isotropic Gaussian peaks of 0.7 amplitude and a standard deviation of 1.5 px. The considered grid has a spacing of 8 px, whereas the position of each speckle is perturbed by a random value between -2 and 2 px, cf. Fig. 3.10e. The higher contrast and the more unified distribution of the finest speckles makes this pattern more suitable for the evaluation of the proposed method with complex deformation and distortion fields. Moreover, this pattern is more realistic for SEM-DIC, where micro or nano particles are used [8], while there are always some long-range brightness variations due to e.g. different crystals in a poly-crystalline material. Images of 583×583 and 513×513 px with 1% noise level are

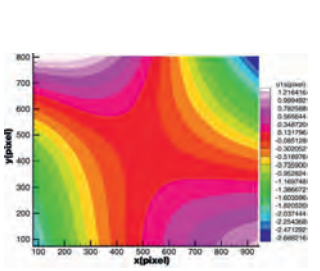

(a) Reference spatial distortion - x

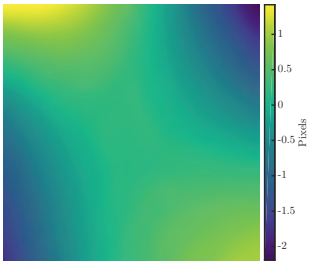

(c) Input spatial distortion - x

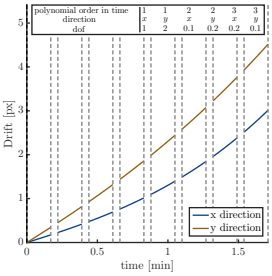

(e) Input drift distortion

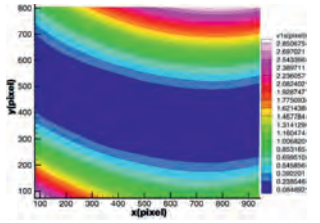

(b) Reference spatial distortion - y

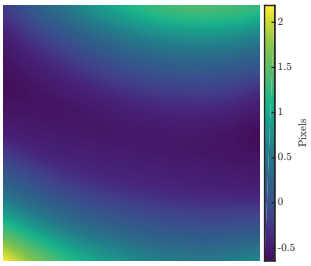

(d) Input spatial distortion - y

Line shifts DOFs (calibration)				
image	A_x	A_y	y_0	w
1	0	3	-226	3.0
2	2	1	-162	3.0
3	1	1	-97	3.5
4	0	4	-32	4.0
5	0	1	32	3.0
6	2	-2	97	4.0
7	2	-1	162	3.5
8	1	2	226	3.0
Line shifts DOFs (mechanical test)				
image	A_x	A_y	y_0	w
1	3	0	-183	3.5
2	2	2	-110	4.0
3	1	2	-37	4.0
4	-1	2	37	4.0
5	1	2	110	4.0
6	2	2	188	4.5

(f) Parameters of line shifts

Figure 3.11: Input spatial distortion used in the "complex" virtual experiments: (a) and (b) the SEM spatial distortion fields in x and y direction experimentally measured by Sutton et al. [25]; (c) and (d) the spatial distortion fields used for the complex virtual experiments in x and y direction, respectively, matching the fields of (a) and (b). (e) Evolution of drift distortion in time and, (f) list of parameters characterizing the line shift artifacts, used for the generation of all the virtual images in the calibration (four image pairs) and mechanical test phases (three image pairs).

generated for the calibration and mechanical test phases, respectively — recall Fig. 3.3c and the discussion therein.

The spatial distortion field is regularized by a 10×10 mesh of second order B-splines. The edge and corner elements are chosen to be twice as large as the remaining ones to reduce the higher sensitivity to the edges. A 30×30 mesh of second order B-splines is used to parametrize the mechanical displacement field, where a ratio of 1.5 is used to scale the edge elements. Drift is regularized in time by 6 knots of second order B-splines (case 5 in Fig. 3.9), in both the calibration as well as the mechanical test phase. Scan line shifts are all identified and assigned to the corresponding images in a pre-correlation step for both the spatial distortion calibration and the mechanical test, see Appendix 3.B. The error function of Eq. (3.32) is used to define the line shift mapping function for each image. In both the calibration and test phase, the correlations are initiated with straightforward initial guesses and performed following the steps discussed in Appendix 3.B.

Fig. 3.12a and b show the error in the determination of the spatial distortion field in the calibration phase, in x and y direction. The mean absolute value of these errors over the central area of the field of view (area 1 in Fig. 3.3c, which is the measured area for the mechanical test phase) are $\bar{\mathcal{E}}_{S_x} = 0.012$ px and $\bar{\mathcal{E}}_{S_y} = 0.024$ px for the x and y direction respectively.

The error in the resulting mechanical displacement field, obtained from the mechanical test phase, is reported in Fig. 3.12c and d. The mean values of these error fields are $\bar{\mathcal{E}}_{U_x} = 0.012$ px and $\bar{\mathcal{E}}_{U_y} = 0.009$ px, which is approximately equal to the general DIC accuracy, indicating that all artifacts have been captured with high accuracy. For comparison, the errors in the mechanical displacement field for the case where the artifacts are ignored are shown in Fig. 3.12e and f. The mean absolute values are, $\bar{\mathcal{E}}_{U_x} = 0.897$ px and $\bar{\mathcal{E}}_{U_y} = 0.415$ px, i.e. a factor of 75 and 46 higher, thereby underlining the importance of proper artifact correction.

Figs. 3.13a, b and c depict the error in the measurement of the ε_{xx}, ε_{yy} and ε_{xy} strain components by the proposed artifact corrected framework. The mean values of these errors are $\bar{\mathcal{E}}_{\varepsilon_{xx}} = 0.06\%$, $\bar{\mathcal{E}}_{\varepsilon_{yy}} = 0.05\%$ and $\bar{\mathcal{E}}_{\varepsilon_{xy}} = 0.03\%$, respectively. Figs. 3.13d, e and f depict the same strain components for the case with ignored artifacts, with mean values of $\bar{\mathcal{E}}_{\varepsilon_{xx}} = 0.16\%$, $\bar{\mathcal{E}}_{\varepsilon_{yy}} = 0.85\%$ and $\bar{\mathcal{E}}_{\varepsilon_{xy}} = 0.87\%$. The considered line shift artifacts typically affect the ε_{yy} and ε_{xy} components and have a negligible effect on ε_{xx}. Note the large localized errors in ε_{yy} and ε_{xy} if artifacts are not corrected for, while no trace of such large errors are found in the corrected case.

3.6 Validation by virtual experiments: application to real SEM patterns

In this section the proposed methodology is validated using virtual experiments in combination with speckle patterns from real SEM images. To this end, the virtual experiments of the previous section (with complex spatial distortion and mechanics obtained from experiments of [63] and [25], respectively) is repeated using the patterns from Fig. 3.14. The same virtual deformation and distortion fields are used to virtually deform the SEM patterns mentioned above, and the mechanical deformation field as well as the artifact fields are measured in the same way. Fig. 3.14a provides a regular SEM-DIC pattern, which is obtained by sputter coating of a silicon substrate by an Indium-Tin target and then heat treated to the melting point of the alloy (98^oC) to create a pattern consisting of spheres [73]. Note that this is only a suitable pattern if used at a high magnification. For the experimental validation in Section 3.7, we also need speckle patterns that are suited for simultaneous analysis at multiple scales. Therefore, a multiscale pattern, based on the fractal growth of copper during electro-deposition, is used as well. Figs. 3.14b, c and d depict this multiscale pattern imaged at three different magnifications corresponding to 10, 50 and 600 μm horizontal fields of view (HFV). The result is an acceptable, though not optimal, DIC pattern at multiple scales.

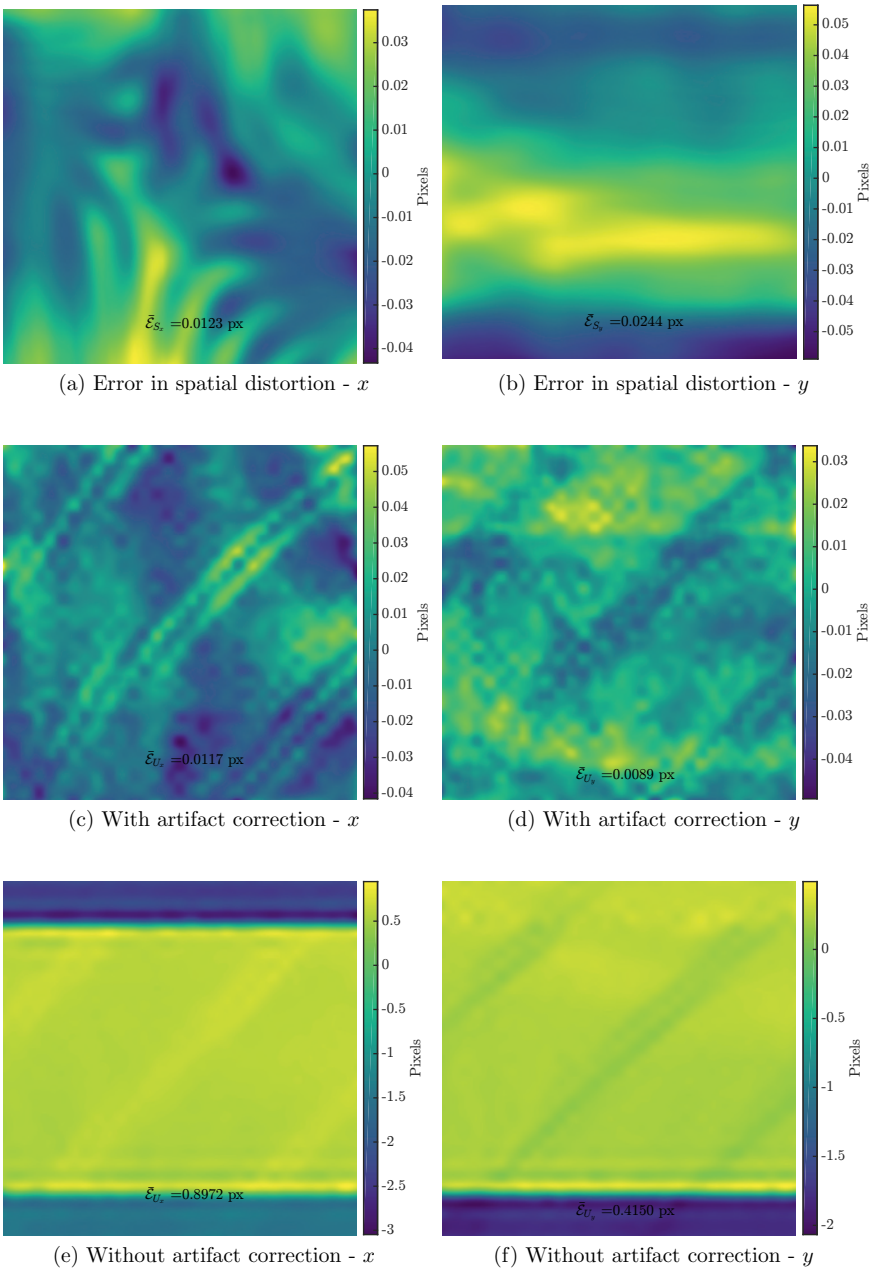

(a) Error in spatial distortion - x

(b) Error in spatial distortion - y

(c) With artifact correction - x

(d) With artifact correction - y

(e) Without artifact correction - x

(f) Without artifact correction - y

Figure 3.12: Error in virtual experiments with complex deformation and distortion fields (input fields taken from [63] and [25]). (a) and (b) spatial distortion, (c) and (d) mechanical displacement with artifact correction, (e) and (f), the error in mechanical displacement without artifact correction (using conventional GDIC with the same discretization for the mechanical deformation field).

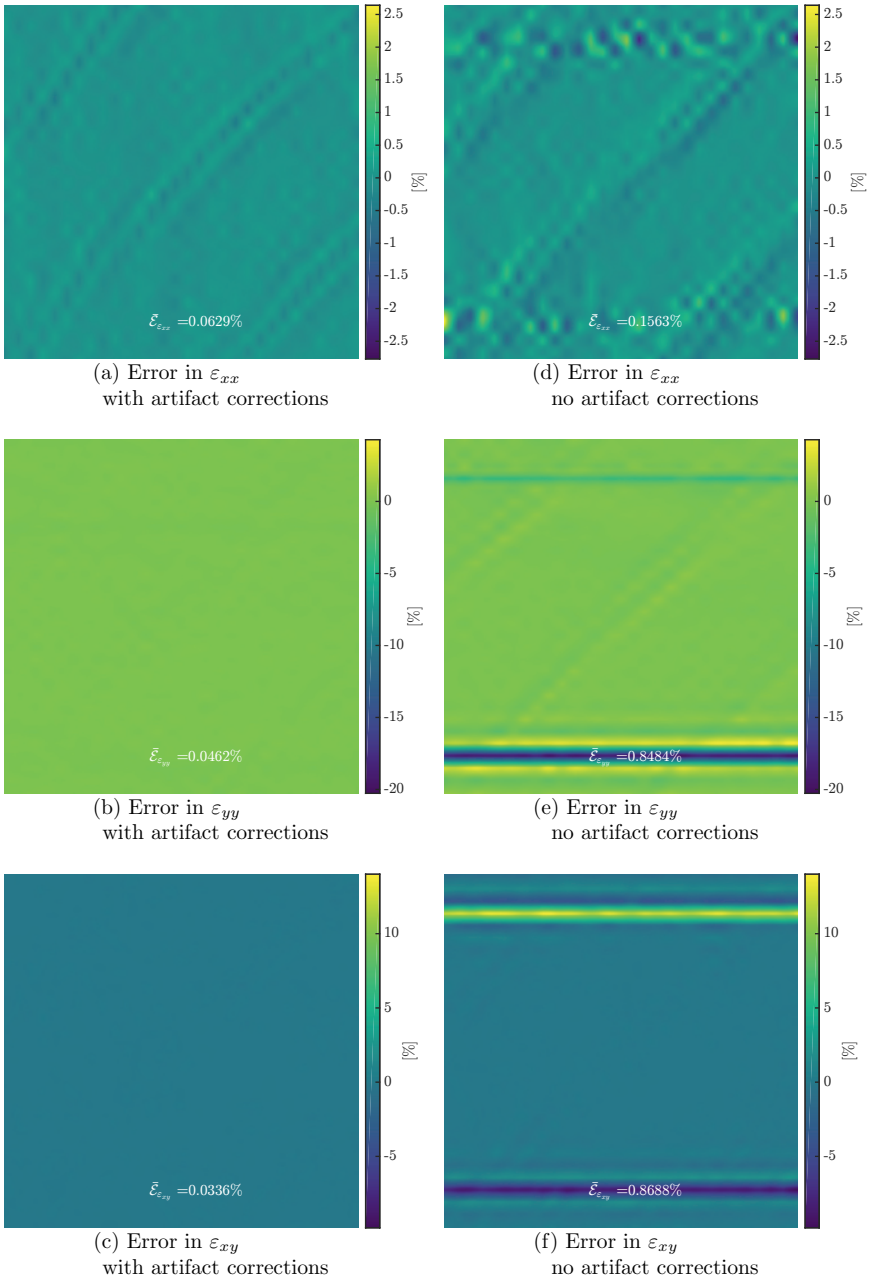

(a) Error in ε_{xx} with artifact corrections

(d) Error in ε_{xx} no artifact corrections

(b) Error in ε_{yy} with artifact corrections

(e) Error in ε_{yy} no artifact corrections

(c) Error in ε_{xy} with artifact corrections

(f) Error in ε_{xy} no artifact corrections

Figure 3.13: Error in strain components in virtual experiments with complex deformation and distortion fields (input fields taken from [63] and [25]). Error in (a) ε_{xx}, (b) ε_{yy} and (f) ε_{xy} with artifact correction. Error in (a) ε_{xx}, (e) ε_{yy} and (f) ε_{xy} without artifact correction (using conventional GDIC with the same discretization for the mechanical deformation field).

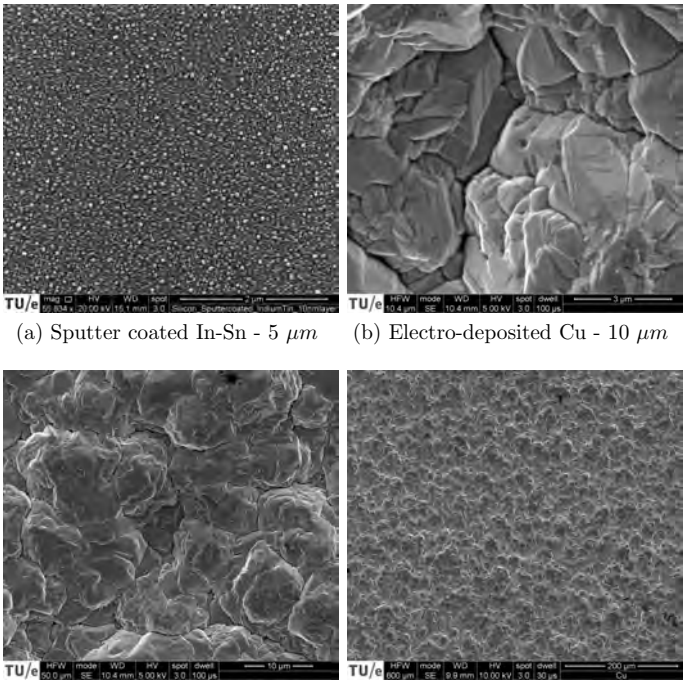

(a) Sputter coated In-Sn - 5 μm (b) Electro-deposited Cu - 10 μm

(c) Electro-deposited Cu - 50 μm (d) Electro-deposited Cu - 600 μm

Figure 3.14: Four realistic SEM patterns used in virtual experiments with complex deformation and distortion fields. (a) regular small scale SEM-DIC pattern obtained by Indium Tin sputter coating on a silicon substrate imaged in HFV of 5 μm. Electro-deposited copper imaged with an FEI Quanta 600 SEM, in secondary electron contrast mode, visualized in three different magnifications corresponding to (b) 10, (c) 50, and (d) 600 μm horizontal field of view (HFV). The fractal growth, resulting from the electrodeposition of copper, provides a natural DIC pattern at different scales.

All images are taken in a FEI Quanta 600 SEM, in secondary electron contrast mode, with 1024×884 pixels. The Indium-Tin sputter coated image is taken at $15mm$ working distance, with $20kV$ beam voltage and $100\mu s$ dwell time. The electro-deposited copper images are taken with 10 mm working distance while the ones with 10 and 50 μm horizontal field of view are acquired with $5kV$ beam voltage and $100\mu s$ dwell time, and the images with $600\mu m$ HFV with $10kV$ and $30\mu s$.

The obtained results for the spatial distortion calibration phase and the mechanical test phase are summarized in Fig. 3.15 for the four real SEM patterns of Fig. 3.14 as well as for the virtual pattern of Fig. 3.10e. In particular, Fig. 3.15a shows the errors in the spatial distortion field $\bar{\mathcal{E}}_S$ (corresponding to the spatial distortion calibration phase), whereas Figs. 3.15b and c show the error in the mechanical displacement $\bar{\mathcal{E}}_U$ and strain field $\bar{\mathcal{E}}_\varepsilon$ (corresponding to the mechanical test phase). In all the three graphs, the vertical axis represents the mean absolute error values, whereas error bars reflect their maxima

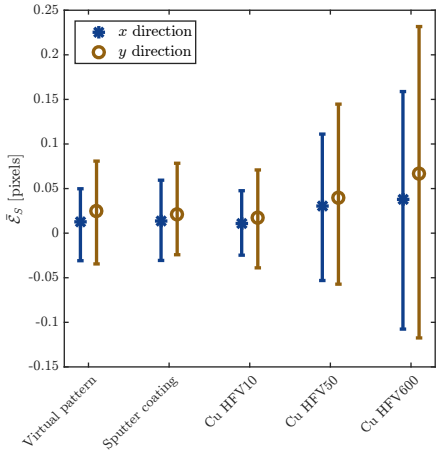

(a) $\bar{\mathcal{E}}_S$

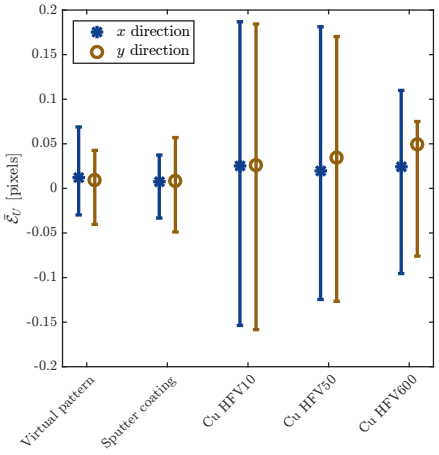

(b) $\bar{\mathcal{E}}_U$

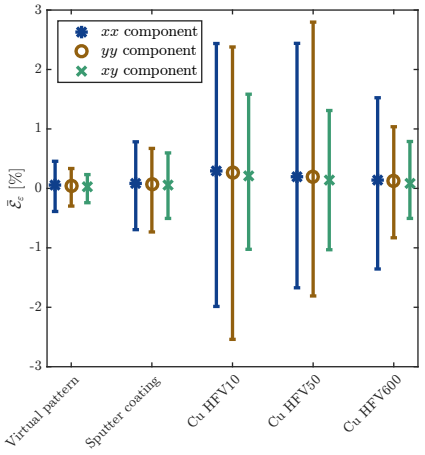

(c) $\bar{\mathcal{E}}_\varepsilon$

Figure 3.15: Influence of the SEM patterns (Fig. 3.14) on the error in (a) spatial distortion, (b) displacement and (c) mechanical strain measurements corresponding to virtual experiments with complex deformation and distortion fields taken from [63] and [25]. The horizontal axis refers to the patterns of Figs. d, (c), (b), (a) and e respectively. The vertical axis represents the mean absolute value of the error, whereas the error bars reflect the minimum and maximum values.

and minima. Clearly, the regular SEM-DIC pattern (in Fig. 3.14a) achieves the same high accuracy as that of the virtual pattern of Fig. 3.10e, showing that the method is not very sensitive to the precise pattern. Indeed, even the suboptimal multiscale pattern (of Figs. 3.14d – b) reveals only a somewhat lower accuracy and higher scatter. Still, the obtained accuracy is adequate for practical purposes. The reduced accuracy with the electro-deposited copper pattern is explained by the fact that these patterns show low local spatial contrast in certain areas. Such local lack of contrast leads to higher error in corresponding elements in the B-spline regularization of both spatial distortion and mechanical deformation fields. Due to the finer discretization of the mechanical field these local errors are observed more in the mechanical deformation error, explaining the larger maximum and minimum values. This comparison suggests that higher errors are to be expected for the patterns based on the electro-deposited copper film or patterns with poor contrast in general. On the other hand, such a suboptimal pattern provides the possibility to measure at different scales. Note that the error in spatial distortion is higher at lower magnification, where the spatial distortion is larger.

3.7 Validation on real SEM images

Finally, the proposed methodology is used to assess the accuracy with which the artifacts can be measured in a series of real SEM images. In a real mechanical test, it is unfeasible to apply a higher-order mechanical deformation field which is known a priori with sufficiently high accuracy in order to validate the measurement accuracy. Therefore, instead, the experimental validation is performed by evaluating in detail the measured distortion (scan line shifts, spatial distortion, drift distortion) fields, as well as the improvement in the image residuals obtained by applying the artifact corrections. To this end, a simple rigid body motion, in which the mechanical deformation is known to be zero everywhere, is applied to the specimen, as done in the spatial distortion calibration phase. The calibration phase is performed, as described in Fig. 3.3b. Three magnifications are considered, corresponding to 10, 50 and 600 μm HFV as depicted in Figs. 3.14b, c and d. Two series of images are taken at each magnification, to assess the reproducibility.

In all correlations performed, the spatial distortion field is regularized by a 10×10 mesh of second order B-splines. Drift distortion is regularized by 10 knots of second order B-splines in time. An error function is assigned to each detected line shift (see Appendix 3.B), and zeroth order polynomials are used for the mechanics to capture the applied rigid body motion between each image pair.

Figs. 3.16a – d depict the measured spatial distortion fields determined from the two measurements at the lowest magnification ($600\mu m$ HFV). The two measurements (taken on the same day) match well. This reproducibility supports the assumption that the spatial distortion is time-independent, as long as the electron beam parameters are not changed. The difference of these two measurements is shown in Fig. 3.16e and f. The mean absolute value of these error fields amounts to 0.015 px in x and, 0.010 px in y

direction, showing high reproducibility of the spatial distortion measurements. Such low reproducibility error values alongside the low residual fields of the correlations (discussed below) indicate the high accuracy of the measurements. For more quantitative analysis, the diagonal of the spatial distortion fields in the x direction measured in all six tests at three magnifications are plotted on the same physical scale in Fig. 3.17. Note that because the mean of the spatial distortion fields is by definition zero, as explained in Section 3.3.2, all curves in Fig. 3.17 are vertically shifted to zero in the center. As expected, the spatial distortion is smaller for higher magnifications. The measurements at $50\mu m$ HFV slightly differ from the ones at $600\mu m$, which may be caused by the fact that the 50 and 10 μm HFV tests were done on a different day than the 600 μm HFV tests (different electron beam parameters). The spatial distortion at $10\mu m$ field of view is slightly below the noise level in the measurements, and thus may be neglected for measurements at this length scale. Nevertheless, at each magnification, the reproducibility of the spatial distortion is within the expected accuracy.

The obtained results for the drift distortion measurements are shown in Fig. 3.18, where Fig. 3.18a and b show the results in pixels while Fig. 3.18c and d depict the same results in micrometers. Each curve represents the evolution of drift in time for all eight images in a series. The gaps between segments in each curve represent the dead time between scanning of any two images. Note that although drift distortion is treated as a smooth function in time, also in between the scans, it is plotted only for the scanning duration of each image where actual measurement data exists. It is observed that the drift in pixels is much more pronounced at higher magnifications. The drift measured in the tests at $600\mu m$ HFV is as small as the accuracy of DIC, i.e. 0.01 px, which is why these noisy measurements are omitted in Fig. 3.18c and d. Note that Fig. 3.18c and d, show that the effect of drift distortion on a physical scale, i.e. expressed in μm, is independent of the magnification and comparable in rate and direction. This shows that in this particular case, drift distortion is dominated by a physical motion (e.g. due to a motion of the stage with respect to the column). This can be understood from the fact that all the four tests at 50 and $10\mu m$ field of view were performed in one session, in which the drift distortion apparently occurred mainly in y direction having a more or less similar rate.

The third type of considered artifact, i.e. line shifts, are the most pronounced and hardest to deal with for the images with $10\mu m$ field of view. In the second $10\mu m$ HFV test, the first image is interesting as it contains one line shift. LDIC is used between this first (reference) and the second image in the series, which also contains a scan line shift. Note that LDIC is only used for evaluating the impact of the line shift artifact corrections. For this case, where the mechanical displacement is constant in space (rigid body motion), it is possible to use LDIC as a reference, which means that any variation in the displacement field, found by LDIC, is due to the SEM artifacts. LDIC is performed with 53 px subset and 1 px step size, using VIC-2D™. As the amplitudes of the scan line shifts in x and y direction are comparable, Fig. 3.19a only shows the displacement field in x direction, obtained from LDIC on the second image in the second series of $10\mu m$ HFV, where two line shifts are visible, both exhibiting negative amplitudes. The

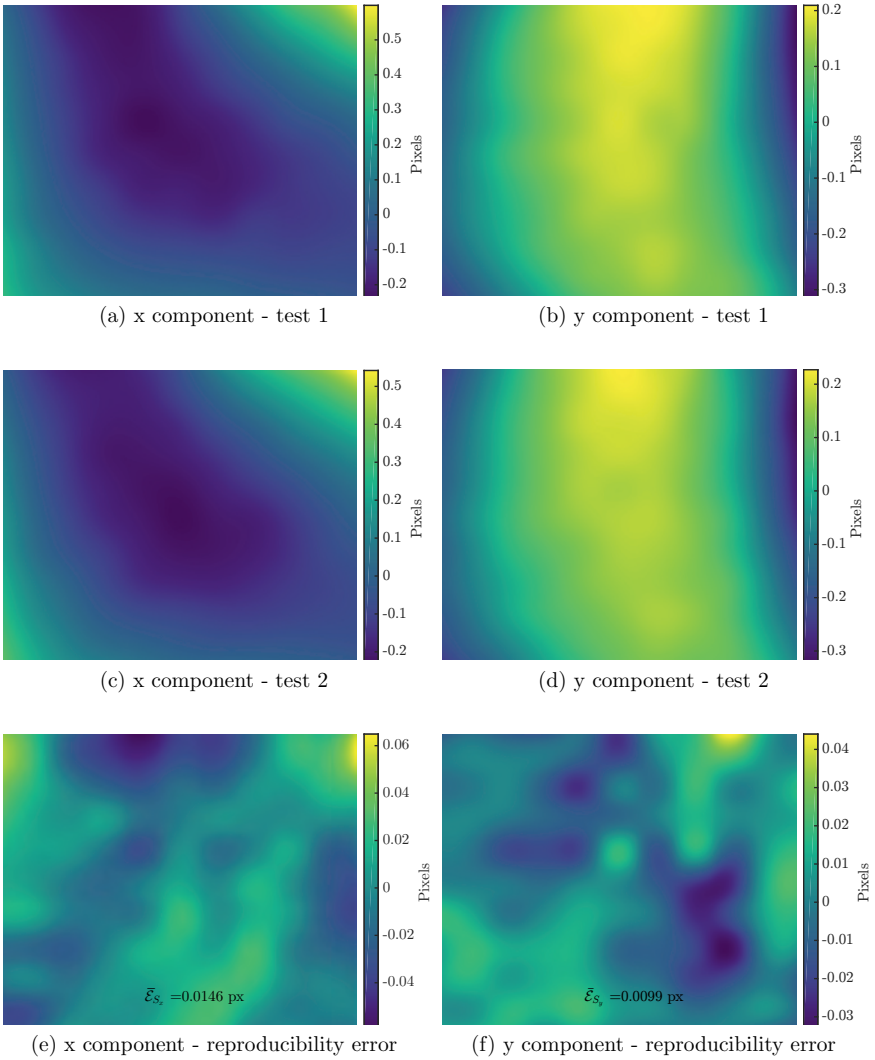

(a) x component - test 1

(b) y component - test 1

(c) x component - test 2

(d) y component - test 2

(e) x component - reproducibility error

(f) y component - reproducibility error

Figure 3.16: Spatial distortion field measured on 600μm field of view for measurement 1 in (a), (b), measurement 2 in (c), (d). The difference between the two measurements is shown in (e), (f)).

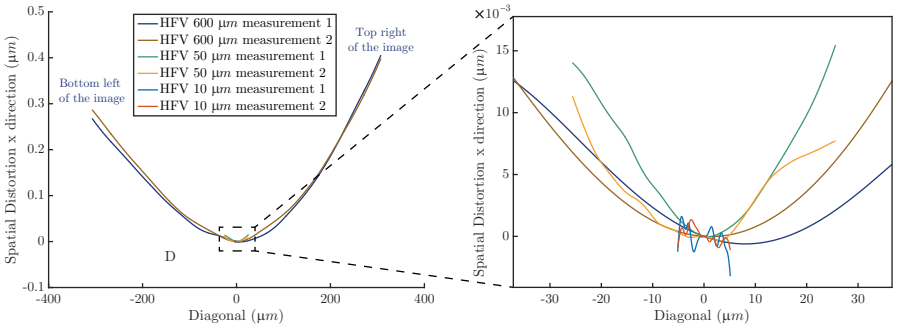

Figure 3.17: Comparison of spatial distortion measurements at different magnifications, where the x component is plotted as a function of the diagonal (bottom left to top right) of the images, while the bottom graph provides a zoom of the higher magnification measurements.

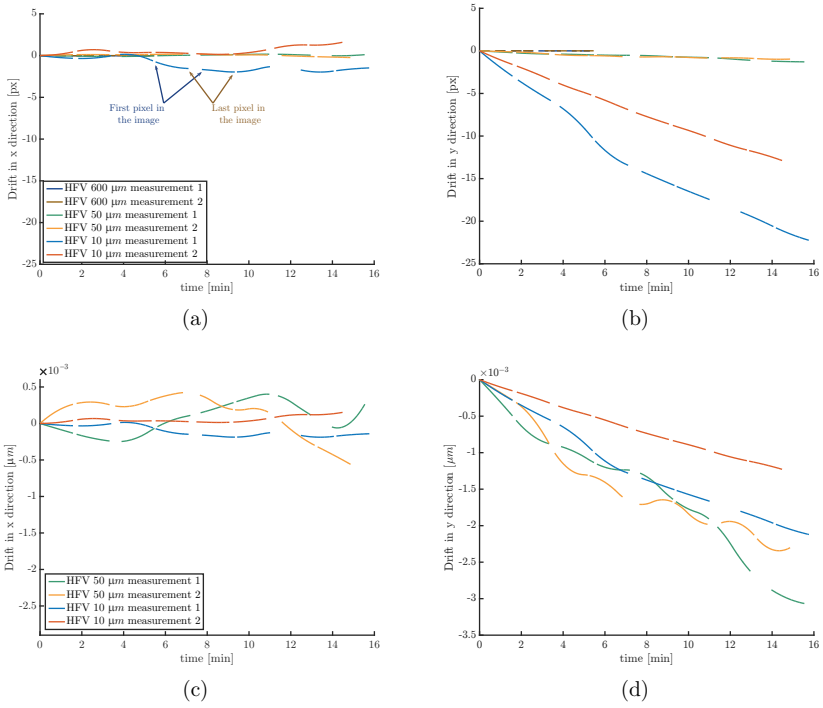

Figure 3.18: Evolution of drift as a function of time for each image series, plotted in (a), (b) pixels and (c), (d) micrometers. Drift distortion is a smooth function in time; however, it is plotted only for the duration of each image.

line shifts measured with the proposed artifact correction method are depicted for x direction in Fig. 3.19b, where the left and right sides show the line shift in Image 1 and 2. Note that the line shift in Image 1 has a positive amplitude while LDIC shows a negative amplitude since it cannot distinguish between the artifacts of the two images.

One of the images in the first $10\mu m$ HFV test contains multiple line shifts which is therefore also analyzed by comparison to LDIC. As the amplitudes of the scan line shifts in x and y direction are comparable, Fig. 3.19c only shows the displacement field in x direction from LDIC. Five line shifts are visible in this image, which is beyond the expected limitations of the proposed method [65]. Yet, all five line shifts are successfully identified, see Fig. 3.19d. The line shift amplitudes moreover match well with those from LDIC. However, the line shift locations reveal a minor deviation, which is caused by the other distortion fields displacing the line shifts. The LDIC results should, therefore, be compared with the proposed method including all artifact corrections. This is depicted on the right side of Fig. 3.19d, which restores the expected match with the line shift locations revealed by the LDIC results. Note the noisy results of LDIC (due to the suboptimal DIC pattern) in comparison with the low level of noise in the artifact measurement by the proposed method.

Fig. 3.20 finally compares the residual fields with and without artifact correction. Fig. 3.20a shows the residual field of one of the images with HFV $10\mu m$ from a conventional GDIC ignoring all artifacts, where the mechanical mapping function has been parametrized with zeroth order polynomials. Fig. 3.20b depicts the residual field of the same image from the correlation including the artifact corrections. The difference between the two emphasizes the quality of the measurement of the artifacts and the correction for them. Such an accurate measurement of the different artifact fields is a necessary condition for eliminating the artifact-induced errors in the mechanical deformation measurements from *in-situ* SEM tests. Fig. 3.20c and d show the same comparison for the $50\mu m$ field of view, where a zoomed view is included for clarity. Similar results are also obtained for the lowest magnification tests.

3.8 Conclusions

Using high resolution scanning electron microscopy images should enable high displacement resolutions in DIC. However, SEM images contain artifacts which introduce considerable errors in displacement measurements if ignored. SEM artifacts are categorized in three types: spatial distortion, drift distortion and scan line shifts.

The current study proposes a generic unified framework based on IDIC to measure all three types of artifact fields alongside the mechanical deformations, in an integrated manner, to minimize the artifact induced errors in the displacement measurements. To this purpose, the imaging process of SEM is captured through the hierarchical mapping functions that have been inserted in the proposed IDIC framework. Based on these hierarchical mapping functions, the IDIC problem is reformulated. Using the proposed IDIC framework and following the proper imaging and correlation procedures,

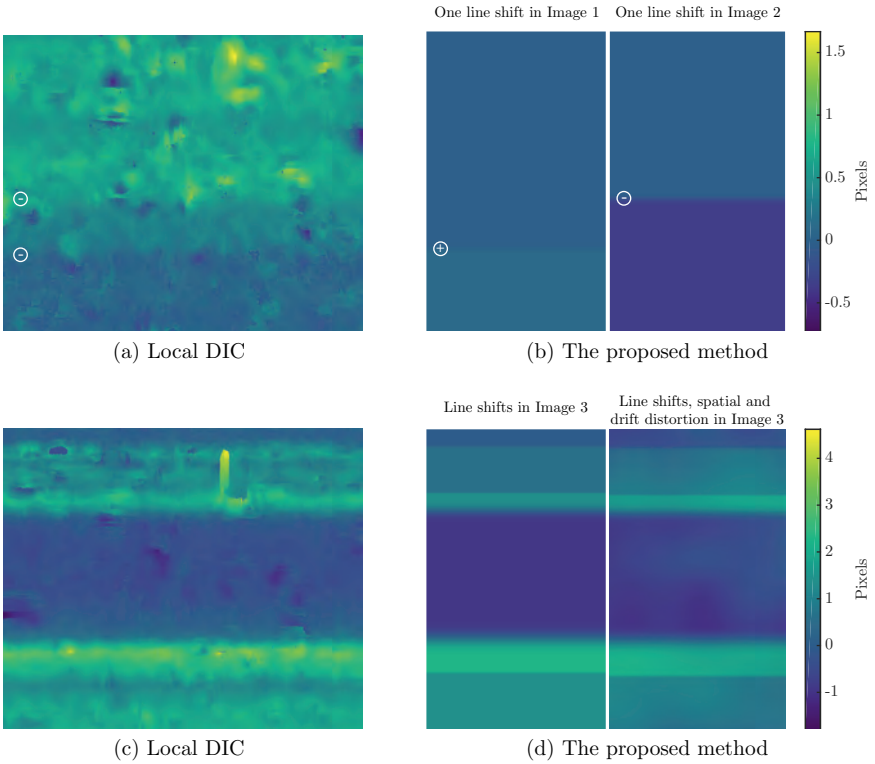

(a) Local DIC (b) The proposed method

(c) Local DIC (d) The proposed method

Figure 3.19: Measurement of line shift artifacts and comparison with local DIC results. (a) Displacement in x direction of LDIC on the second image of test 2 with $10\mu m$ field of view compared to (b) line shift artifacts measured with the proposed method in image 1 (left) and 2 (right). (c) Displacement in x direction of LDIC on the third image of test 1 with $10\mu m$ field of view compared to (d) line shift artifacts (left) and the total artifact field (right) measured with the proposed method in the same image. In all the cases here the amplitudes of the scan line shifts in y direction are comparable to the amplitudes in x direction.

the artifact fields can be measured separately from the mechanical displacement fields in a simple optimization step. This separation is made possible through the physical characteristics of the individual fields:

(i) spatial distortion is inherently a constant field in time; it is identified during an independent calibration step in which no mechanical deformation occurs (only discrete steps of rigid body motion are applied);

(ii) drift is a continuously evolving, smooth function in time, also during scanning of each image; its image distortion is distinguished from mechanical deformation which is applied in a step-wise manner between the acquisition of every two images, making it constant in each image pair;

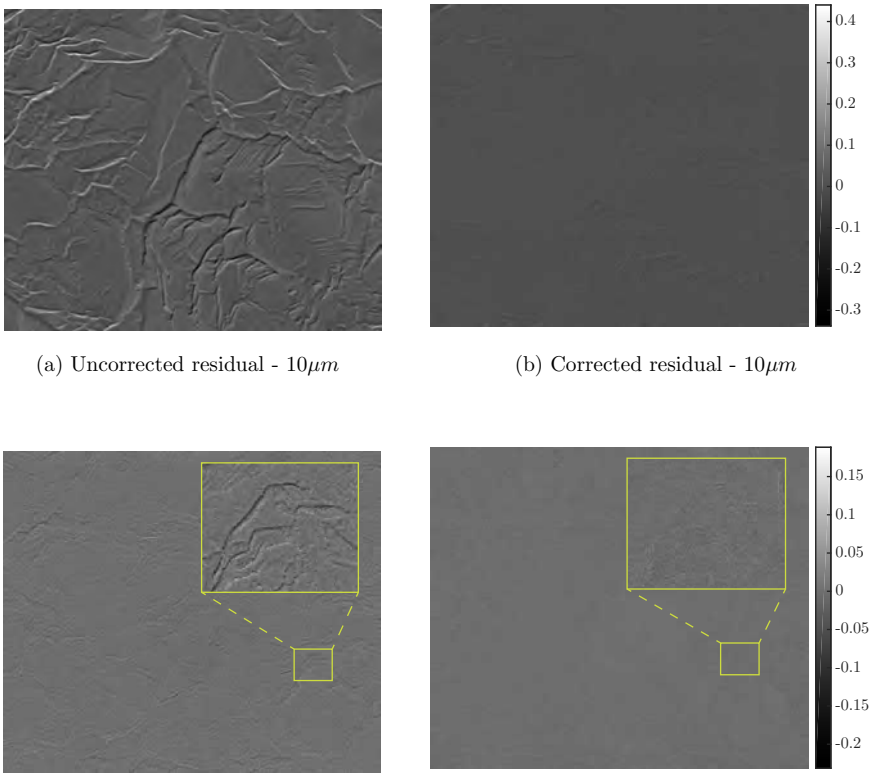

(a) Uncorrected residual - $10\mu m$

(b) Corrected residual - $10\mu m$

(c) Uncorrected residual - $50\mu m$

(d) Corrected residual - $50\mu m$

Figure 3.20: Examples of residual fields of images with $10\mu m$ horizontal field of view (a) without and (b) with artifact correction, and of images with $50\mu m$ horizontal field of view (c) without and (d) with artifact correction (zoomed view included for clarity).

(iii) scan line shift artifact fields are random localized distortions with a direction dictated by the underlying scanning process; they occur discretely in time, and are distinguished from the mechanical deformation through image pairs, similar to drift;

(iv) mechanical deformation is considered as an arbitrary complementary field, constant within a given loading step (i.e. constant for each image pair); hence no constraint is enforced on mechanical deformation.

This methodology has been validated with a series of virtual experiments. First, artificially generated images have been deformed both by an evolving mechanical deformation field and by SEM imaging artifact fields. The mechanics and the artifacts of each of these sets of images have been then measured using the framework introduced in this article. First, a less complex case of mechanical deformation and spatial distortion

has been studied in a virtual experiment, and analyses on noise levels and the regularization of the artifact fields have been conducted. It has been shown that the error in the mechanical displacement measurement remains acceptable up to a noise level of 5% of the image dynamic range. Different regularizations of spatial distortion with global basis functions and drift distortion with both globally and locally supported basis functions, resulted in acceptable error levels (< 0.02 px) in the mechanical displacement measurements, confirming the robustness of the framework in convergence.

Second, a more complex virtual experiment has been carried out by deforming another set of virtually generated images reflecting a challenging localized mechanical deformation and asymmetric spatial distortion field (taken from SEM-DIC measurements in the literature). The artifact and deformation fields have been measured using the current method, which resulted in errors well within the DIC accuracy range.

Third, the same challenging virtual experiments have been repeated using real SEM patterns to study the performance of the proposed methodology under realistic conditions. A regular SEM-DIC pattern provides the same accuracy as a virtual pattern. A sub-optimal multiscale pattern (based on an electro-deposited copper film) reveals somewhat higher errors in the evaluation of the mechanical and distortion fields.

And finally, the proposed method has been validated on different sets of real SEM images at three different magnifications, based on the sub-optimal multiscale pattern, to assess the accuracy with which the artifacts can be measured. The reproducibility of the results of spatial distortion and drift distortion, the overlap with measurements at different magnifications, and low image residuals show the accuracy of the measurements. The comparison of the line shift artifact measurements with LDIC results reveals the accuracy of the line shift artifact measurements even when five line shifts occur in one image, which is beyond the expected limitation of the proposed method. Finally, the significant improvement of the residual fields by including the artifact corrections confirms the high accuracy of the artifact corrections performed using the current method.

The proposed method is unique in the following:

(i) it deals with all three types of SEM artifacts (line shits, drift and spatial distortion) in a unified and systematic way,

(ii) the SEM imaging process is taken into account through a set of hierarchical mapping functions (the general framework can be easily extended to any imaging system),

(iii) all artifact and mechanical deformation fields are captured properly in only two correlation steps (spatial distortion calibration and mechanical test phase),

(iv) the acquired data (SEM images) are used most efficiently by avoiding any integration of images,

(v) the drift distortion is measured/corrected directly for all the duration of the test including the reference image, without any extrapolation of data.

Appendices

3.A Alternative image gradient arrangement

It can be easily shown that by rearranging the image gradient, as found in Ref. [61] for the case of conventional GDIC, Eqs. (3.21) to (3.23) can be rewritten as:

$$L_k^{L_i}(\mathbf{X}, \underline{\mathbb{0}}) = [\boldsymbol{\nabla}_{\mathbf{X}} \tilde{g}_i(\mathbf{X})] \cdot [\boldsymbol{\nabla}_{\mathbf{X}} (\boldsymbol{\phi}_{L_i} \circ \boldsymbol{\phi}_S \circ \boldsymbol{\phi}_{M_i}(\mathbf{X}))]^{-1} \left(\frac{\partial \boldsymbol{\phi}_{L_i}(\mathbf{X}, \underline{\mathbb{0}})}{\partial a_k} \circ \boldsymbol{\phi}_S \circ \boldsymbol{\phi}_{M_i}(\mathbf{X}, \underline{\mathbb{0}}) \right) \tag{3.42}$$

$$L_k^{S_i}(\mathbf{X}, \underline{\mathbb{0}}) = [\boldsymbol{\nabla}_{\mathbf{X}} \tilde{g}_i(\mathbf{X})] \cdot [\boldsymbol{\nabla}_{\mathbf{X}} (\boldsymbol{\phi}_S \circ \boldsymbol{\phi}_{M_i}(\mathbf{X}))]^{-1} \left(\frac{\partial \boldsymbol{\phi}_S(\mathbf{X}, \underline{\mathbb{0}})}{\partial a_k} \circ \boldsymbol{\phi}_{M_i}(\mathbf{X}, \underline{\mathbb{0}}) \right) \tag{3.43}$$

$$L_k^{M_i}(\mathbf{X}, \underline{\mathbb{0}}) = [\boldsymbol{\nabla}_{\mathbf{X}} \tilde{g}_i(\mathbf{X})] \cdot [\boldsymbol{\nabla}_{\mathbf{X}} (\boldsymbol{\phi}_{M_i}(\mathbf{X}))]^{-1} \left(\frac{\partial \boldsymbol{\phi}_{M_i}(\mathbf{X}, \underline{\mathbb{0}})}{\partial a_k} \right). \tag{3.44}$$

This arrangement is more convenient for implementation, mainly because there is no need for interpolation in the image gradient calculation.

3.B Initial guess for correlations

In order to establish convergence of the correlations, a systematic procedure is adopted. It is proposed to follow these few steps of correlations by gradually adding some of the dofs and removing blurring from images. Each step improves the initial guess for the next one, so that starting with the most trivial initial guess (zero), the correlations converge robustly and monotonically.

The randomly occurring line shifts need to be detected and an adequate initial guess of their positions is needed. Following [65], a pre-correlation step is performed in which the approximate location of the line shifts is identified. This is done by performing a conventional GDIC analysis between image pairs, ignoring the existence of any line shifts and using merely first order polynomials for basis functions. This pre-correlation is the most simple GDIC correlation. The residual fields of the pre-correlations reflect the line shifts. Plotting the row mean of the residual fields as a function of the row number of the images reveals existing line shifts, which gives a good initial guess for their positions, cf. Fig. 3.21. Comparing these positions for three correlations among three images indicates which line shift belongs to which image. Fig. 3.21 depicts an example of 6 pre-correlations, of a set of six SEM images of the calibration phase of the virtual experiment. Fig. 3.21a shows the pre-correlations between images 1, 2 and 3. There is a high gradient in the curves related to the pre-correlations involving image one at approximately $y = -50$ px reflecting a line shift artifact in image 1 and in this

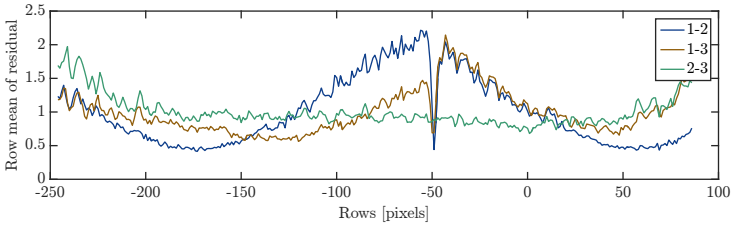

(a)

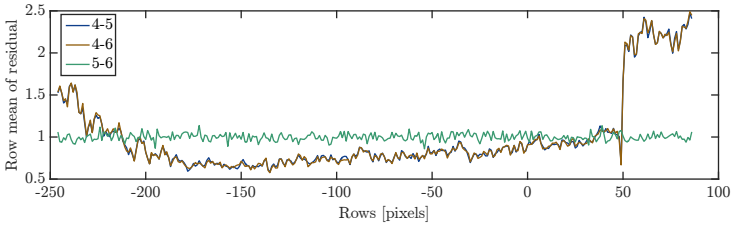

(b)

Figure 3.21: Row mean of the residuals of pre-correlations as a function of the row number for the virtual images of the calibration phase. Triplets of (a) 1, 2 and 3 revealing a line shift in image 1, approximately at $y = -50$ px and (b) 4, 5 and 6 revealing a line shift in image 4, approximately at $y = 50$ px. Note that the residual fields are available only in the region of interest.

position. Likewise, Fig. 3.21b reveals a line shift at approximately $y = 50$ px in image four. It is also helpful to use smoothed derivatives of these curves in which dominant peaks indicate line shifts in the images. By this means the procedure is even automated. Note that in cases in which recognition of line shifts becomes more difficult, e.g. due to a local lack of DIC pattern or the presence of several line shifts close to one another, LDIC can provide a useful indicator. The width of each line shift is initially constrained to a large value, e.g. 20 px, to first correlate the position as well as the line shift amplitudes along with all the other deformation and distortion fields, after which a final correlation step including also the dofs for the line shift width is performed. Once proper initial guesses for line shift artifact positions are attained, the very first correlation step is performed on images that are blurred by a Gaussian filter with standard deviation of 10 px and a window size of 41 px. After obtaining proper initial guesses for the displacement and artifact fields, the second correlation step is performed on the original images (not blurred). In the first two correlation steps, the dofs characterizing the width of the line shifts are deactivated, as mentioned above. The next step is basically a repetition of the previous step including the dofs of the width of all the line shifts. Up to this point the reference image is chosen to be the first back-deformed image ($\tilde{g}_1$), as in Eq. (3.12). The final (principal) step is correlating the original (not blurred) images with all the dofs of mechanics and artifacts, and the reference image defined as the average of all back-deformed images, as in Eq. (3.29). Since the correlation with the general definition

of the reference image typically requires more iterations, the extended definition for the reference image is introduced only when the solution is almost approached. This optimizes the total number of iterations. The steps to be taken can be summarized as:

- perform pre-correlation on image pairs with first order polynomials,
- plot the row mean of the residual field of each three pre-correlations and obtain the initial guess for the position of line shifts,
- perform a correlation step on blurred images to obtain a good initial guess for all dofs,
- perform the second correlation step on the original (not blurred) images,
- repeat the final step with the reference image defined as the average of all back-deformed images.

Chapter 4

Experimental full-scale analysis of size effects in cellular elastomeric metamaterials

Reproduced from:
S. Maraghechi, J. P. M. Hoefnagels, R. H. J. Peerlings, O. Rokoš, M. G. D. Geers
Experimental full-scale analysis of size effects in cellular elastomeric metamaterials, 2019, *Submitted*.

Abstract

Cellular elastomeric metamaterials may exhibit multiple microstructural pattern transformations beyond the point of buckling, each with a characteristic mechanical response. This makes them interesting for various applications, for instance in soft robotics. Numerical studies in the literature revealed significant size effects in the mechanical response such materials due to large boundary layer formations. The goal of this paper is to analyse these findings experimentally on small scale specimens that are relevant for real applications. Cellular metamaterial specimens are manufactured with different scale ratios, i.e. ratio of specimen size to unit cell size, while *in-situ* micro-compression tests combined with digital image correlation are applied to enable full field kinematic measurements. In order to objectively compare the results, complementary numerical simulations are performed. The global behaviour of the specimens in the experiments aligns well with the numerical predictions, in terms of the pre-buckling stiffness, the buckling strain and the post buckling stress. the local behaviour of the specimens, i.e. pattern transformation and formation of boundary layers, is consistent between experiments and numerical simulations. Comparison of the results of the current study with idealized numerical studies available in the literature, reveals the influence of the conditions in real applications of cellular metamaterials, e.g. lateral confinement, on their mechanical response such as the size and formation of boundary layers.

4.1 Introduction

Cellular soft materials have proven to be useful in a variety of applications, and thus have attracted many studies in the past decade [74]. The behaviour of such materials significantly depends on their microstructural geometry, where buckling of the microstructure entails a non-local effective behaviour, with one or multiple emerging patterns, e.g. the pattern shown in Fig. 4.1b. Since these materials typically reveal a distinctly different mechanical behaviour beyond their buckling point compared to before, e.g. a transition from non-auxetic to auxetic behaviour [30], they are commonly categorized as metamaterials.

Different applications such as strain tunable photonic crystals [42] or soft robotics [40, 41] have been investigated in the literature. Other examples include programmable mechanical metamaterials [43], for which the axial compressive behaviour is adjustable by lateral confinement, and functionally graded metamaterials, hereby enabling enhanced global stability and dynamic compression resistance [75]. [76] used 3D printing techniques to manufacture and study multi-material mechanical metamaterials. The design of cellular metamaterials is not limited to planar structures and interesting studies have been conducted on 3D cellular structures [36, 39]. Yet the literature mainly focused on planar cellular elastomeric metamaterials. For instance, the effect of hole geometry and stacking on the behaviour of cellular elastomers was studied in detail in [29, 31–33]. [77] analysed different patterns induced by swelling in cellular hydrogel membranes. [78] investigated the effect of friction on buckling pattern formation in cellular structures.

In cellular elastomeric metamaterials, the pattern transformation is strongly affected by the boundary conditions that may locally confine these patterns. Kinematic restrictions lead to the formation of boundary layers resulting in a significant dependence of the effective mechanical response on the ratio of the specimen size to hole size, i.e. the so-called "size effect". In a recent study, Ameen et al. [44] numerically investigated the size effect in cellular elastomers. They showed a considerable influence of size on the global behaviour of such materials and a characteristic boundary layer size in specimens with scale ratios of 4 to 128, where scale ratio is the ratio of the specimen length to the length of a unit cell of the microstructure. They reported an increasing trend in the boundary layer thickness with a an asymptote of approximately three unit cells and an asymptotic trend of global stress with more than 40% decrease over the range of scale ratios.

The goal of the current study is to assess these findings experimentally for microstructures of a realistic size. In order to be more relevant to engineering purposes, experimental studies are therefore conducted on small scale specimens. To this end, different specimens with millimetre sized holes and various number of unit cells in loading direction were processed using custom-made moulds. *In-situ* micro compression tests with optical microscopy in combination with Digital Image Correlation (DIC) are employed to measure high resolution full-field displacement maps of the specimens with different scale ratios. Such a detailed kinematic assessment is essential in identifying the

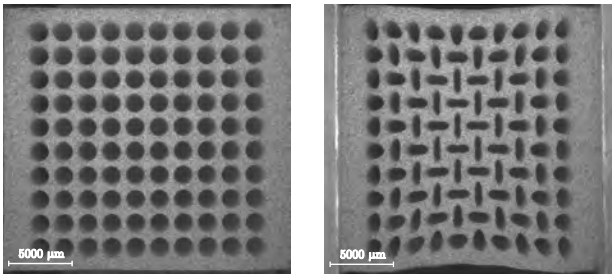

(a) Undeformed microstructure (b) Deformed microstructure

Figure 4.1: A cellular elastomeric metamaterial (a) before, and (b) after the onset of buckling in the microstructure due to compression in horizontal direction, leading to the emergence of an anti-symmetric pattern.

local boundary layers, and to enable accurate validation of the size effects in the global behaviour of such metamaterials.

There are two major differences between the current experimental study and the numerical investigation of Ameen et al. [44]. The numerical specimens were infinite in the transverse direction due to the use of periodic boundary conditions, whereby the boundary layer analysis was done on a homogenized solution obtained by ensemble averaging of many realizations of the microstructure inside the specimen. These conditions are not feasible experimentally. Thus new Finite Element (FE) simulations, replicating the experiments, are conducted to objectively compare the experimental findings. To this end, bulk material parameters are identified by fitting a hyper-elastic Ogden model to tensile tests done on the bulk sample of the base material. A good match is observed between the experimental and numerical results in both global and local behaviour of the cellular elastomeric metamaterial specimens. The trend in the global stress is of the same order of magnitude of the one reported by [44]. It is shown that the size and emergence of boundary layers strongly depend on the lateral confinement of the metamaterial, which has direct consequences for their optimal design. These findings indicate the influence of the boundary conditions relevant to real applications of cellular elastomeric metamaterials on their mechanical response beyond the pattern transformation, which was not addressed in idealized numerical studies in the literature.

4.2 Methodology

4.2.1 Specimen preparation

Thick cellular elastomeric metamaterial specimens with millimetric circular holes have been processed with customised moulds with a rectangular stacking and micrometric spacings. It is important to make thick specimens, and small spacings with respect

to the hole diameter to induce local buckling, rather than global buckling, during the *in-situ* micro-compression tests. Note that no out-of-plane constraints can be applied to the surface of the specimens due to the DIC speckle pattern applied on the specimen surface. All specimens have 1.5 mm hole diameter, 1.9 mm center to centre spacing and are 22.5 mm thick, cf. Fig. 4.2a. Bulk edges of 1.9 mm and 0.9 mm are present in the axial and transverse directions, respectively. The size of each unit cell is denoted l, whereas the length of the specimen (excluding the bulk edges) is denoted L, see Fig. 4.2a. The scale ratio of each specimen, L/l, is equal to the number of holes in the loading direction. Specimens with scale ratios of 4, 6, 8, 10 and 12, all with 10 holes in the transverse direction, have been manufactured. Two specimens for the scale ratios 8, 10 and 12, and a single specimen for the scale ratios 4 and 6 were made. Based on the study of Ameen et al. [44], the scale ratio of 12 should be sufficient to allow for a completely developed boundary layer. Aluminium cubic moulds with perforated bottom surface, removable steel pins, and perforated brass cover plates are utilized, cf. Fig. 4.2b. Sylgard 184 with 1:10 mixing ratio was degassed for 30 minutes, then slowly poured into the moulds with inserted pins and degassed for 2 hours. Finally, the perforated cover plates are placed to close the mould from the top and the specimens are cured for 15 hours at 70℃. Degassing of the filled moulds should be very slow due to the small area between the pins and the high surface tension of the PDMS mixture. Thus the bulk material edges are included in the specimen design to provide an outlet for the air bubbles and achieve complete degassing before the mixture viscosity increases too much during the curing process. Note that the long curing time at an elevated temperature is necessary for thick specimens to ensure proper and homogeneous curing. Each specimen is finalized by removing all pins, and then the cover plate.

A speckle pattern was applied on the specimens to generate a contrast as required for DIC. Since Sylgard 184 is translucent and light reflecting, the speckle pattern consists of two layers; first a white powder (HELLING Standard-Check developer Medium Nr. 3) was sprayed to make a fine-grained background, then black India ink was sprayed using an air brush. Spraying at an inclined angle through a short tube, to create a spiral flow, filters out the big particles, resulting in speckles measuring roughly 30 to 80 μm, corresponding to 3 to 8 pixels as shown in Fig. 4.2c.

4.2.2 *In-situ* micro-compression tests

Micro-compression tests are conducted on the patterned specimens using a Kammrath & Weiss micro tensile/compression stage with a 50 N load cell. Two aluminium T-shaped clamps are used to apply the compression uniformly in the axial direction, cf. Fig. 4.2d. A Zeiss Discovery.V20 stereo microscope with a PlanApo S 0.63× objective and an Axiocam 506 mono camera with 2751×2207 pixels resolution are used to acquire images during the tests. A 7.6× magnification is used to cover the whole area of the largest specimen. The test is interrupted to record images at displacements corresponding to 1.4% global strain increments up to 7% strain, followed by 0.2% global strain increments up to 12% strain for all specimens. The global strain for defining the load increments is

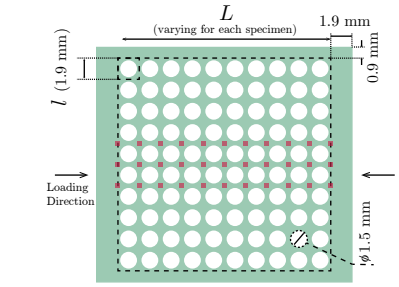

(a) Specimen design

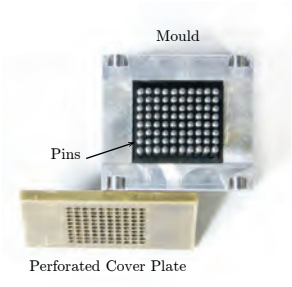

(b) Mould

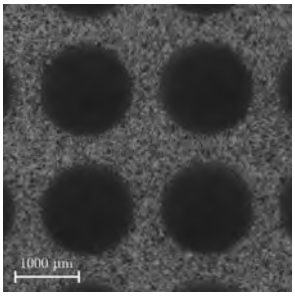

(c) Speckle Pattern

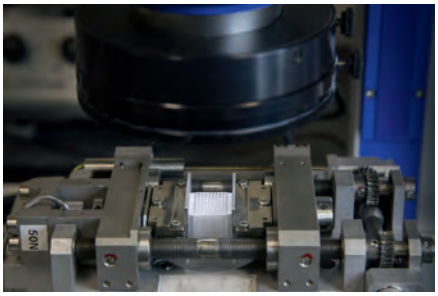

(d) Test setup

Figure 4.2: Experimental set-up for *in-situ* testing. (a) Schematic of a 10×10 holes specimen (scale ratio of 10) indicating the total length of the specimen excluding the bulk side edges (L: the large dashed square), the size of the unit cells ($l = 1.9\ mm$: small dashed square), the diameter of the holes ($1.5\ mm$), the size of the bulk edges and the loading direction. The red squares of 20×20 pixels depict the position where the local rotation of the islands (cross-shaped parts in the center of each four holes) are probed for quantifying the boundary layer size. (b) The aluminium mould, with inserted pins, used for making the 10×8 holes specimens, along with the brass perforated cover plate. (c) Zoomed view of the speckle pattern applied on the specimens for DIC. (d) Test setup showing the micro compression stage, with 50 N load cell, underneath the microscope's objective with LED ring light mounted.

calculated as the displacement readings of the Linear variable differential transformer (LVDT) of the compression stage, divided by the initial length of each specimen. The test on each specimen is repeated four times. During the first and last test, images are acquired at $8.8 \times 10^{-5} s^{-1}$ global strain rate. The other two tests are uninterrupted and performed at $3.3 \times 10^{-4} s^{-1}$ global strain rate. Unloading during all tests is done with $3.3 \times 10^{-4} s^{-1}$ global strain rate.

4.2.3 Full-field displacement measurement

The images taken during the *in-situ* tests are used for local DIC to extract the kinematic fields. Images are typically affected by optical distortions of the objective lens.

These spatial distortions are measured using the method proposed by [65, 79]. The measured distortion field is used to correct the images taken during the *in-situ* tests, which is necessary because the magnitude of the distortions is roughly 10% of the actual displacements in the metamaterial specimens. The kinematic fields are then determined using the VIC-2D local DIC package with 19 pixel subset and 1 pixel step size. The displacement fields are used to evaluate local rotation fields using the module available in VIC-2D and a smoothing filter size of 51 pixels.

4.2.4 Numerical Methodology

A plane strain finite element model, using quadratic isoparametric triangular elements with three-point Gauss integration rule, is made for each specimen size. Dirichlet boundary conditions are applied on the two vertical edges perpendicular to the loading direction, whereas the two remaining edges are free. PDMS is modelled with a hyper-elastic Ogden material model. Considering the range of different material properties reported in the literature [80–83], tensile tests are performed to characterize the bulk mechanical properties of the PDMS used. The Ogden model material parameters are identified from these tensile tests: $c_1 = 0.0892\ MPa$, $c_2 = 1.2537\ MPa$, $m_1 = 10.0959$, $m_2 = 0.0036$ and $\kappa = 29.6716\ MPa$, where c_k and m_k are the material parameters and κ is the bulk modulus. More details on the material characterization are given in 4.A. Buckling of the numerical model is guaranteed by checking the signs of the diagonal matrix D in the $\mathrm{LDL}^{\mathrm{T}}$ decomposition of the iterative finite element stiffness matrix, cf. e.g. [Section 7.1.2 84]. When a negative entry is encountered, the eigenvector corresponding to the lowest eigenvalue is computed and used as a perturbation of the Newton solver. The magnitude of the perturbation is increased from initially a very small value until a stable configuration is reached. The algorithm then proceeds with a buckled stable configuration if the perturbation was successful, otherwise the load increment is halved and the entire procedure repeats.

4.3 Results and Discussion

Local rotation fields are obtained from displacement fields obtained by local DIC, as described in Section 4.2.3, and are shown in Fig. 4.3 in the deformed configuration for one specimen of each scale ratio at 1.3% global strain after buckling.

4.3.1 Global Response

In order to accurately measure the applied displacement on the specimens, and thus the nominal strains, the DIC data are used. In order to properly quantify the displacement to achieve the same global strain for specimens of different scale ratios, the exact geometry of the specimens has to be accounted for. To this end, the global displacement is determined at the outside of the first and the last unit cells (i.e. excluding the bulk edges), where the applied displacement on each side is averaged over the width of the

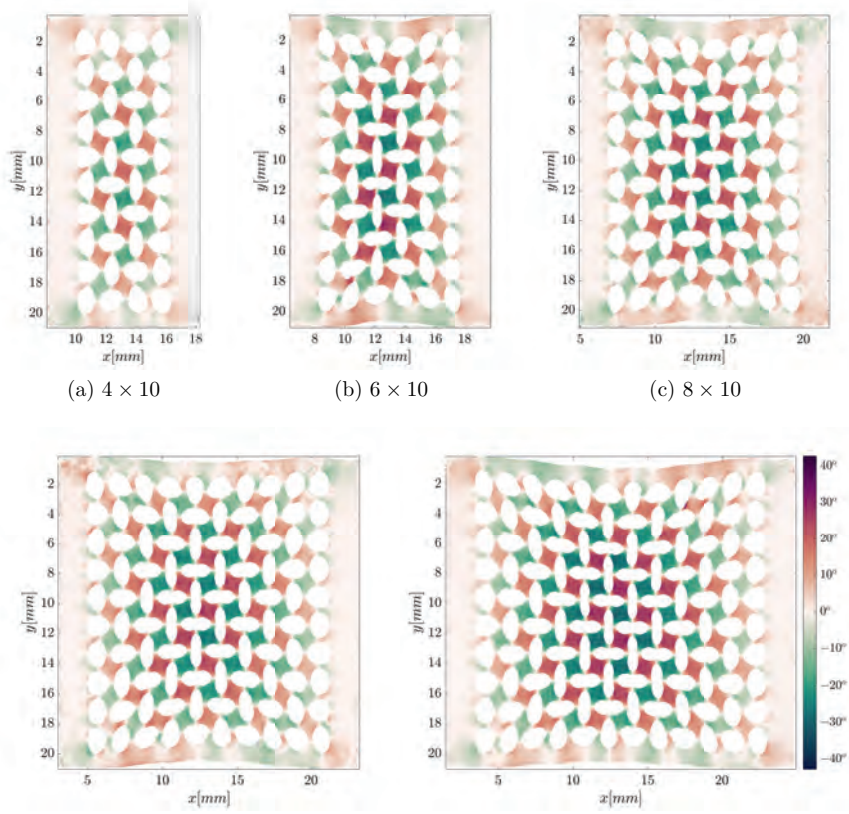

(a) 4×10 (b) 6×10 (c) 8×10

(d) 10×10 (e) 12×10

Figure 4.3: Local rotation fields inside a specimen for each scale ratio, at 13% global strain after local buckling, plotted on the deformed configuration. The displacement fields used for calculating the deformations and the local rotations are obtained by local digital image correlation.

specimen. The global nominal strain is then calculated as the ratio of the relative displacement between the two sides and the initial distance, L. The global nominal stress is computed as the ratio of the global compressive force and the initial cross sectional area of each specimen. This approach is used for both experimental and numerical analyses.

Fig. 4.4a depicts the global stress-strain curves of different specimens for both the experiments and the numerical simulations. The results of all tests for each scale ratio are depicted in the same color for the sake of readability. Optical inspection of the specimens under the microscope showed variations of approximately 3 % in hole diameter. Therefore extra simulations were conducted considering ± 3 % variation in the diameter of the holes. The error bars at three different strain levels in Fig. 4.4a depict the range of stresses observed in these simulations. Note that the somewhat higher stiffness

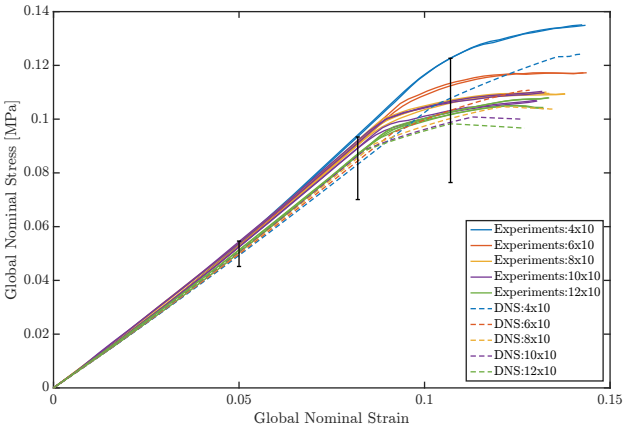

(a) Stress–strain curves

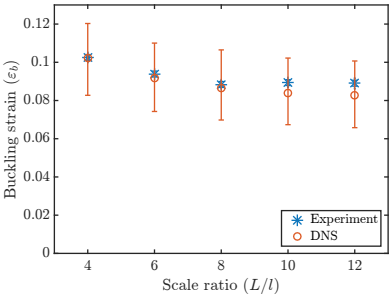

(b) Buckling strain

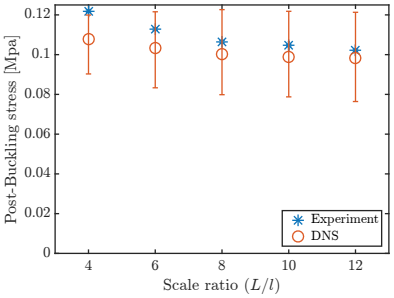

(c) Post-Buckling stress

Figure 4.4: Global response of specimens of different scale ratios, comparing experimental and numerical results. (a) Global nominal stress–strain curve. Results of all tests for each scale ratio are depicted in the same color. (b) Buckling strains, calculated as the strain at which the maximum curvature occurs in the stress–strain curves. (c) Post-buckling stresses determined at a global strain of 10.7% (maximum strain before global buckling of the largest specimen). The error bars on the experimental data in (b) and (c) reflect the variability in all tests done, while the error bars on all numerical data reflect the uncertainties in the simulations, resulting from the geometrical variations . The small blue dots in (b) and (c) represent the results of each individual test, while the blue stars the average for each scale ratio.

observed in the experiments is in line with the optical inspection of the specimens pointing to smaller holes than the design value. The pre-buckling stiffness values of different specimens agree well, as expected for cellular metamaterials, for which the pre-buckling stiffness should be independent of the scale ratio. There is, however, a small systematic variation in the initial stiffness due to the bulk edges on the transverse sides, which was confirmed in numerical simulations with and without these side bulk edges.

Fig. 4.4b shows the global strain at which the local buckling, resulting in the pattern transformation, occurs in each specimen, which is denoted by ε_b. The average buckling strain for all tested specimens of a certain scale ratio are depicted in this curve, and the error bars are attained as follows. The differences between the buckling strains for all 16 tests and the average of the corresponding scale ratio are calculated. The standard deviation of these disparities gives a global measure of the uncertainty in the buckling strain measurements, and is therefore used as the error bar. Based on the observed geometrical variations, the error bars on the numerical results are based on two sets of simulations considering ± 3 % variation of the hole diameters. The buckling strains match well between the experimental and numerical results (Fig. 4.4b). Note that a small variation in the geometry of the specimens results in a large shift in buckling strains. The asymptotically decreasing trend, however, remains uninfluenced.

Fig. 4.4c depicts the post-buckling stress against the scale ratio, taken from both the experimental and numerical results. The stress is determined at 10.7% global strain, which is the maximum strain prior to global buckling in the largest specimen. The error bars are obtained as in Fig. 4.4b. A nearly constant trend is observed in the upper bound of the error bars due to the fact that the simulation of the two smallest specimens with a 3% smaller hole diameter did not yet reveal local buckling at the imposed 10.7% global strain. Taking this into account, the numerical and experimental results show a similar asymptotically decreasing trend. The larger size effect in the experiments is due to the fact that the onset of global buckling in the larger specimens is more gradual, influencing the stresses at the considered strain.

The global post buckling stress in the current study shows a 19% decrease from scale ratio 4 to 12. This value is 29% in the idealized numerical study of [44]. The difference is due to the relative size of the holes with respect to the unit cell as well as different boundary conditions i.e. no free boundaries nor bulk edges in the infinitely wide specimens considered in simulations of [44].

4.3.2 Local Behaviour

The boundary conditions applied to the cellular elastomeric metamaterial specimens obviously influence the buckling-induced pattern close to the edges, which in turn result in the size effects discussed above. Ameen et al. [44] studied this effect by numerically identifying the boundary layer in which the normal strain in the loading direction is affected by the edge, using a homogenized solution. This homogenized solution was calculated from an ensemble average of many realizations of the same periodic microstructure, where the microstructure was shifted relative to the specimen geometry.

Since it is impossible to use the same procedure for experimental results (for which only one realization is measured), a different approach for characterising the boundary layer thickness is proposed here. The local buckling of the ligaments between the holes results in rotation of the islands, leading to the patterns shown in Fig. 4.3. When the specimen is loaded beyond the buckling point, a significant increase in the rotation of the islands results in a pronounced pattern. This also applies to the spatial variation of the pattern at each global strain state, i.e. the rotation of the islands is larger in the specimen center, where the pattern is more developed.

Therefore, in order to quantify the size of the boundary layer, the rotation of the islands is exploited as the quantity of interest. To avoid the influence of the free side edges, only the two central unit cell rows are taken into consideration, see Fig. 4.2a. A unique rotation angle is determined for each island by averaging the local rotations in a window of 20×20 pixels in the center of each island. The little red squares in Fig. 4.2a indicate the positions where the local rotations are probed. The absolute values of the rotation angles of the islands are averaged over each column (i.e. in the transverse direction) and plotted against the row number (i.e. normalized axial coordinate) in Fig. 4.5a for the experimental and Fig. 4.5b for the numerical data. Each curve is evaluated at a relative global strain increment of 0.013 after the onset of local buckling at the corresponding scale ratio ($\varepsilon_b + 0.013$). The curves in Fig. 4.5a and b are plotted by mirroring the rotation angles with respect to the central island and averaging the values on both sides. By this means the small variations in the rotation angles, due to the antisymmetry of the buckling pattern, are averaged out and smooth symmetric curves are attained. Values corresponding to non-integer number of holes/scale ratios are based on linear interpolation of the local rotation of islands to give a quasi-continuous measure for quantifying the boundary layer thickness. Each curve in Figs. 4.5a and 4.5b is probed at 70% of its dynamic range and the x coordinate of each intersection defines the size of the boundary layer. This threshold is chosen to ensure that the results of the current study, in case of infinitely wide specimens, match those of [44] for large scale ratios. The resulting boundary layer size is plotted against the scale ratio in Fig. 4.5c. The experimental and numerical results match adequately, although the trend is not yet converged for the specimens with scale ratio 12. Note that it is experimentally challenging to perform the tests on specimens with larger scale ratio, due to the necessity of thicker specimens to prevent global buckling making the specimen processing infeasible. And also due to the difficulty of attaining high spatial resolution of the displacement and thus rotation fields inside the islands, while capturing the complete surface of the specimens within the field of view.

Three more numerical simulations are conducted to analyse larger specimens. At a scale ratio of 18, the boundary layer size almost levels out, showing an asymptotic trend corresponding to a boundary layer size of roughly 4 unit cells. Extending the simulations to bigger scale ratios is infeasible since global buckling occurs almost immediately after local buckling, preventing analysis of the rotation fields before global buckling. Note that the presented results are all determined at $\varepsilon + 0.013$, which guarantees that all specimens up to scale ratio 18 are not globally buckled.

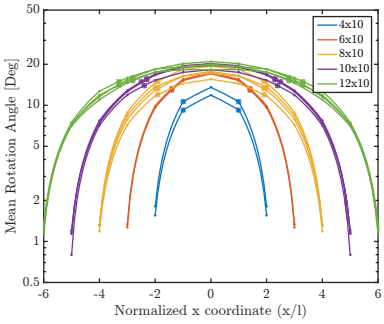

(a) Experimental mean rotation angle

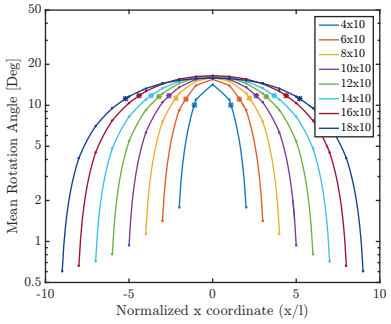

(b) DNS mean rotation angle

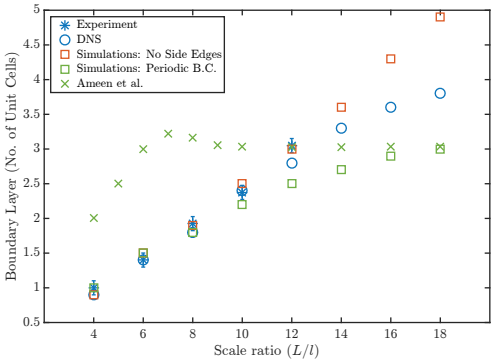

(c) Boundary layer size

Figure 4.5: Local behaviour of specimens of different scale ratios based on experimental and numerical results. Rotation angles averaged over the two central unit cells against the horizontal coordinate for (a) experimental, where results of all the tests for each scale ratio are depicted in the same color and, (b) numerical results, at a relative global strain of $\varepsilon_b + 0.013$. The stars are depicting 70% of the dynamic range of each curve for quantification of the boundary layer size. Graphs in (a) and (b) are plotted on logarithmic vertical scales to better visualize the boundary layers. (c) Size of the boundary layer, in terms of the number of unit cells, determined from the rotation of the islands, for the experimental and numerical data as well as for the simulations by [44]. The simulations are extended to a scale ratio of 18 to reveal the converged size of the boundary layer.

Results of two additional sets of numerical simulations with different lateral constraints are included in Fig. 4.5c as well. In both cases the bulk side edges in the loading direction and 10 unit cells over the specimen width are employed. First, specimens with different scale ratios but no bulk side edges are analysed, which imposes no lateral constraint on the metamaterial. Second, infinitely wide specimens are computed by means of periodic boundary conditions, which applies a high level of lateral constraint on the metamaterial. As mentioned above, the 70% threshold is chosen to have the boundary layer thickness of this case to match those of [44], for large scale ratios. They used a different measure, i.e. maximum curvature of the axial component of deformation gradient tensor, to assess the boundary layer size with respect to this study, but the asymptotic boundary layer thickness should be independent of the method used to quantify it. The boundary layer size in their study is evaluated from a homogenized solution based on many shifted realizations of the microstructure, in many of which the holes cut through the edges. For small scale ratios, this results in a different boundary layer thickness evaluated based on one single realization (no microstructural shift) and the thickness assessed from the homogenized solution, which explains the difference between the simulations of the current study with periodic boundary conditions and results of [44].

It is observed that the different levels of lateral confinement directly influence the scale ratio at which the boundary layer size converges, see Fig. 4.5c. The experimental specimens of the current study are in between these two limit cases of lateral confinement, which explains why the boundary layer size was not fully converged in the experimental data.

The presented results demonstrate that relatively large boundary layers emerge in cellular elastomeric metamaterials, which result in considerable size effects in specimens of finite size. These effects are tunable to a certain degree by changing the constraints put on the specimens in the transverse direction, which can be exploited for customized designs of these metamaterials in various engineering applications.

4.4 Summary and Conclusions

Cellular elastomeric materials exhibit pattern transformations beyond a critical load, entailing internal buckling of their microstructure, which may dramatically change influences their global mechanical response. To experimentally analyse the size effects in such materials, as previously observed in a numerical study of [44], a systematic study has been conducted. To remain consistent with potential applications of cellular elastomers, specimens with millimetre sized holes have been manufactured using custom-made moulds. The size of the specimen with respect to hole size, i.e. “scale ratio”, was varied while keeping the hole size fixed. *In-situ* micro compression tests in conjunction with optical microscopy and digital image correlation have been conducted to attain full-field kinematic measurements. Such measurements are essential to accurately assess the global stress–strain behaviour of the specimens and to evaluate the

local kinematics during pattern transformation, which allows to extract the boundary layer thickness. Unlike done in the numerical study mentioned above, real specimens are by definition finite in size and ensemble-average homogenized solutions are not applicable, making a direct comparison challenging. To overcome this difficulty, finite element simulations of finite sized specimens have been conducted here and analysed in parallel to the experiments. Tensile tests have been performed to characterize the bulk material, allowing to identify the Ogden hyper-elastic material parameters. The experimentally observed geometrical variations within the specimens have been incorporated to assess the uncertainties characterising the real specimens.

The global stress–strain behaviour, local buckling strain and post-buckling stress for different scale ratios adequately agree between numerical and experimental results, taking into account the specimen variations and uncertainties. The global stress shows a trend of the same order of magnitude as the one reported by [44], while the difference is mainly due to the very different boundary conditions in the two studies. In order to determine the size of the boundary layer, the spatial variation of the rotation angle of cross-islands inside each specimen was studied. The numerical and experimental results agree well, although the boundary layer size did not yet converge to an asymptotic value for the maximum scale ratio used in the experiments. The numerical results indicate convergence of the boundary layer size towards approximately 4 unit cells. Additional numerical investigations, where the lateral constraint acting on the specimens was varied, reveal that the level of lateral confinement of the cellular elastomeric metamaterials strongly influences the boundary layer and its convergence to a saturated value. Relaxation of the lateral constraints results in larger boundary layers and larger scales ratios for which the boundary layer size has converged. These novel insights are instrumental for controlling the boundary layer size and size effects in designs based on cellular metamaterials.

Appendices

4.A Material Characterization

Dog-bone specimens, with a gauge length of 12 mm and a width of 2.2 mm, are punched out of PDMS slabs, which are processed along with the manufacturing of the metamaterial specimens. The thickness of these dog-bone specimens varies between 1.0 to 1.5 mm for different batches. A similar speckle pattern as described in Section 4.2.3 is applied on the dog-bone samples, and *in-situ* tensile tests are performed. Loads are measured with a 50 N load cell. Global DIC, in which the displacement field is parametrized with linear polynomials, is used to measure the strains inside the specimens. Adopting hyper-elastic Ogden material model, the material parameters are identified by minimizing the difference between the reaction force of a finite element model of a material point under uniaxial tension and the experimentally measured forces. The strain energy

density function is given by:

$$W = \frac{1}{2}\kappa\,(J-1)^2 + \sum_{k=1}^{N} \frac{c_k}{m_k^2}\,(\lambda_1^{m_k} + \lambda_2^{m_k} + \lambda_3^{m_k} - 3 - m_k \ln J)\,, \tag{4.1}$$

where λ_i are the principal stretches, $J = det(\mathbf{F})$ is the volume change ratio, $\mathbf{F}$ the deformation gradient tensor, κ is the bulk modulus, and c_k and m_k are the material parameters, with N taken equal to 2 in this study [85]. The principal stresses, σ_i, are given as:

$$\sigma_i = \kappa\,(J-1) + \sum_{k=1}^{N} \frac{1}{J}\frac{c_k}{m_k}\,(\lambda_i^{m_k} - 1)\,, \tag{4.2}$$

The initial values for c_k and λ_k as well as the bulk modulus are chosen from Ref. [82], due to the similar PDMS processing utilized in that study. Considering the variety of values reported for the bulk modulus of Sylgard 184 in literature, varying from 20 to 1200 MPa [81, 82, 85], it was decided to perform confined compression tests on circular samples of 5 mm diameter punched from PDMS slabs to evaluate the bulk modulus. An average of 415 MPa and standard deviation of 125 MPa was found for bulk modulus over ten tests. The low average is due to air bubbles observed under optical microscope, while the large standard deviation is due to the non-uniform distribution of the air bubbles. It is realized, however, that the degassing process in the metamaterial specimens is less effective, considering their thickness and complicated design, which will for sure leave more bubbles in these metamaterial specimens than for the flat compression specimens and thus results in a lower bulk modulus. Therefore, the low initial guess for the bulk modulus obtained from Ref. [82], i.e. 29.15 MPa, seems to be a reasonable value to use as initial guess.

A staggered approach is used to identify all five material parameters. First, c_k are optimized for strains up to 2%, then c_k and m_k are optimized for the entire strain range, i.e. up to 60%. The bulk modulus is finally found for the whole strain range while keeping the optimized values of c_k and m_k constant. This approach results in optimized values of $\kappa = 29.6716$ MPa, $c_1 = 0.0892$ MPa, $c_2 = 1.2537$ MPa, $m_1 = 10.0959$ and $m_2 = 0.0036$. Note that a separate numerical investigation revealed only 2% change in initial mechanical response of metamaterial specimens for a change of bulk modulus from 30 to 1000 MPa, thus revealing a very small sensitivity to this material parameter.

Chapter 5

Harvesting micromorphic fields from experiments on patterning metamaterials

Reproduced from:
S. Maraghechi, O. Rokoš, J. P. M. Hoefnagels, R. H. J. Peerlings, M. G. D. Geers
Harvesting micromorphic fields from experiments on patterning metamaterials, 2019,
Submitted.

Abstract

Cellular elastomeric metamaterials generally exhibit local buckling patterns that emerge at a critical level of compressive load. For the analysis and design of metamaterials with dedicated functionalities it is useful to distinguish the displacement pattern due to local buckling from the overall deformation. A recent study proposed a micromorphic computational homogenization scheme, suitable for cellular metamaterials, based on a kinematical ansatz consisting of three parts: (i) a smooth mean displacement field, corresponding to the slowly varying deformation at the macro-scale, (ii) a long-range correlated fluctuation field, related to the buckling pattern at the meso-scale and, (iii) the remaining uncorrelated local microfluctuations at the micro-scale. The current study aims at experimentally identifying the decomposed kinematics of cellular metamaterials based on this ansatz. To this end, a novel micromorphic Integrated Digital Image Correlation (IDIC) method is developed. The methodology is applied to cellular elastomeric metamaterials in both virtually generated images and images attained during *in-situ* compression of specimens with millimetre sized microstructure using optical microscopy. The novel micromorphic IDIC method effectively decomposes the different kinematic fields, both before and after the emergence of the long-range correlated fluctuations. The methodology is easily extended to account for cellular metamaterials with different microstructural designs.

5.1 Introduction

Mechanical metamaterials exhibit exotic behaviour that is of great interest for dedicated applications such as soft robotics or tunable materials [74]. The focus of this paper is on cellular elastomeric metamaterials which reveal a pattern transformation at a critical level of compressive load, resulting in a significant change in their mechanical response. Fig. 5.1 shows an example of a cellular elastomeric metamaterial with a regular grid of circular holes, where the local buckling of the microstructure results in a patterned fluctuation field that is correlated over long distances.

Different applications of cellular elastomeric metamaterials, such as strain tunable photonic crystals [42], soft robotics [40, 41], programmable mechanical metamaterials [43], functionally graded metamaterials [75], are being studied in the literature. Various aspects of such metamaterials with 2D [29] and 3D [36, 39] microstructures have been studied. A number of studies focus on the effect of the hole geometry and stacking [30–33]. [86] made a qualitative comparison between numerically and experimentally assessed stresses in cellular elastomers; [76] used 3D printing to manufacture and study multi-material mechanical metamaterials; [77] investigated different pattern transformations as a result of swelling in cellular hydrogel membranes, [78] investigated the effect of friction on buckling pattern formation in cellular structures; and [44] conducted a computational study on the size effects in cellular metamaterials.

Few studies in the literature made use of full-field displacement measurement techniques to investigate cellular metamaterials. [35] used local Digital Image Correlation (DIC) to validate their numerical study on auxetic metamaterials; [37] used DIC in the design of thermally expanding tunable 3D metamaterials; [38] studied different designs of auxetic dome-shaped structures using stereo DIC; and [34] compared DIC and finite element analysis results on highly stretchable and reconfigurable metamaterials. Such full-field kinematic assessments, based on local DIC, all provide complex displacement fields consisting of a smooth part and complicated fluctuations depending on the microstructural design. Decomposition of these complex kinematics proves to be useful in different applications, such as metamaterials for which the tunable phononic properties depend on the local distribution of patterned fluctuations [87–89]. Therefore, it is important to be able to identify this distribution, independently from the global deformation, for a proper assessment of and design for certain effective phononic properties. There are many other applications, such as auxetic metamaterials [90, 91] and biomedical prosthetics [92, 93], for which tuning the complex fluctuations at the scale of the microstructure also guides the desired architectured global behaviour. Therefore, measurement of the global macroscopic deformation field separately from the meso-scale fluctuation field is of clear interest.

In a recent numerical study [45], a micromorphic homogenization scheme was introduced, suitable for cellular elastomeric metamaterials, which is based on the decomposition of the displacement field according to the following ansatz,

$$\mathbf{u}(\mathbf{x}) = \mathbf{v}_0(\mathbf{x}) + \sum_{i=1}^{n} v_i(\mathbf{x})\,\boldsymbol{\varphi}_i(\mathbf{x}) + \mathbf{w}(\mathbf{x})\,. \tag{5.1}$$

The total displacement field $\mathbf{u}(\mathbf{x})$ is divided into three parts: (i) the mean smooth displacement field, $\mathbf{v}_0(\mathbf{x})$, corresponding to the slow variations at the macro-scale; (ii) long-range correlated fluctuations at the meso-scale represented by the vector fields $\boldsymbol{\varphi}_i(\mathbf{x})$, with $i = 1, \ldots, n$, scaled by their magnitudes in space $v_i(\mathbf{x})$; and (iii) a remaining microfluctuation field, $\mathbf{w}(\mathbf{x})$, which represents the non-correlated fluctuations at the micro-scale. In here, $\mathbf{x}$ is the position of material points in the undeformed configuration.

The same decomposition is used here to develop an experimental method to qualify and quantify the decomposed kinematic fields of cellular elastomeric metamaterials, using images captured at different stages of deformation during an experimental test. To this end, a novel micromorphic Integrated Digital Image Correlation (IDIC) is developed, in which the total displacement field is described by only (i) the smooth mean part and (ii) the long-range correlated fluctuation field. IDIC is a full-field displacement measurement technique based on regularization of the kinematics according to specific knowledge about the problem at hand. Typically this prior knowledge is applied in the form of a numerical model describing the mechanics with the material parameters as the degrees of freedom. It can then be used to directly find the material properties from *in-situ* tests. However, such a knowledge of the nature of the problem at hand can be integrated with DIC scheme in form of a parametric analytical description, which is useful when the kinematic fields are of interest. The total displacement field is regularized based on the above-mentioned ansatz by parametrization of the smooth mean field, $\mathbf{v}_0$, the long-range correlated fluctuation modes carried by the microstructure, $\boldsymbol{\varphi}_i$, as well as their spatial distribution functionals, $v_i(\mathbf{x})$. The proposed methodology is applicable for a general class of cellular metamaterials.

The methodology is tested on virtually generated and deformed images, as well as optical microscopy images taken during an *in-situ* compression test on a cellular elastomeric metamaterial with rectangular stacking of circular holes, cf. Fig. 5.1. A spectral density analysis is shown to be effective for fine tuning the parametrization and initialization of the fluctuation mode for a specific metamaterial. It is demonstrated that the micromorphic IDIC scheme leads to a proper decomposition of the kinematic fields into their smooth mean field, the fluctuation mode and its spatial distribution over the specimen, both before and after the emergence of the fluctuation pattern.

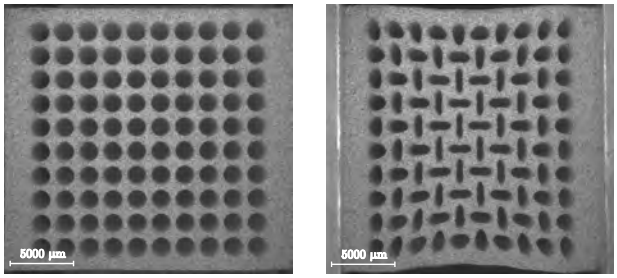

(a) Undeformed microstructure (b) Deformed microstructure

Figure 5.1: Elastomeric metamaterial specimen (a) before and (b) after the onset of microstructural buckling, due to compression in horizontal direction, resulting in the emergence of an anti-symmetric pattern.

5.2 Micromorphic Integrated Digital Image Correlation

5.2.1 Integrated Digital Image Correlation

Integrated image correlation is a full-field displacement measurement method based on the minimization of the residual field, which is the difference of the reference image, f, and the deformed image, g, probed at, respectively, reference coordinates and the deformed positions corresponding to those coordinates based on the displacement field. The problem is solved over the whole region of interest, where the residual field is defined as

$$r(\mathbf{x}, \underline{\mathbb{o}}) = f(\mathbf{x}) - g(\boldsymbol{\phi}_M(\mathbf{x}, \underline{\mathbb{o}})). \tag{5.2}$$

$\boldsymbol{\phi}_M(\mathbf{x}, \underline{\mathbb{o}}) = \mathbf{x} + \mathbf{u}(\mathbf{x}, \underline{\mathbb{o}})$ is the mapping function corresponding to the mechanical displacement field, $\mathbf{u}$. The displacement field, in turn, is based on the regularization according to a model with specific knowledge of the kinematics at hand, thereby reducing the number of degrees of freedom (dof) contained in $\underline{\mathbb{o}}$, and improving the robustness of the solution [94]. This model can be a numerical model in which the dofs would be the material parameters or an analytical model describing the deformation field. The optimal values of the degrees of freedom, $\underline{\mathbb{o}}^{opt}$, are found as:

$$\underline{\mathbb{o}}^{opt} = \underset{\underline{\mathbb{o}}}{\operatorname{argmin}} \left(\frac{1}{2} \int r^2(\mathbf{x}, \underline{\mathbb{o}}) \, d\mathbf{x} \right) \tag{5.3}$$

This minimization problem is then solved by an iterative scheme such as Gauss-Newton [61].

5.2.2 Regularization of the Kinematics based on the Micromorphic Kinematical Ansatz

The kinematical ansatz introduced in Eq. (5.1) is used to experimentally obtain the decomposed kinematic fields of cellular metamaterials. The local microfluctuations are the non-correlated part of the kinematics and by definition unknown, therefore $\mathbf{w}(\mathbf{x})$ is not included in the micromorphic IDIC parametrization for cellular metamaterials. Accordingly, the displacement field for the IDIC problem is defined as:

$$\mathbf{u}\left(\mathbf{x}, \underline{\mathbb{q}}\right) = \mathbf{v}_0\left(\mathbf{x}, \underline{\mathbb{q}}_{v_0}\right) + \sum_{i=1}^{n} v_i\left(\mathbf{x}, \underline{\mathbb{q}}_{v_i}\right) \boldsymbol{\varphi}_i\left(\mathbf{x}, \underline{\mathbb{q}}_{\varphi_i}\right), \tag{5.4}$$

where $\underline{\mathbb{q}} = \left[\underline{\mathbb{q}}_{v_0}\ \underline{\mathbb{q}}_{v_i}\ \underline{\mathbb{q}}_{\varphi_i}\right]^{\mathsf{T}}$ is the column of degrees of freedom, with $\underline{\mathbb{q}}_{v_0}$, $\underline{\mathbb{q}}_{v_i}$ and $\underline{\mathbb{q}}_{\varphi_i}$ the sets of dofs for $\mathbf{v}_0$, v_i and $\boldsymbol{\varphi}_i$ respectively. Since each mode $\boldsymbol{\varphi}_i$ is periodic within an integer multiple of the unit cell size [45], a truncated 2D Fourier series is a natural choice for its parametrization. As will be shown below, the selection of relevant sine waves can be easily done by means of a simple spectral density analysis of one example for any family of cellular metamaterials and loading conditions. Note that the number of modes that are activated by different loading conditions in cellular metamaterials is often only one, e.g. Fig. 5.1, or just a few [95]. Each long-range correlated fluctuation mode $\boldsymbol{\varphi}_i$ is defined such that it is non-zero only where the cellular microstructure exists. In order to avoid discontinuities, its smoothly goes to zero in bulk edges of the specimen, if present. This is accounted for, such that the periodic field of each mode is extended in the bulk material while its value linearly decays to zero inside a region of bulk material with a width of half the unit cell size. Because $\mathbf{v}_0$ and v_i are slow macroscopic fields, smooth functions such as globally-supported polynomials are the best choice for their parametrization.

In an *in-situ* test, in addition to the mechanical displacement field, the images are affected by optical distortions of the optical lenses. Such distortions may introduce large errors if neglected. Therefore, the residual field of Eq. (5.2) is rewritten as:

$$r(\mathbf{x}, \underline{\mathbb{q}}) = f\left(\boldsymbol{\phi}_S\left(\mathbf{x}\right)\right) - g\left(\boldsymbol{\phi}_S\left(\boldsymbol{\phi}_M(\mathbf{x}, \underline{\mathbb{q}})\right)\right), \tag{5.5}$$

where $\boldsymbol{\phi}_S(\mathbf{x}) = \mathbf{x} + \mathbf{S}(\mathbf{x})$ is the mapping function describing the spatial distortion. The spatial distortion field, $\mathbf{S}(\mathbf{x})$, is determined a priori in a calibration step by the method introduced in Chapter 3 [65, 79]. Hence there are no degrees of freedom related to spatial distortion to be identified anymore in the micromorphic IDIC problem, of Eq. (5.3).

5.3 Results and Discussion

The methodology is applied to both virtual and real *in-situ* micro-compression experiments on cellular elastomeric metamaterial specimens with a design as depicted in Fig. 5.2. The specimen has 1.5 mm hole diameters and 1.9 mm center to center pitch

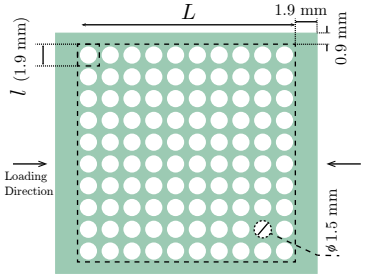

Figure 5.2: Analysed cellular elastomeric metamaterial specimen, depicting the total length of specimen excluding the bulk side edges (L: the large dashed square), the size of the unit cells ($l = 1.9\ mm$: small dashed square), hole diameter ($1.5\ mm$), the size of the bulk side edges and the loading direction.

(unit cell size l) with edges of 1.9 mm and 0.9 mm bulk material in loading and transverse directions. The length of the specimen, excluding the bulk edges, is denoted L. The scale ratio of the specimen, L/l, is equal to the number of holes in the loading direction. More details on the specimen geometry are found in Chapter 4.

5.3.1 Virtual Experiments

The micromorphic IDIC scheme will be first tested on virtually generated and deformed speckle images. By this means the method is tested in a case where there is no influence of image distortions and noise in the images, and there are no imperfections in the specimen and the loading, etc. To this end, a plane strain finite element simulation, using quadratic isoparametric triangular elements with three-point Gauss integration rule, is performed for the compression of a cellular elastomeric metamaterial specimen with scale ratio of 6, i.e. 6 and 10 holes in loading and transverse directions, respectively. Dirichlet boundary conditions are applied on the two vertical edges perpendicular to the loading direction to apply compression, while the two remaining edges are free. The material, i.e. PDMS, is modelled by a hyper-elastic Ogden material model. More details on the numerical simulation are presented in Chapter 4. The displacement fields obtained from this simulation are used to deform a speckle pattern for two different time steps, one before microstructural buckling and the other after the emergence of the patterned fluctuation field, corresponding to 7.8% and 12.8% applied nominal strain. Fig. 5.3a depicts the deformed configuration of the virtual speckle pattern after the buckling-induced pattern emerged, which exhibits the pattern transformation more pronounced in the center and restricted at the edges, specifically the vertical edges. The employed speckle pattern is obtained as a thresholded two-dimensional scalar and stationary random Gaussian field, generated according to [Section 5.3.1.2 96]. The spectral density is chosen as a radially-symmetric normal probability density function with the mean zero and standard deviation 1/20. No additive image white noise has been added to

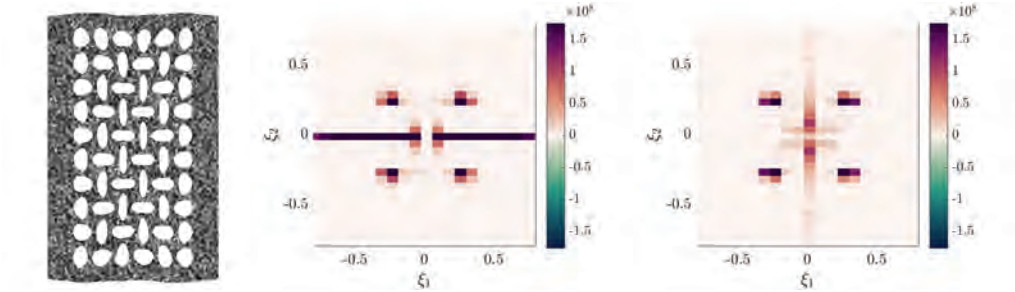

(a) Deformed virtual image (b) S_{xx} $[mm^6]$ (c) S_{yy} $[mm^6]$

Figure 5.3: (a) Virtually generated and deformed speckle pattern, corresponding to compression in horizontal direction after the onset of pattern transformation in a cellular elastomeric metamaterial, revealing the presence of one fluctuation mode inside the specimen. Energy spectral density functions of the corresponding displacement field in (b) x and (c) y direction, revealing the principal frequencies related the long-range correlated fluctuation mode (four peaks approximately on the diagonals). The range of the colorbars is reduced to highlight the frequencies related to the long-range correlated fluctuation mode.

such generated images. The pattern is blurred using Gaussian filter with the standard deviation of 3 pixels.

No imaging spatial distortions are present in the virtual images, and thus $\boldsymbol{\phi}_S(\mathbf{x}) = \mathbf{x}$ is set for the virtual experiments. Chebyshev polynomials of 5th and 6th order are used to parametrize $\mathbf{v}_0$ and v_1, respectively. In order to attain a proper initial guess for $\boldsymbol{\varphi}_i(\mathbf{x}, \underline{\mathbb{o}}_{\varphi_i})$, it is first observed, cf. Fig. 5.3a, that only one long-range correlated fluctuation mode is triggered in the specimen, thus $n = 1$ is set in Eq. (5.1) with only $\boldsymbol{\varphi}_1$ considered. It is also obvious that the triggered mode is periodic wth a periodicity of two unit cells. Moreover, a spectral density analysis is performed on the reference displacement field, available from the simulation. Figs. 5.3b and c depict the energy spectral densities of the displacement components in horizontal and vertical directions, $S_{xx} = \hat{u}_x(\xi)\hat{u}_x^*(\xi)$ and $S_{yy} = \hat{u}_y(\xi)\hat{u}_y^*(\xi)$, respectively, where u_x and u_y are the x- and y- components of $\mathbf{u}(\mathbf{x})$, the hat indicates the Fourier transformation and * complex conjugate. Inspection of these two graphs allows to make a specific choice on the parametrization and initialization of the long-range correlated fluctuation mode. The horizontal and vertical lines in Figs. 5.3b and c, respectively, correspond to the discontinuities in the mean deformation due to the edges of the specimen, while the four peaks correspond to the correlated fluctuation mode, revealing two sine functions roughly in diagonal directions of the Cartesian coordinate system, for the x and y components of $\boldsymbol{\varphi}_1$. In the spectral densities there are a multitude of secondary peaks, corresponding to the microfluctuations $\mathbf{w}$, which are not visible due to their small amplitudes. The purpose of the spectral density analysis is the identification of the long-range correlated

fluctuation modes, so only the corresponding four peaks are considered here. Inspection of $\hat{u_x}(\xi)$ and $\hat{u_y}(\xi)$, at the frequencies corresponding to the four peaks of S_{xx} and S_{yy}, suggests that the two sine waves are of the same sign in the x component, and of the opposite sign in the y component of the displacement field. This inspection also suggests that the two sine waves are of the same amplitude, for both x and y components of the displacement. Based on these observations, $\boldsymbol{\varphi}_1$ is parametrized as the sum of two sine functions for each component, as:

$$\begin{aligned}\boldsymbol{\varphi}_1(\mathbf{x}, \underline{\mathbb{o}}_{\varphi_1}) = a_1 \Big[sin\frac{\pi}{l}(a_2 x + a_3 y + a_6) - sin\frac{\pi}{l}(a_4 x + a_5 y + a_7) \Big] \mathbf{e}_x \\ + \Big[sin\frac{\pi}{l}(a_2 x - a_3 y + a_6) - sin\frac{\pi}{l}(a_4 x + a_5 y + a_7) \Big] \mathbf{e}_y, \end{aligned} \tag{5.6}$$

where $\underline{\mathbb{o}}_{\varphi_1} = [a_1, a_2, a_3, a_4, a_5, a_6, a_7]^\mathsf{T}$ is the column of degrees of freedom describing the mode. Note that the direction of both sine waves and their wavelengths are free and independent, which compensates for inaccuracies in the measurement of the unit cell size, due to processing uncertainties. This allows for an accurate assessment of the shape of the fluctuation mode, whereas the spectral density analysis is only used for a proper parametrisation of the fluctuation mode and for the initial guess of all these parameters. Note also that it is sufficient to perform the spectral density analysis only once for a family of cellular metamaterials triggering the same pattern. In cases where more than one mode is activated, the spectral analysis should be done separately on each of the regions containing the individual modes.

The dofs describing $\boldsymbol{\varphi}_1$ are initialized as: $\underline{\mathbb{o}}_{\varphi_1} = [1, 1, 1, 1, 1, 0, 0]^\mathsf{T}$. The initial values for a_2 to a_5 are set to a wavelength of 2 unit cells and their signs and ratios are set such that the initial orientation of the two sine waves is aligned with the two diagonals of the coordinate system. Note that a_1 is only defining the ratio of the amplitude of the mode in x and y direction, while $v_1(\mathbf{x})$ defines its absolute amplitude according to Eq. (5.4). In order to assure a proper scaling of the minimization problem, $\boldsymbol{\varphi}_1(\mathbf{x})$ is scaled such that the initial maximum value of the mode is 0.04. Since the sensitivity functions of the mode $\boldsymbol{\varphi}_1$ used in the Gauss-Newton optimization algorithm [61] are a function of $v_1(\mathbf{x})$, the initial guess for the latter needs to be non-zero to avoid an ill posed problem in the first iteration. To this end, $v_1(\mathbf{x})$ is initiated with a small constant value in space. The applied compressive global strain results in large displacement on the edges of the specimen requiring an approximate initial guess in order to ensure convergence. Thus, the smooth mean field $\mathbf{v}_0(\mathbf{x})$ is initialized such that the first order term in x direction approximately accounts for the applied global strain.

The micromorphic IDIC results in a proper identification of the $\mathbf{v}_0(\mathbf{x})$, $v_1(\mathbf{x})$ and $\boldsymbol{\varphi}_1(\mathbf{x})$, considering the residual fields that are small everywhere both before and after buckling occurs, see Figs. 5.4g and o. The convergence is consistent and the methodology is robust with respect to the initial values. Fig. 5.4 shows the results of the virtual experiments before (left) and after (right) the emergence of the buckling pattern. For each case, the mean smooth displacement field, $\mathbf{v}_0(\mathbf{x})$, in x and y directions, and $v_1(\mathbf{x})$ are depicted in the first two rows, i.e. Figs. 5.4a–c before and Figs. 5.4i–k after buckling

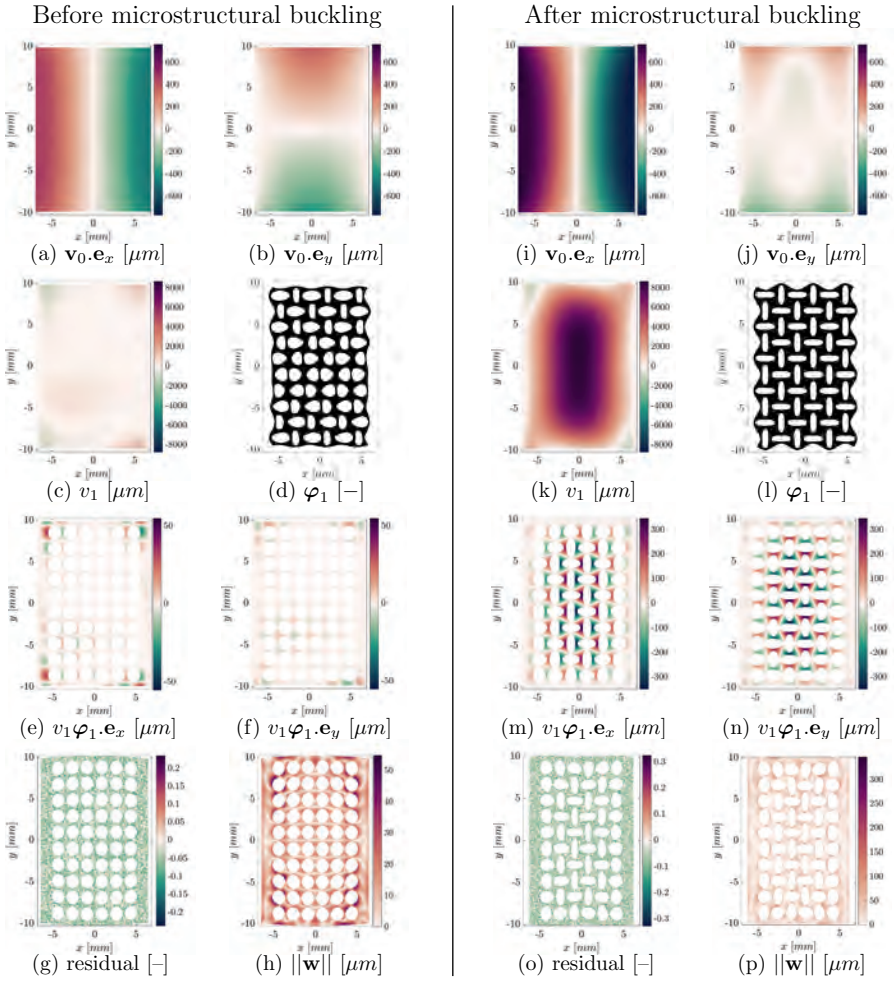

Figure 5.4: Results of the virtual experiments before (left) and after (right) the onset of microstructural buckling: (a, b, i, j) the smooth mean displacement fields, $\mathbf{v}_0(\mathbf{x})$, in (a, i) x and (b, j) y directions; (c, k) the pattern amplitudes, $v_1(\mathbf{x})$, (d, l) the deformed configuration of identified patterns/modes, $\boldsymbol{\varphi}_1(\mathbf{x})$, scaled to assure the visibility of the deformed shape, and (e, f, m, n) the resulting fields, (e, m) in x and (f, n) y directions, corresponding to the long-range correlated fluctuations. In (d, l) $\boldsymbol{\varphi}_1(\mathbf{x})$ are scaled to assure the visibility of the deformed shape of the modes. The long-range correlated fluctuation fields, $v_1(\mathbf{x})\boldsymbol{\varphi}_1(\mathbf{x})$, are plotted in the deformed configuration corresponding to their contribution only. (g, o) are the residual fields in normalized gray scales; and (h, p) the Euclidean norm of the microfluctuation field, $\mathbf{w}(\mathbf{x})$, plotted in deformed configuration based on the total displacement.

occurs. The $\mathbf{v}_0$ fields show compression in x direction both before and after buckling (a linear profile). Before pattern transformation, lateral expansion is visible in y direction, while afterwards the auxetic effect, i.e. lateral contraction, is clearly visible near the specimen's center. As expected, the v_1 field is close to zero before buckling occurs, although its absolute value increases slightly in the corners of the region with cellular microstructure (the area of the specimen excluding the bulk edges), which is due to the fact that the fluctuation mode, $\boldsymbol{\varphi}_1$, partially captures the deformation that occurs in the corner holes where the edge effect is considerable. After the buckling occurs, the v_1 field is close to zero on the edges and increases towards the center, as expected. Again, v_1 is not exactly zero at the edges and the corners of the metamaterial, since the fluctuation mode partially describes the deformation in the corners where the edge effect is considerable. Note that the large values in $v_1(\mathbf{x})$ are due to the scaling of the corresponding mode $\boldsymbol{\varphi}_1$ (maximum value of 0.04).

The identified long-range correlated mode, $\boldsymbol{\varphi}_1(\mathbf{x})$, is depicted in Figs. 5.4d and l for before and after buckling, respectively, where their amplitudes are scaled to assure the visibility of the deformed shape of the modes. The small v_1 prior to buckling entails a low sensitivity of the mode parameters. As a result, $\boldsymbol{\varphi}_1$ is significantly perturbed with respect to the initial guess, see Fig. 5.4d where the periodicity does not match twice the unit cell size anymore. After buckling, however, the mode becomes representative and it resembles the initial guess more closely and matches the mode observed in the simulations (Fig. 5.4l). The long-range correlated fluctuation fields, $v_1\boldsymbol{\varphi}_1(\mathbf{x})$ in x and y directions, are depicted in their deformed configurations prior to buckling, in Figs. 5.4e and f and beyond buckling in Figs. 5.4m and n. Prior to buckling, $v_1\boldsymbol{\varphi}_1(\mathbf{x})$ is close to zero everywhere apart from the four corners, where the identified mode, although significantly perturbed with respect to the initial guess, partially captures the edge effect, as described above. Post buckling, $\boldsymbol{\varphi}_1$ is identified properly, resulting in small modifications to the wavelengths and orientations of the sine waves compared to the initial guess based on spectral density analysis.

The residual fields in normalized gray scales before and after buckling are shown in Figs. 5.4g and o, in the deformed configuration based on the total evaluated displacement $\mathbf{u}(\mathbf{x})$. The residual fields are consistently small everywhere over the region of interest. However, the microfluctuation fields, discarded in the micromorphic IDIC scheme seeking to extract correlated fields only, are by definition reflected in the residual fields. In order to evaluate the performance of the method, the microfluctuation field $\mathbf{w}(\mathbf{x})$ is recovered as the difference of the reference displacement field (here available from the simulation) and the displacement field $\mathbf{u}(\mathbf{x})$ according to Eq. (5.4). The Euclidean norm of the microfluctuation field, $||\mathbf{w}||$, is depicted in Figs. 5.4h and p before and after the buckling, respectively. Note that the micromorphic IDIC scheme is constrained to identify displacement fluctuations with spatial frequencies bound to the highest spatial frequencies in the long-range correlated fluctuation modes, $\boldsymbol{\varphi}_i$. Thus, the microfluctuation field, $\mathbf{w}$, contains all parts of the signal with spatial frequencies higher than the characteristic frequency of $\boldsymbol{\varphi}_1$, as well visible far from the edges of the specimen in the post buckling case, see Fig. 5.4p. As expected, the microfluctuation field, $\mathbf{w}$, is of

a significantly smaller amplitude than the correlated fluctuation field beyond buckling (compare Fig. 5.4p with Figs. 5.4m and n). The opposite is true prior to buckling, due to the almost negligible contribution of the long-range correlated fluctuation field (compare Fig. 5.4h with Figs. 5.4e and f). Note the difference in scale bars for the figures of the pre- and post-bifurcation state.

In order to assess the robustness of the method, the correlations of the virtual experiments, after the onset of buckling, are repeated with different initial guess values for the fluctuation mode. The values of $\underline{\mathbb{q}}_{\boldsymbol{\varphi}_i}$ are perturbed by a random value up to 10% of the nominal value stated above, resulting in random changes in the wavelengths and orientations of the sine waves as well as the ratio of the the x and y components of $\boldsymbol{\varphi}_1$. The perturbed correlations are repeated 100 times, and the error in each case is evaluated as: $\epsilon = 100 \times \frac{||\mathbf{u}||-||\mathbf{u}_{pert}||}{||\mathbf{u}||}$, where $\mathbf{u}$ is the total displacement field evaluated with no perturbation of initial guess, and $\mathbf{u}_{pert}$ is the perturbed total displacement field. The error averaged over all the repetitions is 0.86%, entailing only two cases with an erroneous assessment of the total displacement field, i.e. $\epsilon > 1.5\%$, confirming the 98% robustness of the method to initial guess. The average error ϵ, ignoring the two outlier cases, is 0.45%, confirming the high accuracy of the methodology.

5.3.2 Real Experiments

The results of an *in-situ* compression test on a cellular elastomeric metamaterial specimen, manufactured using a customised mould as explained in Chapter 4, are analysed with the micromorphic IDIC method. The real experiment includes some complexities with respect to the virtual experiment, such as the image distortions and noise as well as the imperfections in the specimens and loading conditions of the test. The specimen is $22.5mm$ thick and has 12 and 10 holes in loading and transverse directions, respectively, corresponding to a scale ratio 12. The specimen is made of Sylgard 184, with a 10:1 mixing ratio. A two-layer speckle pattern is deposited on the top surface (white powder sprayed to make a fine grained background and India ink sprayed using an air brush, see Fig. 5.5a), resulting in a speckle size between 30 and $80\mu m$ (3 to 8 pixels). An *in-situ* compression test is performed with a Kammrath & Weiss micro tensile/compression stage with a 50 N load cell, while a Zeiss V20 stereo microscope is used to acquire images at each load step at 7.6× magnification and 2751×2207 pixels. More details on the specimen processing and the *in-situ* test is given in Chapter 4. Two images obtained during the *in-situ* test, before and after the emergence of the buckling pattern, corresponding to 8.2% and 12.7% applied nominal strain on the metamaterial, are correlated to the undeformed reference configuration. The deformed configuration after emergence of the buckling pattern is shown in Fig. 5.5a.

A spatial distortion calibration step, explained in Chapter 3 [65, 79], is performed to measure the spatial distortions of the imaging system at the desired magnification. The resulting distortion field, which is as large as 10% of the actual displacements, is used to construct the distortion mapping function $S(\mathbf{x})$.

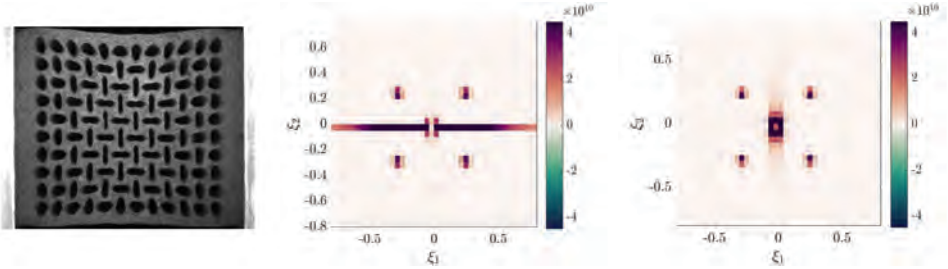

(a) Deformed Image (b) S_{xx} $[mm^6]$ (c) S_{yy} $[mm^6]$

Figure 5.5: (a) Image of the deformed configuration of a cellular elastomeric metamaterial with millimetre-sized circular holes in a rectangular stacking, corresponding to a compressive load step after the onset of pattern transformation, acquired during an *in-situ* compression test. Energy spectral density functions of the displacement field, assessed by local DIC, in (b) x and (c) y direction, revealing the principal frequencies related to the long-range correlated fluctuation mode (four peaks approximately on the diagonals). The range of the colorbars is reduced to highlight the frequencies related to the long-range correlated fluctuation mode.

Chebyshev polynomials of 5th and 6th order are used to parametrize $\mathbf{v}_0$ and v_1, respectively. The same procedure as in the case of virtual experiments is performed for estimating the reduced regularization of $\boldsymbol{\varphi}_1(\mathbf{x})$ and the initialization of the associated parameters. To this end, first, the post buckling kinematics is determined using local DIC, in order to attain S_{xx} and S_{yy}, shown in Figs. 5.5b and c. Similar to the virtual experiments, vertical and horizontal lines relate to discontinuities in the smooth mean deformations due to the specimen's edges, while the two sine waves in approximately diagonal directions for each displacement component correspond to a single long-range fluctuation mode. Based on these observations, the fluctuation mode is assigned as done for the virtual experiments, i.e. Eq. (5.6) with $\underline{\mathbb{o}}_{\varphi_1} = [1, 1, 1, 1, 1, 0, 0]^\mathsf{T}$ as initial guess. Note that this procedure is required only once for a metamaterial of a certain microstructural geometry, e.g. a cellular metamaterial with rectangular stacking of circular holes, and the same initialization of the mode can be used on any specimen with such microstructure. In order to assure a proper scaling of the minimization problem, $\boldsymbol{\varphi}_1(\mathbf{x})$ is scaled such that the initial maximum value of the mode is 0.04. In order to avoid an ill-posed problem in the first iteration, $v_1(\mathbf{x})$ is again initiated with a small constant value in space. The applied compressive global strain results in large displacement on the edges of the specimen, which requires an approximate initial guess in order to ensure convergence. Thus, the smooth mean field $\mathbf{v}_0(\mathbf{x})$ is initialized such that the first order term in x direction approximately accounts for the applied global strain.

The micromorphic IDIC results in a proper identification of $\mathbf{v}_0(\mathbf{x})$, $v_1(\mathbf{x})$ and $\boldsymbol{\varphi}_1(\mathbf{x})$, whereby the residual fields are small everywhere both before and after buckling, see Figs. 5.6g and o. Convergence is consistent. Fig. 5.6 shows the results of applying micromorphic IDIC on real experiments before (left) and after (right) the emergence

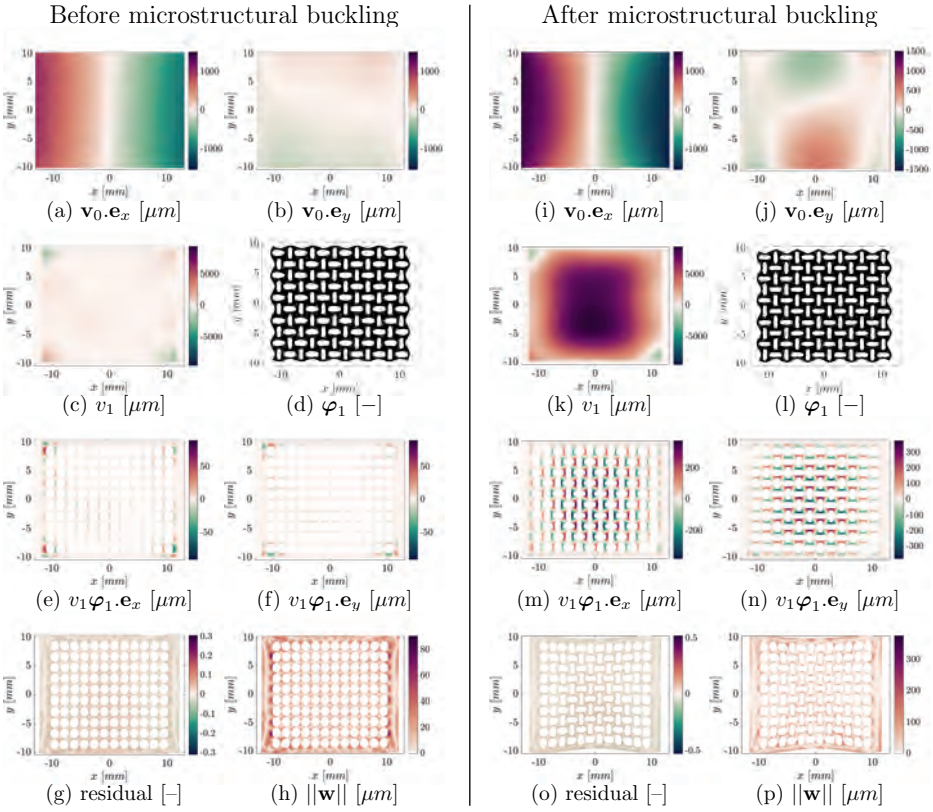

Figure 5.6: Results of the real experiments, before (left) and after (right) the onset of microstructural buckling:(a, b, i, j) the smooth mean displacement fields, $\mathbf{v}_0(\mathbf{x})$, in (a, i) x and (b, j) y directions; (c, k) the amplitudes, $v_1(\mathbf{x})$, (d, l) the deformed configuration of identified modes, $\boldsymbol{\varphi}_1(\mathbf{x})$, scaled to assure the visibility of the deformed shape, and (e, f, m, n) the resulting fields, (e, m) in x and (f, n) y directions, corresponding to the long-range correlated fluctuations. The long-range correlated fluctuation fields, $v_1(\mathbf{x})\boldsymbol{\varphi}_1(\mathbf{x})$, are plotted in their corresponding deformed configurations. (g, o) are the residual fields in normalized gray scales; and (h, p) the Euclidean norm of the microfluctuation field, $\mathbf{w}(\mathbf{x})$, plotted in deformed configuration based on the evaluated displacement, $\mathbf{u}(\mathbf{x})$.

of the buckling pattern. For each case, the mean smooth displacement field, $\mathbf{v}_0(\mathbf{x})$, in x and y directions and, $v_1(\mathbf{x})$ are depicted in the first two rows, i.e. Fig. 5.6a–c before and Fig. 5.6i–k after the onset of buckling. The $\mathbf{v}_0$ field shows compression in x direction both before and after buckling. Similar results as in the virtual experiments are observed in $\mathbf{v}_0$ and v_1. Note that the large values in $v_1(\mathbf{x})$ are due to the scaling of the corresponding mode $\boldsymbol{\varphi}_1$ (maximum value of 0.04). The auxetic effect is more pronounced in the real experiments (Figs. 5.6j,o) compared to the virtual experiments (Figs. 5.4j,o), due to the larger specimen size, i.e. the larger scale ratio. In a specimen with a larger scale ratio the buckling pattern in the center is less affected by the two

stiffening lateral edges, and thus it is more pronounced and results in larger auxetic effect.

The long-range correlated mode, $\boldsymbol{\varphi}_1(\mathbf{x})$, as well as the long-range correlated fluctuation fields, $v_1\boldsymbol{\varphi}_1(\mathbf{x})$, in x and y directions, are depicted in their deformed configurations in Fig. 5.6d–f and Fig. 5.6l–n, before and after buckling, respectively. In Figs. 5.6d and l, $\boldsymbol{\varphi}_1(\mathbf{x})$ is scaled to assure the visibility of the deformed shape of the modes. As expected, small values for v_1 prior to buckling entail a low sensitivity to the fluctuation mode, i.e. a slightly different mode is identified at this stage. Indeed, the long-range correlated fluctuation mode is as good as absent before the emergence of the buckling pattern, where it is not yet representative. The edge effect prior to buckling, which is most pronounced at the corner unit cells, is partially captured by the identified mode. This explains the non-zero values of v_1 and thus $v_1(\mathbf{x})\boldsymbol{\varphi}_1(\mathbf{x})$ in these areas.

The residual fields in normalized gray scales are shown in Fig. 5.6g and o, in the deformed configuration based on the evaluated displacement $\mathbf{u}(\mathbf{x})$ from Eq. (5.4), before and after buckling, respectively. In order to extract the microfluctuation field $\mathbf{w}(\mathbf{x})$, the displacement fields obtained by local DIC on the same images are used as the reference. Note that the local DIC procedure is not a part of the methodology introduced here, and is used only for performance evaluation purposes. Local DIC gives the displacement field with minimum kinematical constraints (yet with non-negligible statistical and systematic errors). Therefore, it is used here to assess the microfluctuation field (with errors from local DIC) in order to evaluate the performance of the method. Figs. 5.6h and p show the Euclidean norm of the microfluctuation field, $||\mathbf{w}||$, before and after buckling. The microfluctuation field $\mathbf{w}$, is of a higher spatial frequency than the characteristic frequency of $\boldsymbol{\varphi}_1$, which is more pronounced far from edges of the specimen in the post-buckling regime (Fig. 5.6p). Yet, it can be observed prior to buckling as well (Fig. 5.6h). Beyond buckling, the microfluctuation field $\mathbf{w}$ has a significantly smaller amplitude than the correlated fluctuation field. This is not the case prior to buckling, considering the almost zero contribution of the long-range correlated fluctuation field. The residual field is larger in certain areas which corresponds directly to higher values in the microfluctuation field, both before and after buckling.

All the identified fields, i.e. $\mathbf{v}_0(\mathbf{x})$, $v_1(\mathbf{x})$ and $\boldsymbol{\varphi}_1(\mathbf{x})$, satisfy the expected mechanical behaviour, and the correlation residual, reflected also in the evaluated microfluctuation field $\mathbf{w}(\mathbf{x})$, confirms the good performance of the micromorphic IDIC method.

5.4 Summary and Conclusions

Cellular elastomeric metamaterials generally exhibit a pattern transformation based on microstructural buckling at a critical level of compressive load. These pattern transformations are correlated over long ranges in the specimen and result in a considerable change in mechanical response after their emergence. A micromorphic Integrated Digital Image Correlation (micromorphic IDIC) method, was here developed to experimentally

identify and quantify the decomposed kinematics for cellular metamaterials. The decomposition follows a recently introduced homogenization scheme based on a micromorphic kinematical ansatz, which consists of three parts: (i) mean smooth displacements, corresponding to the slow-scale material level; (ii) long-range correlated fluctuation fields, representing the buckling patterns; and (iii) a microfluctuation field, which captures the remaining non-correlated part of the fluctuations. This kinematical ansatz was integrated within the digital image correlation scheme, enabling a direct identification of the smooth displacement and the long-range correlated fluctuation pattern and its spatial distribution field. A proper parametrization of the problem was performed, which includes a 2D Fourier series to capture the long-range fluctuation mode.

The methodology is validated on both virtual and real experiments for a specific case of elastomeric metamaterials with rectangular stacking of millimetre-sized circular holes. A standard spectral density analysis is used3 to attain a regularization with a reduced number of degrees of freedom and to initialize the associated parameters of the long-range fluctuation mode for the considered metamaterial. The method successfully decomposes the displacement field of cellular elastomers under compressive load, both before and after local microstructural buckling leading to long-range correlated pattern transformations. The performance of the method is assessed by identifying the microfluctuation fields through a comparison with local DIC data. In all cases, the microfluctuation field is of higher spatial frequency than the long-range fluctuations and of smaller amplitude after the emergence of the buckling pattern, thereby validating the kinematical ansatz as well as the micromorphic IDIC identification routine. An initial guess robustness study, performed by random perturbations upto 10% in fluctuation mode parameters, resulted in 98% robustness of the correlations and negligible errors (0.45% on average) in the results, confirming the robustness and the accuracy of the proposed method.

The micromorphic IDIC methodology is unique in the following aspects:

(i) The methodology aims at, and succeeds in identifying long-range correlated fluctuation fields, which is not existing yet in commercial DIC packages.

(ii) The decomposition of the displacement field is performed in a single minimization step, identifying the long-range correlated fluctuation mode, its amplitude in space, and the mean smooth displacement field;

(iii) The methodology can be readily extended to any cellular metamaterial by making proper initialization choices of the fluctuation modes;

(iv) It is easy to implement based on minimal modifications to conventional global DIC formulations.

Chapter 6

Conclusions and Recommendations

6.1 Conclusions

The goal of this thesis was to develop novel methodologies to extract and identify correlated fluctuations in the fields obtained from full-field displacement measurement techniques. Integrated Digital Image Correlation (IDIC), exploiting prior knowledge of the desired fields within the DIC scheme, was used for two different cases in which the identification of correlated fields is essential. First, the distortions in Scanning Electron Microscopy (SEM) images were considered, for which the correlated patterns introduce large errors if ignored in displacement measurements. Second, the correlated fluctuation patterns occurring in cellular metamaterials were studied. For both cases, novel IDIC methodologies were developed to identify and quantify the correlated parts of the measured kinematics.

SEM image artifacts

The findings in this thesis on the treatment of SEM imaging artifacts, in Chapters 2 and 3, may be summarized as follows:

- It is essential to study the imaging process in SEM in order to recognize the different types of imaging artifacts and the characteristics needed for their identification. Three different types were addressed: spatial distortion, drift distortion and line shift artifacts. In order to identify the artifacts concurrently with the mechanical deformations in the specimen, the non-linearity in the imaging process needs to be taken into account, which is done through a sequential composition of a series of mapping functions, each representing an imaging step during deformation of an *in-situ* experiment. These mapping functions, in order of interference during the imaging process, are related to scan line shifts, spatial distortion, and the drift distortion along with the mechanical deformations. Together, they represent a model of the SEM imaging system in an *in-situ* mechanical test, addressing Question (I) in the Introduction.
- Line shift artifacts are occurring randomly in time during the scanning of an SEM image. However, they exhibit a systematic form through localized shifts in

the image parallel to the scan direction. By parametrizing the distortion fields related to line shifts using smooth step functions, all the characteristics of the individual line shifts, i.e. the position of their occurrence, their amplitudes in x and y directions, and the width over which they spread, are identified. This directly addresses Question (II) in the Introduction. Obtaining a proper initial guess for the position of the line shifts and assigning them to their corresponding image turned out to be challenging. However, it this has been achieved by a simple precorrelation step.

- Spatial distortion is rooted in the electromagnetic objective lens. Thus it is safe to assume that it is a constant field in time, if the imaging parameters are not altered. This characteristic is exploited to measure the spatial distortion field prior to the *in-situ* test, in a calibration step with only discrete steps of rigid body motion, i.e. without any mechanical deformation. This directly addressed Question (II) in the Introduction.
- Drift distortion is rooted in the fact that during the scanning process in the SEM, there can be relative motion of the electron beam with respect to the specimen. This means that drift is a continuously evolving, smooth function in time, while the mechanical deformations are applied step wise. Considering the manner in which these two fields are affecting the images, it suffices to take two images at each load step to distinguish the drift distortion from the mechanical deformations. This complemented Question (II) in the Introduction.
- A model of the SEM imaging process was integrated with a DIC scheme, resulting in a generalized methodology for the identification and correction of SEM imaging artifacts. The artifact enriched integrated DIC was shown to be successful in the effective identification of all three types of SEM artifacts.
- A simplified version of the methodology developed here for correcting intrinsic SEM imaging artifacts can be used for simpler imaging systems such as optical microscopy. In optical imaging systems, images are captured instantaneously since no scanning process is involved, thus line shifts artifacts are irrelevant and drifting of the specimen with respect to the imaging system result in rigid body translations in the images and no distortions. However, the optical lenses exhibit distortions which are stationary in time, and are comparable to the spatial distortions in SEM images, yet with a simpler morphology. The artifact enriched IDIC methodology can be used for the correction of the images taken from optical microscopy *in-situ* tests, by considering only the spatial distortions and the mechanics mapping functions.

Cellular Metamaterials

As far as the characterization of correlated fluctuations in cellular metamaterials is concerned, the following observations resulted from Chapters 4 and 5.

- Small scale cellular elastomeric metamaterial specimens are manufactured using custom-made moulds. *In-situ* experiments are performed, which addresses Question (III) in the Introduction. Cellular elastomeric metamaterials, at a critical compressive load, exhibit a correlated fluctuation pattern triggered by the local buckling of the microstructure, leading to large local rotations in the material. The imposed boundary conditions on a cellular metamaterial specimen, typically, constrain these rotations, leading to a restriction of the correlated fluctuation pattern in boundary layers close to the edges. These boundary layers result in a considerable size effect, i.e. a change of the mechanical response depending on the ratio of the relative size of the specimen and the characteristic length of the microstructure. This size effect is particularly large for small scale ratios, where the size of the boundary layer almost spans the entire length of the specimen. The experiments revealed a 19% increase of the global stress in specimens with scale ratio 4 relative to specimens with scale ratio 12. An experimental study of the local rotation fields, obtained using local DIC, was conducted, allowing to determine the boundary layer size for specimens of different size. Comparison of the results with numerical simulations and the results form a recent idealized numerical study [44] on size effects in cellular metamaterials, revealed the influence of the lateral constraints on the specimen on the emergence and thickness of the boundary layers. This directly addresses Question (IV) in the Introduction.
- The micromorphic kinematical ansatz, introduced in an homogenization scheme for cellular metamaterials in the literature [45], was integrated with a DIC scheme. The resulting micromorphic integrated DIC decomposes the kinematics of cellular metamaterials into a smooth mean field and long-range correlated fluctuation fields, leaving out all the non-correlated microfluctuations. The correlated fluctuation fields were characterised by identifying the pattern modes along with the spatial distributions of their corresponding amplitudes. The micromorphic IDIC scheme was tested on an *in-situ* test on a cellular elastomeric metamaterial. It has been demonstrated that it successfully identifies the smooth field, the fluctuation modes and the spatial distribution of the modal amplitudes, addressing Question (V) in the Introduction.
- The methodology developed in Chapter 3, was exploited for the correction of spatial distortions of the optical microscope used in the experimental study on metamaterials in Chapters 4 and 5. A calibration step was performed prior to the *in-situ* tests to measure the spatial distortions. The spatial distortions were used to correct the images before local DIC was applied in Chapter 4. In Chapter 5, the spatial distortion correction has been integrated in the micromorphic IDIC methodology.

6.2 Recommendations for further research

Although the key objectives of this thesis have been reached, further developments of the proposed methodologies are possible to extend their applicability and deepen the understanding they offer. A few recommendations for such further developments are discussed:

- One of the most challenging aspects of the identification of SEM imaging distortions is the detection of the presence of line shifts in each image and obtaining a good initial guess for their positions in the corresponding image. The methodology introduced here, based on an analysis of the residual fields of precorrelations with minimal kinematic regularizations (first-order polynomials) works well, but is still limited to a few line shifts in each image. Further investigation of methods based on image processing techniques or even exploitation of local DIC data may result in a scheme addressing more line shifts, pushing the limits of the current method even further.
- The IDIC based methodology for artifact correction has been conceived for the specific case of SEM images, and further simplified for relatively less complicated case of optical distortions as well. However, the methodology itself is generic and is expandable to other imaging systems as well, such as Atomic Force Microscopy (AFM), with little effort. This can be achieved by careful consideration of the imaging process, translating it into a proper combination of mapping functions and a corresponding procedure to perform the measurements.
- Most of the experimental studies in the literature on cellular metamaterials are performed on large specimens which more resemble structures than materials. The cellular metamaterial specimens considered in this thesis are close to the dimensions relevant for engineering applications of these metamaterials. However, in many applications an even smaller microstructural length may be required. The lab-scale specimens (microstructure of millimetric characteristic length) used in this thesis were already challenging to manufacture with a quality allowing *in-situ* mechanical tests with full-field kinematical measurement. This is due to the presence of the very thin ligaments between the holes, in relation to the larger specimen thickness that ensures the occurrence of local buckling before global buckling. Further miniaturization of the specimens introduces more challenges that need to be addressed to enable in depth analysis of micro-scale cellular metamaterials (microstructure of micrometric characteristic length).
- Once the miniaturization of cellular elastomeric metamaterials is achieved, smaller specimens can be made with larger scale ratios, as long as the width and thickness of the specimens is large enough to prevent global buckling. Doing so, the investigation of size effects can be extended to shed more light on the emergence and development of boundary layers for more realistic boundary conditions. However, in order to acquire images from the entire surface of the specimens with high spatial resolution, necessary for an accurate kinematic assessment, the optical imaging needs to be substituted by a high-resolution imaging technique such

as SEM. This calls for the integration of all the chapters presented in this thesis to identify the long-range correlated fluctuation fields of cellular metamaterials as well as the SEM correlated distortion patterns to minimize the measurement errors. This can be achieved by adopting the regularization choices of micromorphic IDIC in the mechanical displacement regularizations used in the artifact enriched IDIC scheme.

- In more complex geometries, cellular metamaterials exhibit multiple long-range correlated fluctuation modes at the same time in different regions of a single specimen. In order to induce such combinations of modes, apart from the morphology of the microstructure, the loading conditions are important, e.g. cellular elastomeric metamaterials with hexagonal stacking of circular holes under biaxial compression [95]. Such loading conditions occur in realistic applications but are challenging to replicate in a controlled experimental environment. The micromorphic IDIC introduced in this thesis is capable of identifying more than one correlated mode in cellular metamaterials. An interesting continuation of the work done in this thesis, is to perform experimental tests that induce multiple long-range correlated fluctuation modes in a specimen, to be analysed with the proposed micromorphic IDIC scheme.
- The micromorphic IDIC methodology can be developed for any case where mechanical loading results in spatially correlated fluctuations, i.e. also localization of deformations. A proper study of the mechanical fluctuation fields can lead to a proper regularization of the displacement fields, that can be exploited to identify these correlated fluctuation fields. Such an extended IDIC scheme can then be integrated with an artifact enriched IDIC scheme for any imaging system such as, optical microscopy, SEM, AFM, etc.

Bibliography

[1] Michel Grediac, Frédéric Sur, and Benoît Blaysat. The grid method for in-plane displacement and strain measurement: A review and analysis. *Strain*, 52(3):205–243, 2016.

[2] M. A. Sutton, W. J. Wolters, W. H. Peters, W. F. Ranson, and S. R. McNeill. Determination of displacements using an improved digital correlation method. *Image and vision computing*, 1(3):133–139, 1983.

[3] M. A. Sutton and F. Hild. Recent Advances and Perspectives in Digital Image Correlation. *Experimental Mechanics*, 55:1–8, 2015.

[4] Bing Pan. Digital image correlation for surface deformation measurement: historical developments, recent advances and future goals. *Measurement Science and Technology*, 29(8):082001, 2018.

[5] F. Hild and S. Roux. Comparison of local and global approaches to digital image correlation. *Experimental Mechanics*, 52(9):1503–1519, 2012.

[6] Hubert W. Schreier, Dorian Garcia, and Michael A. Sutton. Advances in light microscope stereo vision. *Experimental mechanics*, 44(3):278–288, 2004.

[7] J. Neggers, J. P. M. Hoefnagels, F. Hild, S. Roux, and M. G. D. Geers. Direct stress-strain measurements from bulged membranes using topography image correlation. *Experimental Mechanics*, 54(5):717–727, 2014.

[8] A. Githens and S. Daly. Patterning corrosion-susceptible metallic alloys for digital image correlation in a scanning electron microscope. *Strain*, 53(1), 2017.

[9] R. V. Lapshin. Automatic drift elimination in probe microscope images based on techniques of counter-scanning and topography feature recognition. *Measurement Science and Technology*, 18(3):907–927, 2007.

[10] Z. H. Xu, X. D. Li, M. A. Sutton, and N. Li. Drift and spatial distortion elimination in atomic force microscopy images by the digital image correlation technique. *Journal of Strain Analysis for Engineering Design*, 43(8):729–743, 2008.

[11] H. Teyssedre, S. Roux, G. Régnier, and A. Tracz. Filtering out slow-scan drifts in atomic force microscopy images. *Journal of Strain Analysis for Engineering Design*, 46(5):361–367, 2011.

[12] X. Wang, Z. Pan, F. Fan, J. Wang, Y. Liu, S. X. Mao, T. Zhu, and S. Xia. Nanoscale deformation analysis with high-resolution transmission electron microscopy and digital image correlation. *Journal of Applied Mechanics, Transactions ASME*, 82(12), 2015.

[13] M. A. Sutton, N. Li, D. Garcia, N. Cornille, J. J. Orteu, S. R. McNeill, H. W. Schreier, and X. Li. Metrology in a scanning electron microscope: theoretical developments and experimental validation. *Measurement Science and Technology*, 17(10):2613–2622, 2006.

[14] H. Wang, H. Xie, Y. Ju, and Q. Duan. Error analysis of digital speckle correlation method under scanning electron microscope. *Experimental Techniques*, 30(2):42–45, 2006.

[15] N. Li, M. A. Sutton, X. Li, and H. W. Schreier. Full-field thermal deformation measurements in a scanning electron microscope by 2D digital image correlation. *Experimental Mechanics*, 48(5):635–646, 2008.

[16] P. Cizmar, A. E. Vladár, and M. T. Postek. Real-time scanning charged-particle microscope image composition with correction of drift. *Microscopy and Microanalysis*, 17(2):302–308, 2011.

[17] T. Arikawa, G. Murasawa, and S. Yoneyama. Accurate displacement field measurement with scanning electron microscopy imaging. *Journal of Strain Analysis for Engineering Design*, 46(5):337–346, 2011.

[18] A. D. Kammers and S. Daly. Digital Image Correlation under Scanning Electron Microscopy: Methodology and Validation. *Experimental Mechanics*, 53(9):1743–1761, 2013.

[19] G. S. Schajer, B. Winiarski, and P. J. Withers. Hole-Drilling Residual Stress Measurement with Artifact Correction Using Full-Field DIC. *Experimental Mechanics*, 53(2):255–265, 2013.

[20] R. Jiang, F. Pierron, S. Octaviani, and P. A. S. Reed. Characterisation of strain localisation processes during fatigue crack initiation and early crack propagation by SEM-DIC in an advanced disc alloy. *Materials Science and Engineering A*, 699:128–144, 2017.

[21] J. C. Pina, S. Shafqat, V. G. Kouznetsova, J. P. M. Hoefnagels, and M. G. D. Geers. Microstructural study of the mechanical response of compacted graphite iron: An experimental and numerical approach. *Materials Science and Engineering A*, 658:439–449, 2016.

[22] Catalina Mansilla, Václav Ocelík, and Jeff T. M. De Hosson. A New Methodology to Analyze Instabilities in SEM Imaging. *Microscopy and microanalysis*, pages 1–13, 2014.

[23] P. Jin and X. Li. Correction of image drift and distortion in a scanning electron microscopy. *Journal of Microscopy*, 260(3):268–280, 2015.

[24] Q. SHI, S. Roux, F. Latourte, F. Hild, D. Loisnard, and N. Brynaert. On the use of SEM correlative tools for in situ mechanical tests. *Ultramicroscopy*, 184:71–87, 2018.

[25] M. A. Sutton, N. Li, D. Garcia, N. Cornille, J. J. Orteu, S. R. McNeill, H. W. Schreier, X. Li, and A. P. Reynolds. Scanning Electron Microscopy for Quantitative Small and Large Deformation Measurements Part II: Experimental Validation for Magnifications from 200 to 10,000. *Experimental Mechanics*, 47(6):789–804, 2007.

[26] A. Guery, F. Latourte, F. Hild, and S. Roux. Characterization of SEM speckle pattern marking and imaging distortion by digital image correlation. *Measurement Science and Technology*, 25(1):015401, 2014.

[27] A. W. Mello, T. A. Book, A. Nicolas, S. E. Otto, C. J. Gilpin, and M. D. Sangid. Distortion correction protocol for digital image correlation after scanning electron microscopy: Emphasis on long duration and ex-situ experiments. *Experimental Mechanics*, 57(9):1395–1409, 2017.

[28] M. A. Sutton, N. Li, D. C. Joy, A. P. Reynolds, and X. Li. Scanning Electron Microscopy for Quantitative Small and Large Deformation Measurements Part I: SEM Imaging at Magnifications from 200 to 10,000. *Experimental Mechanics*, 47(6):775–787, 2007.

[29] K. Bertoldi, M. C. Boyce, S. Deschanel, S. M. Prange, and T. Mullin. Mechanics of deformation-triggered pattern transformations and superelastic behavior in periodic elastomeric structures. *Journal of the Mechanics and Physics of Solids*, 56(8):2642–2668, 2008.

[30] Katia Bertoldi, Pedro M. Reis, Stephen Willshaw, and Tom Mullin. Negative Poisson's ratio behavior induced by an elastic instability. *Advanced Materials*, 22(3):361–366, 2010.

[31] J. T. B. Overvelde, S. Shan, and K. Bertoldi. Compaction through buckling in 2D periodic, soft and porous structures: Effect of pore shape. *Advanced Materials*, 24(17):2337–2342, 2012.

[32] Jianying Hu, Yuhao He, Jincheng Lei, and Zishun Liu. Novel mechanical behavior of periodic structure with the pattern transformation. *Theoretical and Applied Mechanics Letters*, 3(5):054007, 2013.

[33] Johannes T. B. Overvelde and Katia Bertoldi. Relating pore shape to the non-linear response of periodic elastomeric structures. *Journal of the Mechanics and Physics of Solids*, 64(1):351–366, 2014.

[34] Yichao Tang, Gaojian Lin, Lin Han, Songgang Qiu, Shu Yang, and Jie Yin. Design of hierarchically cut hinges for highly stretchable and reconfigurable metamaterials with enhanced strength. *Advanced Materials*, 27(44):7181–7190, 2015.

[35] Alex Slann, William White, Fabrizio Scarpa, Katarzyna Boba, and Ian Farrow. Cellular plates with auxetic rectangular perforations. *Physica Status Solidi (b)*, 252(7):1533–1539, 2015.

[36] Farhad Javid, Jia Liu, Jongmin Shim, James C. Weaver, Ali Shanian, and Katia Bertoldi. Mechanics of instability-induced pattern transformations in elastomeric porous cylinders. *Journal of the Mechanics and Physics of Solids*, 96:1–17, 2016.

[37] Hang Xu and Damiano Pasini. Structurally efficient three-dimensional metamaterials with controllable thermal expansion. *Scientific reports*, 6:34924, 2016.

[38] Nathanael Easey, Dimitro Chuprynyuk, Wan Wan Musa, Angus Banks, Yousef Dobah, Anton Shterenlikht, and Fabrizio Scarpa. Dome-shape auxetic cellular metamaterials: manufacturing, modelling and testing. *Frontiers in Materials*, 6:86, 2019.

[39] R. Hedayati, S. Jedari Salami, Y. Li, M. Sadighi, and A. A. Zadpoor. Semianalytical geometry-property relationships for some generalized classes of pentamodelike additively manufactured mechanical metamaterials. *Physical Review Applied*, 11(3), 2019.

[40] Dian Yang, Bobak Mosadegh, Alar Ainla, Benjamin Lee, Fatemeh Khashai, Zhigang Suo, Katia Bertoldi, and George M. Whitesides. Buckling of Elastomeric Beams Enables Actuation of Soft Machines. *Advanced Materials*, 27(41):6323–6327, 2015.

[41] M. J. Mirzaali, S. Janbaz, M. Strano, L. Vergani, and A. A. Zadpoor. Shape-matching soft mechanical metamaterials. *Scientific Reports*, 8(1):1–7, 2018.

[42] D. Krishnan and H. T. Johnson. Optical properties of two-dimensional polymer photonic crystals after deformation-induced pattern transformations. *Journal of the Mechanics and Physics of Solids*, 57(9):1500–1513, 2009.

[43] Bastiaan Florijn, Corentin Coulais, and Martin Van Hecke. Programmable mechanical metamaterials. *Physical Review Letters*, 113(17):1–5, 2014.

[44] M. M. Ameen, O. Rokoš, R. H. J. Peerlings, and M. G. D. Geers. Size effects in nonlinear periodic materials exhibiting reversible pattern transformations. *Mechanics of Materials*, 124(June):55–70, 2018.

[45] O. Rokoš, M. M. Ameen, R. H. J. Peerlings, and M. G. D. Geers. Micromorphic computational homogenization for mechanical metamaterials with patterning fluctuation fields. *Journal of the Mechanics and Physics of Solids*, 123:119 – 137, 2019. The N.A. Fleck 60th Anniversary Volume.

[46] D. Y. Kang, H. M. Tong, J. Zang, R. P. Choudhury, D. S. Sholl, H. W. Beckham, C. W. Jones, and S. Nair. *ACS applied materials & interfaces*.

[47] N. Brodusch, M. Yourdkhani, P. Hubert, and R. Gauvin. Efficient cross-section preparation method for high-resolution imaging of hard polymer composites with a scanning electron microscope. *Journal of Microscopy*, 260(2):117–124, 2015.

[48] J. D. Lord, B. Roebuck, R. Morrell, and T. Lube. 25 year perspective aspects of strain and strength measurement in miniaturised testing for engineering metals and ceramics. *Materials Science and Technology*, 26(2):127–148, 2010.

[49] Caroline F. Bellani, Eric Pollet, Anne Hebraud, Fabiano V. Pereira, Guy Schlatter, Luc Avérous, Rosario E. S. Bretas, and Marcia C. Branciforti. *Journal of Applied Polymer Science*.

[50] J. L. Gu, M. S. Khil, K. K. Beom, M. Gopiraman, K. H. Song, and I. S. Kim. Effect of POSS content on the electrical, thermal, mechanical, and wetting properties of electrospun polyacrylonitrile (PAN)/POSS nanofibrous mats. *Journal of Experimental Nanoscience*, 11(7):500–511, 2016.

[51] K. O. Mussa, M. S. Mousa, and A. Fischer. Information extraction from FN plots of tungsten microemitters. *Ultramicroscopy*, 132:48–63, 2013.

[52] H. G. Jones, K. P. Mingard, and D. C. Cox. *Ultramicroscopy*.

[53] M. A. Sutton, H. Schreier, and J. J. Orteu. *Image Correlation for Shape, Motion and Deformation Measurements*. Springer US, Boston, MA, 2009.

[54] Nick McCormick and Jerry Lord. Digital image correlation. *Materials today*, 13(12):52–54, 2010.

[55] M. T. Postek and A. E. Vladár. *Scanning*.

[56] M. T. Postek, A. E. Vladár, and K. P. Purushotham. Does your SEM really tell the truth? How would you know? Part 2. *Scanning*, 36(3):347–55, 2013.

[57] M. T. Postek, A. E. Vladár, and P. Cizmar. Nanomanufacturing concerns about measurements made in the SEM Part III: vibration and drift. In *Proceedings of SPIE - The International Society for Optical Engineering*, volume 9173, 2014.

[58] T. R. Meyer, D. Ziegler, C. Brune, A. Chen, R. Farnham, N. Huynh, J. M. Chang, A. L. Bertozzi, and P. D. Ashby. Height drift correction in non-raster atomic force microscopy. *Ultramicroscopy*, 137:48–54, 2014.

[59] C. Ophus, J. Ciston, and C. T. Nelson. *Ultramicroscopy*.

[60] F. Lagattu, F. Bridier, P. Villechaise, and J. Brillaud. In-plane strain measurements on a microscopic scale by coupling digital image correlation and an in situ SEM technique. *Materials Characterization*, 56:10–18, 2006.

[61] J. Neggers, B. Blaysat, J. P. M. Hoefnagels, and M. G. D. Geers. On image gradients in digital image correlation. *International Journal for Numerical Methods in Engineering*, 105(4):243–260, 2016.

[62] P. Lava, W. Van Paepegem, S. Coppieters, I. De Baere, Y. Wang, and D. Debruyne. Impact of lens distortions on strain measurements obtained with 2d digital image correlation. *Optics and Lasers in Engineering*, 51(5):576–584, 2013.

[63] J. C. Stinville, M. P. Echlin, D. Texier, F. Bridier, P. Bocher, and T. M. Pollock. Sub-grain scale digital image correlation by electron microscopy for polycrystalline materials during elastic and plastic deformation. *Experimental Mechanics*, 56(2):197–216, 2016.

[64] J. E. Dufour, F. Hild, and S. Roux. Integrated digital image correlation for the evaluation and correction of optical distortions. *Optics and Lasers in Engineering*, 56:121–133, 2014.

[65] S. Maraghechi, J. P. M. Hoefnagels, R. H. J. Peerlings, and M. G. D. Geers. Correction of scan line shift artifacts in scanning electron microscopy: An extended digital image correlation framework. *Ultramicroscopy*, 187:144–163, 2018.

[66] J. Neggers, J. P. M. Hoefnagels, M. G. D. Geers, F. Hild, and S. Roux. Time-resolved integrated digital image correlation. *International Journal for Numerical Methods in Engineering*, 103(3):157–182, 2015.

[67] M. Haider, S. Uhlemann, and J. Zach. Upper limits for the residual aberrations of a high-resolution aberration-corrected stem. *Ultramicroscopy*, 81(3-4):163–175, 2000.

[68] C. Kisielowski, B. Freitag, M. Bischoff, H. Van Lin, S. Lazar, G. Knippels, P. Tiemeijer, M. Van Der Stam, S. Von Harrach, M. Stekelenburg, M. Haider, S. Uhlemann, H. Müller, P. Hartel, B. Kabius, D. Miller, I. Petrov, E. A. Olson, T. Donchev, E. A. Kenik, A. R. Lupini, J. Bentley, S. J. Pennycook, I. M. Anderson, A. M. Minor, A. K. Schmid, T. Duden, V. Radmilovic, Q. M. Ramasse, M. Watanabe, R. Erni, E. A. Stach, P. Denes, and U. Dahmen. Detection of single atoms and buried defects in three dimensions by aberration-corrected electron microscope with 0.5-Å information limit. *Microscopy and Microanalysis*, 14(5):469–477, 2008.

[69] L. Grella, G. Lorusso, and D. L. Adler. Simulations of scanning electron microscopy imaging and charging of insulating structures. *Scanning*, 25(6):300–308, 2003.

[70] P. L. Reu, E. Toussaint, E. Jones, H. A. Bruck, M. Iadicola, R. Balcaen, D. Z. Turner, T. Siebert, P. Lava, and M. Simonsen. Dic challenge: Developing images and guidelines for evaluating accuracy and resolution of 2d analyses. *Experimental Mechanics*, pages 1–33, 2017.

[71] Jorge Nocedal and Stephen J. Wright. *Numerical Optimization, second edition.* World Scientific, 2006.

[72] L. Wittevrongel, P. Lava, S. V. Lomov, and D. Debruyne. C^n-continuity in digital image correlation: Implementation and validation of C^{-1}, C^0 and C^1 algorithms. *Strain*, 51(6):444–458, 2015.

[73] U. Hoeberichts. Optimization of DIC patterns at different length scales and imaging techniques. *Open Space Project, Eindhoven University of Technology*, pages 1 – 40, 2014.

[74] Xianglong Yu, Ji Zhou, Haiyi Liang, Zhengyi Jiang, and Lingling Wu. Mechanical metamaterials associated with stiffness, rigidity and compressibility: A brief review. *Progress in Materials Science*, 94:114–173, 2018.

[75] L. Francesconi, A. Baldi, X. Liang, F. Aymerich, and M. Taylor. Variable Poisson's ratio materials for globally stable static and dynamic compression resistance. *Extreme Mechanics Letters*, 26:1–7, 2019.

[76] M. J. Mirzaali, A. Caracciolo, H. Pahlavani, S. Janbaz, L. Vergani, and A. A. Zadpoor. Multi-material 3D printed mechanical metamaterials: Rational design of elastic properties through spatial distribution of hard and soft phases. *Applied Physics Letters*, 113(24), 2018.

[77] Gaoxiang Wu, Yu Xia, and Shu Yang. Buckling, symmetry breaking, and cavitation in periodically micro-structured hydrogel membranes. *Soft Matter*, 10(9):1392–1399, 2014.

[78] Jianying Hu, Yu Zhou, and Zishun Liu. The Friction Effect on Buckling Behavior of Cellular Structures Under Axial Load. *International Journal of Applied Mechanics*, 10(02):1850013, 2018.

[79] S. Maraghechi, J. P. M. Hoefnagels, R. H. J. Peerlings, O. Rokoš, and M. G. D. Geers. Correction of scanning electron microscope imaging artifacts in a novel digital image correlation framework. *Experimental Mechanics*, 2019.

[80] Miao Liu, Jianren Sun, and Quanfang Chen. Influences of heating temperature on mechanical properties of polydimethylsiloxane. *Sensors and Actuators, A: Physical*, 151(1):42–45, 2009.

[81] Tae Kyung Kim, Jeong Koo Kim, and Ok Chan Jeong. Measurement of nonlinear mechanical properties of PDMS elastomer. *Microelectronic Engineering*, 88(8):1982–1985, 2011.

[82] Aaron P. Gerratt, Ivan Penskiy, and Sarah Bergbreiter. In situ characterization of PDMS in SOI-MEMS. *Journal of Micromechanics and Microengineering*, 23(4), 2013.

[83] I. D. Johnston, D. K. McCluskey, C. K. L. Tan, and M. C. Tracey. Mechanical characterization of bulk Sylgard 184 for microfluidics and microengineering. *Journal of Micromechanics and Microengineering*, 24(3), 2014.

[84] P. Wriggers. *Nonlinear Finite Element Methods*. Springer-Verlag Berlin Heidelberg, 2008.

[85] B. G. Vossen, O. Van der Sluis, P. J. G. Schreurs, M. G. D. Geers, J. Neggers, and J. P. M. Hoefnagels. On the role of fibril mechanics in the work of separation of fibrillating interfaces. *Mechanics of Materials*, 88:1–11, 2015.

[86] Tom Mullin, S. Deschanel, Katia Bertoldi, and Mary C. Boyce. Pattern transformation triggered by deformation. *Physical review letters*, 99(8):084301, 2007.

[87] De-Gang Zhao, Yong Li, and Xue-Feng Zhu. Broadband lamb wave trapping in cellular metamaterial plates with multiple local resonances. *Scientific reports*, 5:9376, 2015.

[88] Osama R. Bilal, André Foehr, and Chiara Daraio. Reprogrammable phononic metasurfaces. *Advanced materials*, 29(39):1700628, 2017.

[89] Maximilian Wormser, Fabian Wein, Michael Stingl, and Carolin Körner. Design and additive manufacturing of 3D phononic band gap structures based on gradient based optimization. *Materials*, 10(10):1125, 2017.

[90] Katia Bertoldi, Vincenzo Vitelli, Johan Christensen, and Martin van Hecke. Flexible mechanical metamaterials. *Nature Reviews Materials*, 2(11):17066, 2017.

[91] H MA Kolken and AA Zadpoor. Auxetic mechanical metamaterials. *RSC Advances*, 7(9):5111–5129, 2017.

[92] S. Amin Yavari, S. M. Ahmadi, R. Wauthle, B. Pouran, J. Schrooten, H. Weinans, and A. A. Zadpoor. Relationship between unit cell type and porosity and the fatigue behavior of selective laser melted meta-biomaterials. *Journal of the mechanical behavior of biomedical materials*, 43:91–100, 2015.

[93] Amir Zadpoor. Design for additive bio-manufacturing: From patient-specific medical devices to rationally designed meta-biomaterials. *International journal of molecular sciences*, 18(8):1607, 2017.

[94] Andre P. Ruybalid, Johan P. M. Hoefnagels, Olaf. van der Sluis, and Marc G. D. Geers. Comparison of the identification performance of conventional FEM updating and integrated DIC. *International Journal for Numerical Methods in Engineering*, 106(4):298–320, 2016.

[95] O. Rokoš, M. M. Ameen, R. H. J. Peerlings, and M. G. D. Geers. Extended micromorphic computational homogenization for mechanical metamaterials exhibiting multiple geometric pattern transformations. *In preparation*, 2019.

[96] M. Grigoriu. *Stochastic Calculus: Applications in Science and Engineering.* Birkhäuser, 2002.

Words of Thanks

I would rather be honest than appealing, going through this PhD was though! This might not be the place to elaborate on how and why, but the fact that it was a though process, is the exact fact which leaves something behind for me to grow. Obviously there was a lot of joy in it too, without this pleasure I would have simply not finished it.

In 2014, I joined the Mechanics of Materials research group, where the mentality and attitude of the group has become the basis of my whole PhD experience. The very serious professional environment in MoM gave me the motivation needed to perform at the best I can. Yet I have always felt myself in a friendly environment in which I am cared for in moments of difficulty, and this combination is something I appreciate. Marc, thank you for curating, managing, and keeping this group alive and as it is. And thank you for your precise observation and supervision of my process over these years, making sure that we don't deviate (at least not too much) from the path which takes us where we intended to reach. Throughout this rough, adventurous, sometimes dark and sometimes light, path, I never felt alone. This is all thanks to the best duo I could have wished for as supervisors, Johan and Ron. Hours and hours of discussion on every aspect of every step we took has been so essential, that it's hard to distinguish them from the PhD itself. The combination of the fast thinking, super enthusiastic Johan, with the calm, patient, precise Ron has been something to enjoy and learn from. Johan, you know that you have been not just a supervisor but a friend and a brother to me, and this is amazing. I loved all the heated discussions we stubbornly pursued about work and more. Ron, your presence in my project has been the ground on which I felt safe and encouraged to keep on going. You have always had a fatherly attitude and a kind understanding of me as a human being, that helped me find control over myself and my project. Thank you both with all my hearth. Somewhere in the middle of my PhD, I was lucky to be able to collaborate with Ondrej, a collaboration which has been filled with learning and pleasure for me. Thanks a lot Ondrej, for all the help and the kindness.

I got to know many lovely people in these years in the university. Salman and Mirka, you have been THE buddies for me throughout these PhD years. All the 4.13ers, Rody, Maqsood, Jim, Steyn, Stefan, Vahid, Sandra, Luv, Majid, Mohsen, Nilgoon, Emanuela, Mary, no one can argue against the fact that we have had the best office ever. Prakhyat, Rosaria, Fabio, Jessica, Coen, Javier, thanks for being very lovely and polymeric. All the MoM people, Andre (I loved every single moment of engaging with your consciousness in

our interesting chats), Francesco (the wise advising brother), Chaowei, Ashwin, Varun and Varun, Aslan, Niles, Marc van Maris (the soul of all the experimental work in our group), Alice and Rachel (the most fun and cool part of MoM) and probably more nice people I'm missing out in this list.

There is a parallel universe that lives in Eindhoven, and I was lucky to be able to live it where I met many amazing people. Anastasija, you have been the door to this world for me, and became a unique companion in it, thanks for the crazily-real friendship we share. Sami, Penny and Elsa (the distilled amazingness that filled my first years in Eindhoven), Stefano (with the tips of all your fingers touching one another just in front of your chest), Ariana (the floating cuteness), Francesco (The Zorzi, with all the life inside you), Matlide, Lodovica, Lucas (the peacefulness itself) and Flo, Sarah, Mila, and again many more amazing souls, specially Shahin, Samereh and Janan (the crazy lightness emitting creatures you guys are).

A part of me has lived away from Eindhoven in all these years, for good reasons. Maryam, you have always been not just a sister, but a friend, the very first one in fact. Thanks for the longest friendship of my life, and thanks for bringing Hessam and tiny Mani to our lives. Farhad (my metabrother who knows me better than anyone in the world), Ehsan, Mohammad you have been the friends with whom I truly experienced friendship and keep on doing so. Kevin, that keeps on bringing softness to my life (with all the times you felt forced to vacuum clean my room, probably as many times as I did it myself :D).

Tonia, it's the hardest thing to write about you. You have been so deeply close to me, that talking about your place in my life feels like talking about my life in these years itself. Thank you for the beauty you are.

Everything I have achieved, even if purely with my own efforts, including this PhD, I have managed to achieve because of the person I am and the attitude I take towards life. And I deeply believe this is all rooted in my mother and father. I, as a child and a teenager, continuously observed my parents living their lives in the most beautiful way. Sure I've learnt, and slowly slowly made the basis of who I am. Maman, all I know about beauty, in any context of it, I have learned from you. You showed me how to know and appreciate beauty, and you did it all so effortlessly, just because you know and appreciated it so truly. Baba, I learnt how to think, to analyse and how to understand from you. I had the best mind to look at, and learn from all my life, and that is what formed me into what I am intellectually. Thank you both, for what you are, how you live and how you brought us up. I could not have been luckier than having you in my life.

Siavash
Eindhoven
Autumn 2019

List of Publications

Below is a list of publications related to the thesis:

- S. Maraghechi, J. P. M. Hoefnagels, R. H. J. Peerlings, M. G. D. Geers, Correction of scan line shift artifacts in scanning electron microscopy - an extended digital image correlation framework, *Ultramicroscopy*, 187:144-163, 2018.
- S. Maraghechi, J. P. M. Hoefnagels, R. H. J. Peerlings, O. Rokoš, M. G. D. Geers, Correction of scanning electron microscope imaging artifacts in a novel digital image correlation framework, *Experimental Mechanics*, 59:489-516, 2019.
- S. Maraghechi, J. P. M. Hoefnagels, R. H. J. Peerlings, O. Rokoš, M. G. D. Geers, Experimental full-scale analysis of size effects in cellular elastomeric metamaterials, 2019, *Submitted*.
- S. Maraghechi, O. Rokoš, J. P. M. Hoefnagels, R. H. J. Peerlings, M. G. D. Geers, arvesting micromorphic fields from experiments on patterning metamaterials, 2019, *Submitted*.

Curriculum Vitae

Siavash Maraghechi was born on 8 of February 1988 in Tehran, Iran. He obtained his Bachelor diploma in Mechanical Engineering from Iran University of Science and Technology, Tehran, in 2011. Directly after, he pursed a Master's degree in Mechanical Engineering at Politecnico di Milano, Italy. He successfully graduated in 2014 with the thesis "Mechanical Behavior of Stretchable Electronics with Specific Reference to Delamination and Buckling of the Metal Interconnects on Polymeric Substrate", supervised by Dr. Pasquale Vena. After his masters, Siavash was offered a PhD position at the Eindhoven University of Technology. The project titled, "Experimental full-field assessment of kinematical and imaging fluctuation patterns" was funded by the European Research Council and carried out in the Mechanics of Materials research group under the supervision of Prof. M.G.D. Geers, Dr. J.P.M. Hoefnagels and Dr. R.H.J. Peerlings. The results of the project are presented in this thesis.